TERNARY BREAKING OF THE REACTION SYSTEM IN HEAVY-ION COLLISIONS BELOW THE FERMI ENERGY

A Dissertation

by

PAUL JOSEPH CAMMARATA

Submitted to the Office of Graduate and Professional Studies of
Texas A&M University
in partial fulfillment of the requirements for the degree of

DOCTOR OF PHILOSOPHY

Chair of Committee,	Sherry J. Yennello
Committee Members,	Aldo Bonasera
	Charles M. Folden III
	Robert R. Lucchese
Head of Department,	François P. Gabbaï

May 2015

Major Subject: Chemistry

ABSTRACT

Heavy-ion collisions have played an important role in probing the asymmetry term of the nuclear Equation of State (nEoS). As the bombarding energy increases from lower energies (∼9 MeV/nucleon) to near the Fermi energy, the reaction mechanism transitions from deep-inelastic transfer reactions to those resulting in the multi fragmentation of the reaction system. In the energy regime between the two extremes, there is the possibility of observing the dynamical breaking of the system into a few heavy reaction partners. This feature, regardless of the energy or asymmetry of the reacting system, has been predicted to be sensitive to the asymmetry term of the nEoS through a number of theoretical predictions.

Recently, a new experiment has been conducted at the Texas A&M University Cyclotron Institute to explore the dynamical breaking of the reaction system at 15 MeV/nucleon. The reaction systems studied, ^{136}Xe,^{124}Sn+^{64}Ni and ^{124}Xe+^{58}Ni, were chosen as they provide a wide range of isospin asymmetry. The forward array using silicon technology (FAUST) was coupled to a large quadrupole triplet spectrometer (QTS) to collect both the emitted intermediate mass fragments ($Z \geq 3$) and the heavy, projectile-like remnant. This arrangement was designed, based on the predictions of numerous simulations, to be the most sensitive for detecting a three-body breakup of the reaction system.

Previously, experimental observations have shown a strong angular alignment in the dynamical breakup of the hot, projectile-like source. In this experiment, a dependence on the charge and isospin asymmetry of the entrance channel in this energy regime is noted. A modest dependence on the mass and energy of the quasi-projectile (QP) source has been shown to play a significant role in understanding the angular

distributions of the breakup. This dependence has been shown to act as a surrogate for the impact parameter of the collision. Additionally, the velocity of the resultant projectile-like fragment plays a key role in sorting out the dynamical vs. statistical breaking of the reaction system, especially when compared to experimentally filtered theoretical simulations (CoMD+Gemini). These dynamical events have revealed a neutron enrichment of the IMFs emitted from near the neck region, on short time scales, in good agreement with previously published data.

The underlying shape of the hot QP has been predicted to be both sensitive to the asymmetry term of the nEoS and the driving force behind the few body breaking of the reaction system. Experimentally, being only able to detect the two resultant fragments of the QP breakup required the use of a surrogate method to qualitatively approximate the shape of the QP at the time of break-up. The dynamical events analyzed were, on average, the result of QPs with little deformation in velocity space. There was good agreement between the simulations and the experimental data.

Recently, a machine learning algorithm has been tested in an attempt to consider multiple observables predicted to be sensitive to the symmetry energy concurrently. Initial testing of the algorithm proved promising, utilizing unfiltered results from dynamical simulations. This technique has been extended to experimentally filtered simulation data with statistically significant results. Within experimental detector constraints, the simulations retain enough sensitivity for the machine learning algorithm to discriminate between the parameterizations of the symmetry energy.

DEDICATION

To Corinne and Frankie

ACKNOWLEDGEMENTS

First and foremost, I would like to thank my wife, Corinne, and son, Frankie, for their patience and undying support all these years while working on my Ph.D. Thank you to Prof. Sherry J. Yennello for taking a chance on me and providing me the opportunity to explore nuclear chemistry and physics to my curiosity's satisfaction. Thank you for your advice on all things science and the rather long leash you kept me on. I would like to thank Dr. Maria Colonna and Dr. Aldo Bonasera not only for the use and assistance in running and interpreting their dynamical simulations, but also for their great insight, conversations and direction in searching for the most interesting physics. Matt Chapman was instrumental in the construction of the beam line, testing of detectors, and design and fabrication of the automated beam line control system. I would like to thank Dr. George Souliotis for his help in setting up, running and interpreting charged ion optics simulations. Thank you to Larry May and Andrew Zarrella for being a sounding board, physics and mathematical treasure and for just in general putting up with my general vagaries. Thank you to Spencer Behling for going out of his way to be available for complex coding questions and help during data collection shift work. I'd like to thank Dr. Kris Hagel for helping with ROOT, Cyclotron Applications and numerous problems along the way in properly setting up the analysis code. Thanks to Dr. Justin Mabiala, Lauren Heilborn, Giacomo Bonasera, Layla Bahktiari, Dr. Mike Youngs, and Dr. Alan McIntosh for their help in the preparation and analysis of the experiment. Thank you to my committee, Prof. Sherry J. Yennello, Prof. Aldo Bonasera, Prof. Charles M. Folden III, and Prof. Robert R. Lucchese.

A special thanks to Will Seward for his expert machining, fabrication and design

advice. His skill, and the skill of his machinists, made it possible to construct a new experimental beam line in less than six months. To this end, thanks to Eric Yendry, Shane Smith, Bill Morgan, and the rest of the cyclotron technical staff for their expert advice and ability. Also, thanks are due to Dr. George Kim, Dr. Brian Roeder and Dr. Henry Clark for the excellent beam quality, tireless dedication to multiple beam changes, and the generous allocation of 30 days of experimental beam-time on top of several test runs.

TABLE OF CONTENTS

Page

LIST OF FIGURES

FIGURE Page

LIST OF TABLES

TABLE Page

1. INTRODUCTION

Intermediate energy, heavy-ion collisions (HICs) around the Fermi energy (10 -100A MeV) provide a rich environment to study reaction dynamics, as there are a number of competing reaction mechanisms. This competition between dynamical emission, pre-equilibrium emission and statistical decay of reaction products results in the mixture of observables resulting from projectile/target fragmentation, multi-fragmentation of the reacting system, intermediate mass fragment (IMF) clusters and light charged particle (LCP) neck emission, quasi-fission, and fusion evaporation in this energy regime. The asymmetry dependence of these processes are important when experimentally investigating the isospin degree of freedom to probe the nuclear equation-of-state (nEoS) of asymmetric nuclear matter. The nEoS plays a fundamental role in describing nuclear and astrophysical phenomena. Heavy-ion collisions provide the unique opportunity to probe nuclear matter at temperatures, densities and isospin content, in the lab, far away from ground state nuclei.

1.1 Nuclear Equation of State

The nuclear equation-of-state provides a description of the nuclear binding energy as a function of pressure, density, temperature, isospin content, etc. There is some variation in the description of the nEoS across a range of models[1, 2, 3, 4]. This is especially true away from ground state nuclei. Ground state nuclei are defined as those nuclei with T=0 MeV and at density of $\rho_0 = 0.16$ nucleons/fm^3 (saturation density). The binding energies of the ground state nuclei are fairly well understood. Ground state nuclei are fairly well described by the semi-empirical liquid drop model of Weisäcker et al.[5, 6]. This model describes the binding energy of the ground state nucleus in terms of the liquid drop parameters (surface and bulk/volume effects)

and as a function of mass (A), charge (Z) and neutron (N) content of the nuclei as shown in Eq. 1.1. The volume term (a_v) provides the bulk binding energy associated with nuclear material. The remainder of the terms diminish this binding energy. The surface term (a_s) accounts for the finite, spherical volume due to the surface energy. This decrease in binding energy results from a decreased number of nearest-neighbors at the surface of the nucleus. The Coulomb (a_{Coul}) and symmetry (a_{sym}) terms account for the effects due to the relatively long range (compared to the strong force) Coulomb nature of the protons and the isospin asymmetry of the nucleus, respectively. The Coulomb term accounts for the relatively long range, repulsive force between the protons in the nucleus and decreases the total binding energy. The asymmetry term accounts for the loss in binding energy from the interaction potential difference between like and unlike nucleons[7]. As the size of nuclei increase, an increasing number of neutrons are required to moderate the drop in binding energy due to increased Coulomb repulsion. Thus as nuclei size increase beyond ^{56}Fe, and as the neutron to proton ratio increases, the binding energy per nucleon decreases moderately. The final term, δ, accounts for the change in the nuclear binding energy due to pairing of nucleons. The pairing term increases the binding energy for even-even nuclei and decreases for odd-odd nuclei.

$$BE(MeV) = a_v A - a_s A^{2/3} - a_{Coul}\frac{Z^2}{A^{1/3}} - a_{sym}\frac{(N-Z)^2}{A} \pm \delta \tag{1.1}$$

The behavior of the nEoS in symmetric nuclear matter has been studied and is fairly well constrained at the saturation point, where E/A=-16MeV/nucleon and $\rho_0 \sim 0.16\text{fm}^{-3}$[8, 9, 4], in the ground state. However, the behavior of the nEoS in asymmetric matter is not well understood in regions far from normal nuclear density ($\rho/\rho_0 = 1$). At low densities ($\rho/\rho_0 \leq 1$), understanding the behavior of the nEoS is

important for describing the neutron skins of heavy elements, nuclear structure at the drip lines, and neutron star formation[10, 11, 12, 13].

The asymmetric part of the nEoS is typically described in parabolic form as in Eq. 1.2. The first term in Eq. 1.2 describes the energy per nucleon as a function of density in symmetric matter (where the number of neutrons, N, equals the number of protons, Z). The second term of the equation describes the effect of nuclear asymmetry (where N≠Z) as a function of density. The asymmetry term, I, is as described in Eq. 1.3.

$$\frac{E}{A}(\rho, I) = \frac{E}{A}(\rho) + E_{sym}(\rho)I^2 \tag{1.2}$$

$$I = \frac{\rho_n - \rho_p}{\rho_{total}} = \frac{N - Z}{A} \tag{1.3}$$

The symmetry energy can be described as the difference in energy between pure neutron matter and symmetric nuclear matter [14]. In other words, the amount of energy it would require to convert all the protons in symmetric matter to neutrons, forming pure neutron matter. At normal nuclear density, the symmetry energy term of the nuclear equation-of-state has been constrained between 28 and 32 MeV. While the current theoretical models do exhibit good agreement at saturation density, for the symmetry energy, there is a large divergence at densities above and below that of normal nuclear matter [4]. As nuclear density goes away from normal nuclear density toward the extremes (low and high nuclear density), the models begin to diverge based on the modeled interaction potential. Generally, an "asy-stiff", or "stiff", density dependence of the symmetry energy can be described as one that monotonically increases as a function of density. The "asy-soft", or "soft", density dependence of the symmetry energy, contrastingly, increases in energy until approximately the saturation density and then turns over (semi-parabolically) at higher densities. However,

this turn-over point is model dependent and there is some variability in the precise turn-over point.

There are many ways of probing the symmetry energy term of the nEoS. Astrophysically, the symmetry energy can help be constrained by observation of neutron star masses, radii, moments of inertia, and temperatures, as well as x-ray bursts[12, 15, 16, 17, 18, 19, 20]. However, the nEoS can also be explored in the laboratory by a variety of methods. There are a number of observables that can be analyzed when studying the nEoS using heavy-ion collisions. An increasing number of constraints have been placed on the nEoS, both at supra- and sub-saturation density, from a wide range of heavy-ion collision observables[21, 22, 23, 24, 25, 26, 27, 28, 29] and neutron skin thicknesses[30, 31, 32, 33]. Although there has been significant progress in recent years[23, 34, 35, 36], tighter and more robust constraints may be obtained by examining multiple observables for the asymmetry energy[37, 38].

1.2 Competition Between Reaction Mechanisms

In the energy regime just below the Fermi energy (E_F), near $E_{beam} \sim 10 - 15$ MeV/nucleon, the momentum and angular distributions, nucleon transport, and mass partitioning are predicted to be sensitive to the density dependence of the symmetry energy term of the nEoS and mean field interactions[11, 25, 39, 40, 41, 42, 43, 44, 45, 46, 47, 48, 49]. Nuclear reactions at these intermediate energies, just below E_F, present the possibility for probing dissipative mean field dynamics and nuclear material under extreme conditions (below normal nuclear density) that have been explored theoretically using post interaction deformation, angular momentum, and excitation energy measurements of the reacting nuclei. Typically, competition between fusion and quasi-fission dominate the reaction exit channels. Composite systems resulting from semi-peripheral collisions may exhibit a prolate (elongated)

shape with a large associated angular momentum. Reactions involving neutron-rich nuclei are expected to be particularly sensitive to the density dependence of the symmetry energy via observables such as dynamical ternary/quaternary breaking and massive fragment angular alignment. By increasing the mass, charge, and asymmetry of the reacting system, modes of projectile-target re-separation, other than binary deep-inelastic processes, become more prominent. In fact, it is suspected that these higher-order breakings are the precursor to neck fragmentation/emission at higher energies (30-50 MeV/nucleon)[50].

Ternary partitioning processes have been observed in early experiments [51, 52] where nearly equal size fragments were observed in Ar and Fe induced reactions on heavy targets at ∼10 MeV/nucleon. The results, however, did not allow for discerning sequential statistical fission of heavy composite nuclei resulting from dissipative heavy-ion collisions from dynamical processes that may have been present. Later, it was reported that a dynamic process was present in the ternary breakup in a number of events with nearly equal mass fragments[53, 54, 55]. Observations by Refs.[54, 55] using Mo and Sn systems, described effects of sequential, dynamical fragmentation of the quasi-projectile on a large background of statistical fission of the QP and QT (quasi-projectile and quasi-target). The QP and QT are defined, herein, as the hot primary fragments of the projectile and target just after interaction. More specifically, peaks in reaction plane angular distributions as well as relative velocity distributions of the detected fragments were observed. Both the angular alignment and relative velocities of the fragments were found to be correlated to the mass asymmetry of the detected fragments. Additionally, Charity et al. [56] noted that quaternary events of the same type were occurring, but, as earlier with the ternary partitioning, the statistical or dynamical nature of these events was unclear.

There has been a range of experimental work at or above the Fermi energy in

recent years[26, 50, 57, 58, 59, 60, 61, 62, 63, 64, 65, 66, 67, 68, 69, 70] utilizing systematic studies to explore the reaction dynamics and mechanisms in this energy range. Experiments detailed by Wilczyński[59, 60] and Skwira-Chalot[58] explored the dynamic processes of the heavy-ion reactions that tend to produce heavy fragments from the ternary and quaternary events. These events have been typically thought of as the result of highly deformed QPs and QTs from the initial interaction that then subsequently re-fission. These types of events were recently detected in the reaction of ^{197}Au +^{197}Au at 15 MeV/nucleon utilizing the CHIMERA[71] (Charged Heavy Ion Mass and Energy Resolving Arrary) detector array.

The results of the experiment showed that in sufficiently semi-peripheral reactions, the reacting nuclei are torn apart into three or four large fragments that were nearly aligned along a common re-separation axis. In the equilibrated (statistical) fission of the heavy fragments, the fragments tend to break isotropically. However, dynamical fissioning processes at this energy result in a strong angular alignment of the fragments. In the fast breakup, the fragments tend to be of comparable size in contrast to what has been described as the neck fragmentation process observed at higher bombardment energies[50, 58].

Simulations with QMD (quantum molecular dynamics) [72, 73] have been used in an attempt to describe the dynamical breakup resulting from the ^{197}Au +^{197}Au reactions. The simulation, however, predicts a slower break-up ($t \sim 3000$ fm/c) opposed to the experimental data at $t \sim 70 - 80$ fm/c. It is important to model the interaction with dynamical models such as CoMD-II (Constrained Molecular Dynamics)[74] and BNV (Boltzmann, Nordheim, Vlasov)[44] to validate the results of similar interactions in the range of ∼10-15 MeV/nucleon. However, there is not a broad range of data to sample in this energy regime that is a close comparison.

Furthermore, using source quadrupole/octupole moment analysis, intrinsic angu-

lar momentum, and excitation energy, the model shows it may to be possible to describe the competition between fusion and binary fission in addition to fast fission processes (ternary/ quaternary breakings) associated with the QP/QT sources[47, 48]. In theory, these momentum (and shape) fluctuations could be observable from lab frame preferential angular distributions of ternary/quaternary fission events due to the intrinsic spin of the system. While the theoretical simulations predict a long time scale (∼3000 fm/c) for the higher-order fission events, collective velocities, likely underestimated by SMF (stochastic mean field) calculations, could lead to a quickening of the sequential fragmentation process via more pronounced deformation[75]. Refs.[47] and [48] suggest the experimental measurement of these observables in lighter systems (near $A_{system} \sim 200$) with varying degrees of isospin asymmetry (at the same energy of 15 MeV/nucleon) as they have been predicted to be sensitive to the symmetry energy. Having both shape and angular alignment information is important to draw correlations between QP shape and time-to-breakup in these dynamical events.

At higher energies, closer to the Fermi energy, there has also been a great deal of experimental work done by the CHIMERA collaboration using reactions of ^{112,124}Sn with ^{58,64}Ni at 35 MeV/nucleon to investigate the fundamental mechanisms leading to fragment formation at intermediate energies[50, 63, 74]. The earlier experiments focused on exploring the characteristic features of heavy-ion reactions at intermediate energies where IMF production is progressively replaced by the vaporization of the nuclear system into light charged particles and nucleons as the energy transitions from lower to higher. In these cases, it was shown that experimental data was in some reasonable agreement with the results of simulations from CoMD-II and BNV-based transport models. Specifically, that the IMFs produced in the ternary breaking of the system were produced largely at mid-rapidity in a sequential decay

of the PLF on short time scales. Both models agreed with the experimental data in that these reactions were a different mechanism than that of Wilczyński [59, 60]and Skwira-Chalot[58].

The INDRA (Identification de Noyaux et Détection avec Résolutions Accrues) collaboration has also shown a number of works detailing the systematic studies of ^{129}Xe+^{nat}Sn at energies ranging from 8 to >29 MeV/nucleon[61, 64, 76]. This allows for the systematic investigation of reaction mechanisms as the system energy transitions from quasi-fission to multi-fragmentation. Adding to this systematic study is the recent work by Henry et al.[77] detailing lower energy data using ^{78}Kr+^{40}Ca at 10 MeV/nucleon with CHIMERA.

Experimental data by DeSouza and associates[65, 66, 67, 68, 69, 70] even further explores the contribution of dynamical processes in a wide range of systems, energies, and detector arrays. These experiments by DeSouza and associates provide a detailed description of IMF enrichment as a function of relative velocity and QP rotation. They further detail the correlation to the time to QP breakup after QP-QT separation. However, the data sets in these analyses are largely above the Fermi energy. It would be advantageous to extend these measurements to further investigate these dynamics below the Fermi energy.

Mid-rapidity emission of IMFs from sequential decay of the PLF near and above the Fermi energy is a fairly well established mechanism for semi-peripheral collisions. Much progress has also been made on determining the time of emission of these emitted fragments. However, when examining the mechanisms below the Fermi energy with heavy, asymmetric systems, there are a number of different mechanisms that have been observed. There appears to be a dependence on mass and energy of the primary fragments, entrance channel isospin content, and centrality of collision for examining the underlying dynamic mechanisms. Probing lower energies to examine

the transition from quasi-fission and deep-inelastic-transfer type reactions up through multi-fragmentation should allow for examining the role of density dependence of the symmetry energy. It has been predicted to be particularly sensitive in the energy regime for $E \sim 10 - 15$ MeV/nucleon.

1.3 Reaction Mechanism Competition and Probing the Symmetry Energy

Heavy-ion collisions provide a rich environment to probe the density dependence of the symmetry energy through observation of a range reaction mechanisms. The neck dynamics of these processes have been found, by transport models, to be influenced by the symmetry energy below saturation. The breakup probability of the hot, primary fragments (QP or QT) are predicted to be governed by the deformation of the QP/QT shortly after interaction. Larger deformations are predicted to be more prevalent in the "asy-stiff" case due to lower nucleon repulsion in the low density neck region during initial re-separation.

The longer predicted lifetime of this low density, neutron-rich neck region provides for the extended time required to produce very deformed primary fragments. This allows for the possibility of dynamically emitted small clusters from this low density neck region. This types of breakup is observable through detection of an emitted heavy fragment ($Z \geq 3$) coincident with a PLF. The angular alignment between the two may give some insight into the state of the QP at the time of breakup and whether the IMF cluster was emitted from the neck at mid-rapidity or at a later time via sequential decay. The highly excited QP/QT at more peripheral impact parameters are predicted to lead to ternary fragmentation events[48] where the QP breaks up into an IMF cluster and a PLF. These would be differentiable from neck emission via the angular alignment information between the two resultant fragments.

Neck fragmentation mechanisms play an important role in intermediate energy

HICs, with IMFs being produced directly in the interacting zone of semi-peripheral collision on short time scales. This mechanism can form light clusters in the dilute contact region between the QP/QT remnants near normal densities. Therefore, it is expected that there is a stronger neutron flow to the neck region in the "asy-stiff" case of the symmetry energy[13]. These isospin dynamics can be extracted from correlations between N/Z, alignment (anisotropic, non-statistical angular correlations), and the deduced emission times of the detected IMFs. Neutron migration to the neck and the resulting neutron enrichment of the neck region is predicted to scale with the slope of the symmetry energy (commonly referred to the "stiffness" or "softness" of the symmetry energy)[45]. The alignment between IMF and PLF has been shown to be very promising for probing the originating mechanism of mid-rapidity IMFs on short time scales[65, 66, 67, 68, 69, 70]. Anisotropic IMF angular distributions indicate a preferential emission; as the neck becomes more neutron enriched, the deformation and angular momentum of the QP increases[40]. Angular alignment of the resultant PLF close to the QP-QT separation axis with a high relative velocity suggests the IMF may have been emitted from the neck region[55].

Ternary (possibly quaternary) events with a direct IMF emission at less than 250-300 fm/c result in generally less deformed QP (QT), but this direct emission is still a rare occasion. The predicted best probability of observing these ternary fragmentation events is exhibited at semi-peripheral impact parameters between $b = 5$ fm and $b = 8$ fm. The IMFs originating from neck fragmentation appearing $t \sim$150 fm/c after interaction, just as the neck begins to break up, exhibit a strong correlation to the reaction mechanism and kinematical correlations via emission time and mass asymmetry[11, 41, 43, 46, 47, 48, 49]. BNV transport models with dynamical fluctuations[78] coupled with stochastic density fluctuation models[79, 80] have shown a varying degree of deformations associated with dynamical break-up

mechanisms[11, 41, 43, 46, 47, 48, 49].

While the previous observables lend themselves to deep insight into the initial reaction/breakup mechanism, there is also predicted sensitivity to the symmetry energy via isospin dynamics. For instance, examining the isospin content (Eq. 1.3) of neck emitted IMFs provides some sensitivity to the density dependence of the symmetry energy[44]. This comparison appears to have a strong dependence on the symmetry energy for given soft, stiff and super-stiff nEoS over several impact parameters. Systematically, there are more neutron-rich IMFs predicted in the asy-stiff nEoS[11, 39] with a strong dependence on the symmetry energy. More importantly, it has been observed experimentally that there is an appreciable difference in the IMF asymmetry when looking at dynamically vs. statistically emitted IMFs[11, 65, 66, 67, 68, 69, 70]. However, there has been a recent proposal in the community to consider the analysis of multiple observables simultaneously[37, 38]. This multi-dimensional approach may provide insight as to affects of the symmetry energy on the dynamical evolution of the reaction system.

1.4 Outline of Thesis

The work presented in this thesis studies and expands upon some of the limitations in previous work. This work studies the data from three different reaction systems accounting for both Z and isospin effects: ^{136}Xe+^{64}Ni, ^{124}Xe+^{58}Ni, ^{124}Sn+^{64}Ni at 15 MeV/nucleon. The purpose of this work is three-fold. First, this work systematically extends the CHIMERA collaboration analysis of angular distributions with respect to the heavy fragments resulting from a ternary breaking of the reaction system. This work also focuses on examining how the dynamical environment evolves from quasi-fission to multi-fragmentation as a function of mass, asymmetry and energy of the colliding system using lower energy reactions. We explore the dynamical

and statistical contributions to this ternary breaking of the reaction system to better understand the underlying dynamics in this energy regime and how it correlates to higher energies. Second, the quadrupole moment of the hot QP has been predicted to be sensitive to the symmetry energy in this energy regime [11, 44, 41, 47, 48, 49] with little experimental validation. A qualitative surrogate was used to probe shape information via a velocity quadrupole measurement as a means to probe the shape of the QP in velocity space. We investigate the correlation between the break-up alignment and the qualitative shape of the QP just before breaking up. This is important to understanding how the shape contributes to the dynamical breaking of the QP. We have recently built a new beam line to collect data for this analysis. Third, recent work has been published in an attempt to take a first step in examining multiple observables sensitive to the symmetry energy simultaneously[81]. The first step proved promising in examining theoretical models. This work examines the power of machine learning via simulations that have been experimentally filtered and the effects of secondary decay on the analysis.

In Section 2, a brief overview of the different theoretical models used in this work is provided. Section 3 provides a detailed discussion on the experimental details of the detector upgrade, particle identification, and energy calibrations used in this thesis. Some details about the optics of the newly constructed FAUST-QTS beam line (Section 3.2) are detailed in Section 4. Analysis of experimental and theoretical reaction plane correlations is presented in Section 5 with QP momentum fluctuations analysis presented in Section 6. Section 7 examines the use of multidimensional analysis in examining observables theoretically sensitive to the symmetry energy with Section 8 detailing the multidimensional analysis of simulated observables, but with experimental constraints imposed. Finally, in Section 9, a summary of this thesis work is presented.

2. SIMULATIONS

The theoretical calculations in this dissertation involve three different types of simulations. The two types that will be discussed in the following sections are: Dynamical Simulations (Section 2.1) and Statistical Simulations (Section 2.2). Specifically, Section 2.1 will discuss the use of the Constrained Molecular Dynamics model[3] (CoMD) and the Stochastic Mean Field model[47, 82] (SMF) to simulate dynamical nuclear interactions. Section 2.2 will discuss the use of the GEMINI[83, 84, 85] used for cooling of the dynamically made fragments in an effort to describe possible secondary, statistical decay effects.

2.1 Dynamical Simulations

The dynamical simulations discussed herein are used in order to model the time dependent interaction of heavy-ion collisions. Of the two dynamical reaction models used for this thesis, one was a molecular dynamics mode (CoMD) and the other was a test-particle based transport model (SMF).

2.1.1 Constrained Molecular Dynamics (CoMD)

The Constrained Molecular Dynamics model[3] describes each nucleon semi-classically as a Gaussian distribution function, $f_i(\mathbf{r}, \mathbf{p})$, in position and momentum space where $\mathbf{r}$ and $\mathbf{p}$ are the position and momentum vectors of the i^{th} particle respectively. In Equation 2.1, the Gaussian distribution is described as:

$$f_i(\mathbf{r}, \mathbf{p}) = \frac{1}{(2\pi\sigma_r\sigma_p)^3} \cdot \exp\left[-\frac{(\mathbf{r} - \langle\mathbf{r}_i\rangle)^2}{2\sigma_r^2} - \frac{(\mathbf{p} - \langle\mathbf{p}_i\rangle)^2}{2\sigma_p^2}\right] \tag{2.1}$$

where σ_p and σ_r represent the widths of the Gaussian distributions in momentum and position space respectively. The terms $\langle\mathbf{p}_i\rangle$ and $\langle\mathbf{r}_i\rangle$ describe the centroid of

the momentum and position phase spaces respectively. The equations of motion are derived via the time-dependent variational principal[86] yielding

$$\langle \dot{\mathbf{r}} \rangle_i = \frac{\partial H}{\partial \langle \mathbf{p}_i \rangle} \ , \ \langle \dot{\mathbf{p}} \rangle_i = \frac{\partial H}{\partial \langle \mathbf{r}_i \rangle} + \mathbf{C}_i + \lambda_{\mathbf{i}} + \mathbf{P}_{\mathbf{i}} + \mathbf{R}_{\mathbf{i}}, \tag{2.2}$$

where $\mathbf{P}_i$ represents the impulsive forces invoked when the Pauli condition is violated, $\mathbf{C}_i$ represents the strong repulsive, short-range nuclear interaction, $\mathbf{R}_i$ is a transformation that corrects the angular momentum conservation of the system, and $\lambda_{\mathbf{i}}$ accounts for frictional forces. The terms $\mathbf{r}$ and $\mathbf{p}$ are the position and momentum vectors as defined previously. The kinetic energy of the two-body interaction is contained in the Hamiltonian, H, described in Eq. 2.3

$$H = \sum_i \frac{\langle \mathbf{p}_i \rangle^2}{2m} + \frac{1}{2} \sum_{ij \neq i} V_{ij} + 3\frac{\sigma_p^2}{2m}, \tag{2.3}$$

where V_{ij} represents the two-body interaction between particles i and j.

More importantly, the CoMD model allows for the consideration of the Pauli Exclusion Principle. The average occupation number ($\bar{f}_i$) is calculated for every t = 1 fm/c during the simulation. If in the time step $\bar{f}_i > 1$, a violation of the Pauli Principal, CoMD executes an algorithm to randomize the momentum of the nearest-neighbor particles while conserving total energy and momentum of the system by the Monte-Carlo method. This process is continued until $\bar{f}_i < 1$. The treatment of the Pauli Principal in this way also allows for increased computational speed. This is largely based on the N^2 dimensionally of the momentum space imposed by the two-body character of the effective interaction. This pales in comparison to the N^4 dimensionality prescribed by anti-symmetric dynamics. This dimensionality difference allows for the CoMD model to propagate the reaction over longer time

scales (t = 3000 fm/c), allowing the system to evolve and cool dynamically, within a reasonable computational time-frame. It has been shown that on these longer time scales, the need to statistically cool the system any further produced little to no noticeable difference in the resulting reaction products for reaction systems above the Fermi energy[87].

A momentum-independent form of the Skyrme interaction was used in the calculation producing an nEoS with a compressibility of K = 200 MeV. It was then possible to vary the symmetry energy term of the Skyrme interaction while holding the compressibility term constant. This allowed for the investigation of the effects of the density dependence of the symmetry energy on reaction mechanisms in this dissertation.

2.1.2 Stochastic Mean Field Model (SMF)

The Stochastic Mean Field model [82, 47, 88, 78] describes the time evolution of the reacting system using the Boltzmann-Langevin equation (BLE) [89, 90]. The BLE is the fluctuation term contained within a Boltzmann-Nordheim-Vlassov type transport equation and can be described as

$$\frac{df}{dt} = \frac{\partial f}{\partial t} + \{f, H\} = I_{coll}[f] + \delta I[f], \tag{2.4}$$

where $f(\mathbf{r}, \mathbf{p}, t)$ is the one-body distribution function and $H(\mathbf{r}, \mathbf{p}, t)$ is the mean-field Hamiltonian. The notation { , } denotes the normal Poisson brackets. Thereby, $\{f, H\}$ describes the time evolution of the one body distribution $f(\mathbf{r}, \mathbf{p}, t)$ using Hamiltonian equations of motion, $H(\mathbf{r}, \mathbf{p}, t)$. The term I_{coll} represents the two body collision term (including Uehling-Uhlenbeck collision term) and $\delta I[f]$ is the fluctuating term of the collision integral, otherwise known as the Langevin term.

The test particle method[91, 92] was used to approximate the solutions to the

BLE. The full BLE is not yet available in three dimensional space[47], thus approximation methods, such as SMF, are utilized through the implementation of stochastic density fluctuations in coordinate space. For situations far from spherical shapes, such as those of interest in this dissertation, thermal fluctuations in the Langevin term can induce conditions that may eventually lead to dynamic break-up channels. The fluctuations can be numerically repeated, creating random perturbations in the spatial density of the system, reproducing many of the observations made in studying heavy-ion collisions. Among the results of the perturbations in spatial density are fluctuations in the collective velocity. These fluctuations in collective velocity are associated with shape deformations, particularly quadrupole or octupole deformations, that may lead to rather elongated shapes in the system. From these elongated shapes, it is expected that the system could subsequently break into three or four heavy partners.

The nuclear equation of state, directly coupled to the mean-field Hamiltonian, can be written in parabolic form

$$\frac{E}{A}(\rho, I) = \frac{E_s}{A}(\rho) + C_{sym}(\rho)I^2, \tag{2.5}$$

as it typically is, where $I = (N - Z)/A$ is defined as the asymmetry parameter and

$$C_{\rm sym}(\rho) = a\left(\frac{\rho}{\rho_0}\right)^{2/3} + b\left(\frac{\rho}{\rho_0}\right) \tag{2.6}$$

describes the density dependance of the symmetry energy where constants a and b are determined by phenomenological fit. In this way, variations are introduced into the model to study the effect of the density dependence of the symmetry energy. Output from the SMF model was subsequently treated with a phase-space coales-

cence code[92]. The coalescence code was applied to the test particle distribution to determine the identities of the fragments representing the phase space of the hot primary fragments.

2.2 GEMINI Statistical Decay Simulation

The GEMINI code[83, 84, 85] is a statistical decay code written in C++ that can be integrated directly with ROOT. Within GEMINI, the excitation energy, angular momentum, mass and charge of the hot fragments are used to calculate the statistical decay path. The decay path is determined by Monte Carlo method through a series of sequential decays from the hot fragment. The decay widths of the light charged particles (n, p, d, t, ^{3}He, α, ^{6}He, and $^{6-8}$Li) are calculated by the Hauser-Feshbach formalism[93]. The partial decay width of the parent fragment of excitation energy E^* and spin S_{frag} for the i^{th} particle, according to the Hauser-Feshbach formalism, is described by

$$\Gamma_i^{HF} = \frac{1}{2\pi\rho_{frag}(E^*, S_{frag})} \int d\varepsilon \sum_{S_d=0}^{\infty} \sum_{J=|S_{frag}-S_d|}^{S_{frag}+S_d} \sum_{\ell=|J-S_i|}^{J+S_i} T_\ell(\varepsilon)\rho_d(E^* - B_i - \varepsilon, S_d) \quad (2.7)$$

where S_d is the spin of the daughter nucleus, S_i, J, and ℓ are the spin, total and angular momenta of the evaporated particle. The parameters ε, B_i, and T_ℓ are the kinetic energy, separation energy and transmission coefficient of the evaporated particle. The level density of the daughter and parent nucleus is described by ρ_d and ρ_{frag} respectively. The transmission coefficient is described by a simplistic scheme, described in Eq. 2.8, to incorporate the effects of barrier distributions under the assumption that parent nucleus shape fluctuations are thermally induced and the

variance is proportional to temperature.

$$T_\ell = \frac{T_\ell^{R_0-\delta r}(\varepsilon) + T_\ell^{R_0}(\varepsilon) + T_\ell^{R_0+\delta r}(\varepsilon)}{3}. \tag{2.8}$$

This scheme describes the average of three incoming-wave boundary-condition models in order to maintain real optical model potentials using three different radii for the nuclear potential. The radii R_0 values are derived from fits to the global optical model with $\delta r = w\sqrt{T}$ in order to be consistent with thermal fluctuations. The value of parameter $w = 1.0$ fm as obtained from fits to experimental data. Nuclear level density parameters, ρ_d and ρ_{frag}, are derived from the Fermi-gas model in that

$$\rho(E^*, J) \propto (2J+1) exp\left[2\sqrt{a(U,J)U}\right]. \tag{2.9}$$

The level desity parameter is described by a and U describes the thermal excitation energy, such that

$$U = E^* - E_{rot}(J) + \delta P \tag{2.10}$$

where δP is the pairing correction to the empirical mass formula and $E_{rot}(J)$ describes the rotational energy of a spherical nucleus with a fixed moment of inertia.

The fission channel is calculated from the Bohr-Wheeler formalism[94] as described by

$$\Gamma^{BW} = \frac{1}{2\pi\rho_{frag}(E^*, S_{frag})} \int d\epsilon\ \rho_{saddle}(E^* - B_f(S_{frag}) - \epsilon) \tag{2.11}$$

where ρ_{saddle} describes the level-density at the saddle point, ϵ describes the kinetic energy of the fission degree of freedom, and $B_f(S_{frag})$ describes the spin-dependent saddle-point (transition state) energy. This, however, has been adjusted by Charity

et al.[83, 84] to account for mass and charge asymmetry of the parent fragment via

$$\Gamma_{Z,A}^{BW} = \frac{1}{2\pi\rho_{frag}(E^*, S_{frag})} \int d\epsilon \; \rho_{saddle}(E^* - B_{Z,A}(S_{frag}) - \epsilon) \tag{2.12}$$

where $B_{Z,A}(S_{frag})$ now allows for an estimation of the mass and charge dependence of the fission barrier based on liquid drop model calculations. Additionally, the gamma-ray emission decay width can also approximated from the GEMINI model. However, this occurs on longer times than we are interested in and is beyond the scope of this thesis.

The GEMINI code was used (in some instances) as an afterburner to the dynamical CoMD simulations after $t = 3000$ fm/c. However, it is important to recognize that several assumptions are made in this process. The GEMINI code assumes a spherical, hot nucleus at normal nuclear density ($\rho_0 = 0.16 \; fm^{-3}$) as an input fragment. However, the dynamical simulation outputs are rarely in this state; the fragments from the dynamical simulations are likely to be deformed to some degree and at a density below ρ_0. This likely affects the decay process. Additionally, after the completion of the decay, GEMINI defines the final fragment trajectories and no additional nuclear or Coulomb forces are considered. The GEMINI code used herein was coupled directly to the analysis code such that the C++/ROOT version of GEMINI was used in-line to decay hot fragments from the dynamical simulations.

3. EXPERIMENTAL

The reactions of ^{136}Xe,^{124}Sn+^{64}Ni and ^{124}Xe+^{58}Ni at 15 MeV/nucleon were studied at the Texas A&M Cyclotron Institute. The FAUST-QTS (Forward Array Using Silicon Technology[95] - Quadrupole Triplet Spectrometer[96, 97, 98, 99, 100]) was used to collect heavy fragments ($Z \geq 3$) from the dynamical breakup of the excited projectile in inverse kinematics. This new experimental beam line was specifically designed for intermediate energy reaction dynamics studies where the collection of the heaviest fragment at small angles ($\theta = 0.5°$-$0.9°$) up to the minimum angle that is covered by the FAUST array ($\theta = 1.63°$-$2.3°$) is desired. The FAUST array provides forward coverage for charged particle detection (via ΔE-E or E-ToF identification) and the QTS provides mass identification of heavy, projectile-like fragments (PLFs) or heavy evaporation residues. Mass asymmetric systems in inverse kinematics are a good match for this arrangement especially in this energy regime. These systems were also chosen as they are a close match to the theoretical systems used by Baran, Di Toro and Colonna et al.[11, 25, 41, 44, 45, 47, 48], where they have shown that on long time scales, the hot, deformed quasi-projectile could dynamically break. The deformation, angular and velocity correlations and mass partitioning of the intermediate mass fragments have been predicted to be sensitive to the symmetry energy. More specifically, these reaction dynamics observables associated with 3- and 4-body breakup of the reaction systems are predicted to be particularly sensitive to the symmetry energy at beam energies below the Fermi energy.

In this section, the experimental details are discussed in Section 3.1. Details concerning the FAUST array, the QTS and Data Acquisition are covered in Section 3.2. The particle identification (PID), energy, and time-of-flight calibrations are

detailed in Sections 3.3, 3.4, and 3.5 respectively. Production of the physics tapes is described in Section 3.6. Finally, the FAUST-QTS geometry and energy thresholds derived from the physics tapes were implemented in the FAUST software filter and discussed in Section 3.7.

3.1 Experiment

The K500 Super-Conducting Cyclotron at Texas A&M University Cyclotron Institute was used to produce beams of ^{136}Xe, ^{124}Xe and ^{124}Sn at 15 MeV/nucleon. The ^{136}Xe and ^{124}Sn beams were collided on a self supporting ^{64}Ni target and the ^{124}Xe beam was collided on a self supporting ^{58}Ni target. The targets were fabricated by iThemba labs[101] with materials purchased from Trace Sciences[102]. Details of the reaction systems, including charge state, system $\frac{N-Z}{A}$, target thickness, and target purity are detailed in Table 3.1. The beam intensity was chosen such that the rate of coincident events between FAUST and the QTS were maximized while minimizing the damage to the forward Si detectors in FAUST and the QTS. Beam rate averaged $\sim$1.50 x10^5 particles per second corresponding to $\sim$20 electical pA on Faraday cup# 2 (FC02) just outside of the K500 deflector.

Table 3.1: Projectile energy, projectile charge state, system $\frac{N-Z}{A}$, target thickness, and target purity for each reaction system

Reaction	^{136}Xe+^{64}Ni	^{124}Xe+^{58}Ni	^{124}Sn+^{64}Ni
Projectile Energy (MeV/u)	15	15	15
Projectile Charge State	29+	26+	26+
System $\frac{N-Z}{A}$	0.1800	0.1702	0.0989
Target Thickness (mg/cm^2)	1.05	1.02	1.05
Target Purity	97.2%	97.2%	97.2%

Additionally, the K500 Cyclotron also produced three calibration beams which were collided on gold targets (^{197}Au). The details of these calibration beams are tabulated as shown in Table 3.2. The calibration beams were chosen in order to produce well defined energy calibration points in both the FAUST array and the Quadrupole Triplet Spectrometer. The range of beams and energies were chosen to provide calibration points based on the type and energy of incident charged particle.

Table 3.2: The beam-target combinations and energy for the calibration beams

Calibration Beam	^{40}Ar	^{22}Ne	^{4}He
Beam Energy (MeV/u)	24.8	24.8	15.0
Target	^{197}Au	^{197}Au	^{197}Au

3.2 FAUST-QTS Experimental Details

3.2.1 FAUST Array

The FAUST array [95] is composed of 68 Si-CsI(Tl) ΔE-E telescopes arranged into five concentric rings, A-E. The rings can be described as rings of squares (detectors) projected on an imaginary sphere. Each Si-CsI(Tl) telescope consists of an edge mounted, 2 x 2 cm by 300μm thick silicon detector followed by a CsI(Tl) inorganic, scintillation crystal read-out by photodiode. In rings A-D, the CsI(Tl) crystals are 3 cm in length with the CsI(Tl) crystals in ring E measuring 2.64 cm in length. Since FAUST is arranged as a set of squares projected on a sphere, there are 13 different detector position combinations between the five rings of FAUST. A cross-sectional view of the FAUST array is shown in Figure 3.1 and a 3D representation

in Figure 3.2. This detector arrangement combined with the single-edge mounting

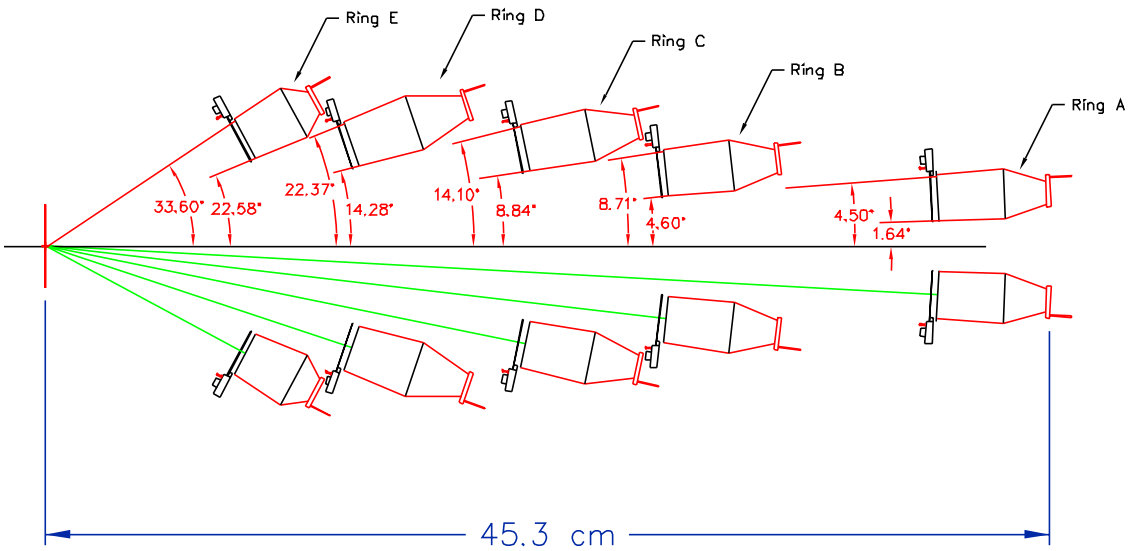

Figure 3.1: Cross Sectional view of the FAUST array. Angles shown are for the center minimum and maximum points of the shown detectors.

of the silicon wafers allows for the inactive area (wafer mounts) to be shadowed by the active area of the ring immediately in front, thus allowing for maximum solid angle coverage. The FAUST arrangement provides over 89.7% solid angle coverage from 2.3°-33.6° with additional coverage from 1.64°-2.3° and 33.6°-44.95°[95] in the laboratory frame of reference. Table 3.3 details the angular coverage by detector ring and position within the ring. Additionally, 1.4 μm thick aluminized mylar foils were placed in front of rings A, C, and E to help attenuate electrons and maximize isotopic resolution. The foil in front of ring C shields rings B and C, while the foil in front of ring E shields rings D and E. This thickness was chosen for this experiment to minimize the resolution loss due to scattered electrons while also allowing the heavy, projectile-like fragments produced in the reactions of interest to have the minimum

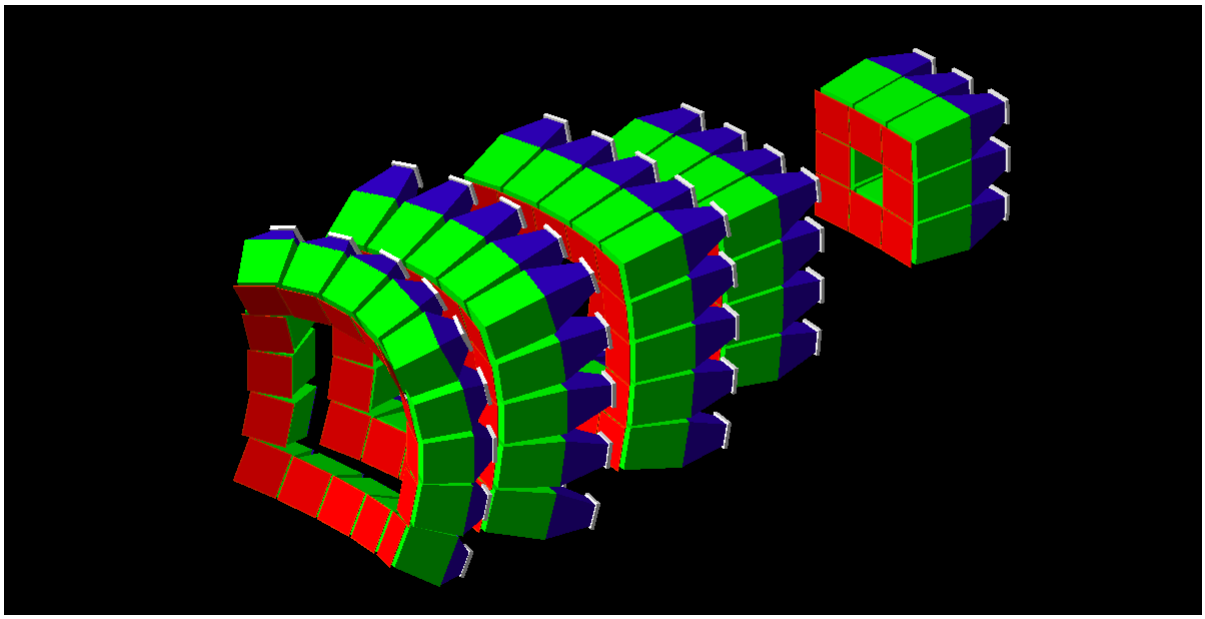

Figure 3.2: A 3D rendering of the FAUST array from the GEANT4 environment.

energy loss through the mylar foil.

Table 3.3: The angular coverage of the FAUST array by detector type with associated ring designation and detector numbers

Ring	Detector Position	Detector #'s	Angular Coverage (degrees)
A	Center	1, 3, 5, 7	1.64 - 4.44
A	Corner	0, 2, 4, 6	2.30 - 6.36
B	Center	9, 10, 12, 13, 15, 16, 18, 19	4.60 - 8.71
B	Corner	8, 11, 14, 17	6.47 - 12.28
C	Center	22, 26, 30, 34	9.20 - 14.34
C	Intermediate	21, 23, 25, 27, 29, 31, 33, 35	9.31 - 16.33
C	Corner	20, 24, 28, 32	12.23 - 19.73
D	Center	38, 42, 46, 50	14.84- 22.683
D	Intermediate	37, 39, 41, 43, 45, 47, 49, 51	14.79 - 25.66
D	Corner	36, 40, 44, 48	19.42 - 30.77
E	Center	54, 58, 62, 66	23.29 - 34.05
E	Intermediate	53, 55, 57, 59, 61, 63, 65, 67	23.37 - 38.11
E	Corner	52, 56, 60, 64	29.34 - 44.95

The FAUST array was chosen for its good isotopic and elemental resolution, forward angular coverage and reasonable angular granularity. The design of FAUST also allows for the possibility of upgrading electronics to suit the needs of the experiment. Since the physics of this experiment demanded elemental resolution identification of intermediate mass fragments (IMFs), the FAUST array provided a good platform for detecting the IMFs of interest for this experiment.

3.2.2 FAUST Array Upgrade

The original CsI(Tl) preamplifiers for this experiment were replaced with Zepto systems preamplifiers[103] and were relocated external to the vacuum chamber. Additionally, in the current rendition of the FAUST preamplification electronics, the external FAUST Si detector preamplifiers were replaced with new charge-sensitive timing pick-off (CS-TPO) preamplifiers and motherboards from RIS-Corp[104] for Rings A-D. As before, the new CS-TPO preamplifiers were mounted directly to the front flange of the FAUST array vacuum chamber upstream of the FAUST detector (Figure 3.3). The new CS-TPO preamplifiers occupy a slightly larger footprint than the Zepto systems preamplifiers, shown side-by-side in Figure 3.4, with two additional pins for timing and fit in newly designed RIS-Corp motherboards. The new motherboards, shown in Figure 3.5, have a 16-channel (34-pin header) connector for the detector input from each ring and two 16-channel connectors for separate energy and timing output signals directly from the preamplifiers. The timing on the new CS-TPO preamplifiers is accomplished by detecting charge fluctuations at the detector input to the charge sensitive portion of the CS-TPO. Specifically, the change in JFET current is passed through the emitter of the pnp transistor (connected to the JFET source/emitter) and is amplified to provide a timing signal in the amplifier circuit shown in Figure 3.6. The timing works because there is a sharp change in

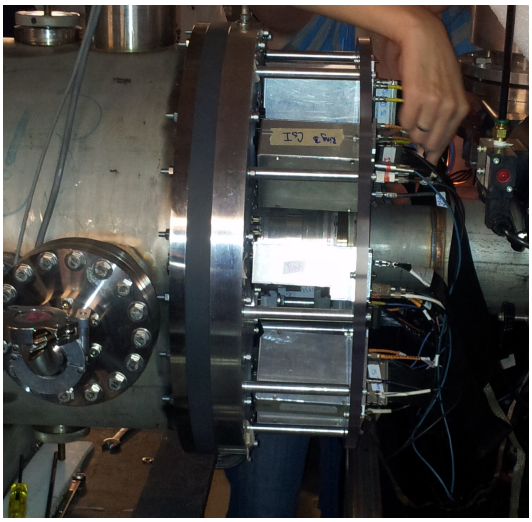

Figure 3.3: Preamplifier boxes mounted directly to the front of the FAUST vacuum chamber.

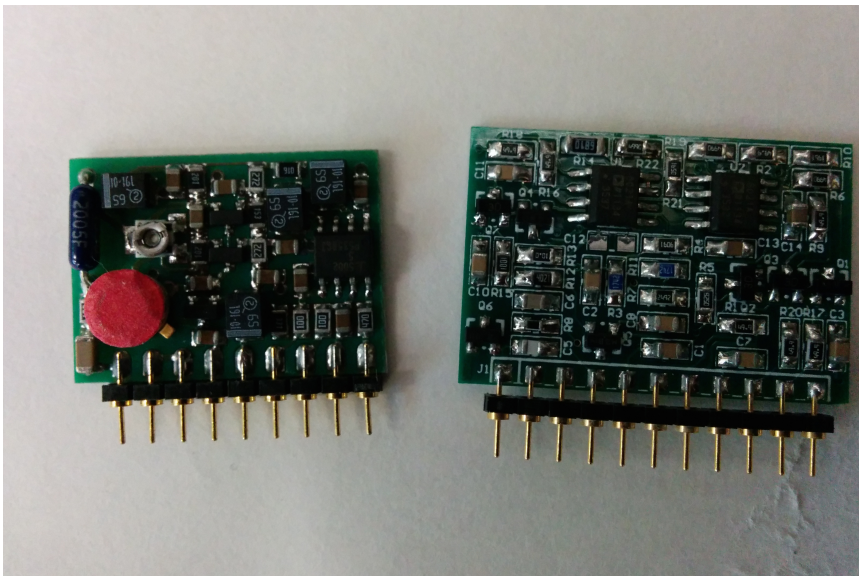

Figure 3.4: Zeptos Systems preamplifier (left) and RIS-Corp preamplifier (right) shown side-by-side.

JFET current for the time it takes to collect the charge deposited by the particle of interest in the detector. This change in current (flux) generates the timing signal.

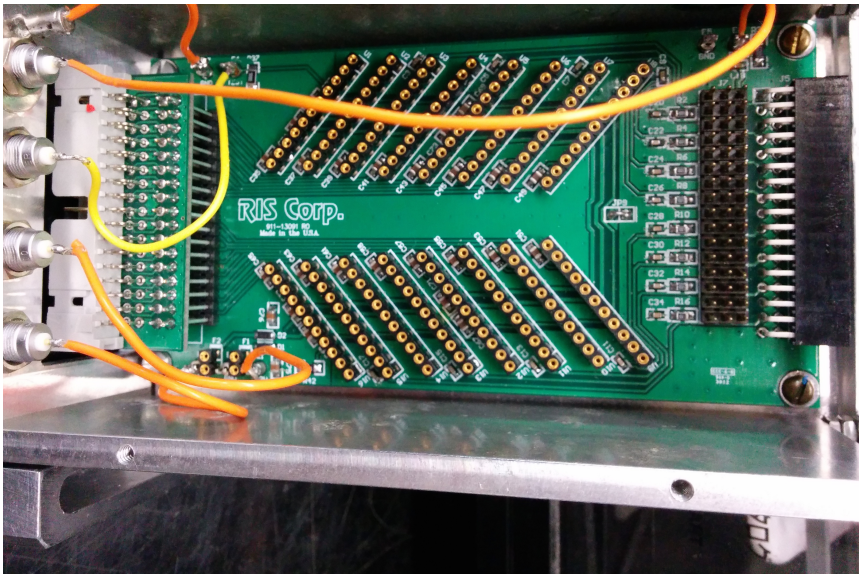

Figure 3.5: Top view of new RIS-Corp preamplifier motherboards.

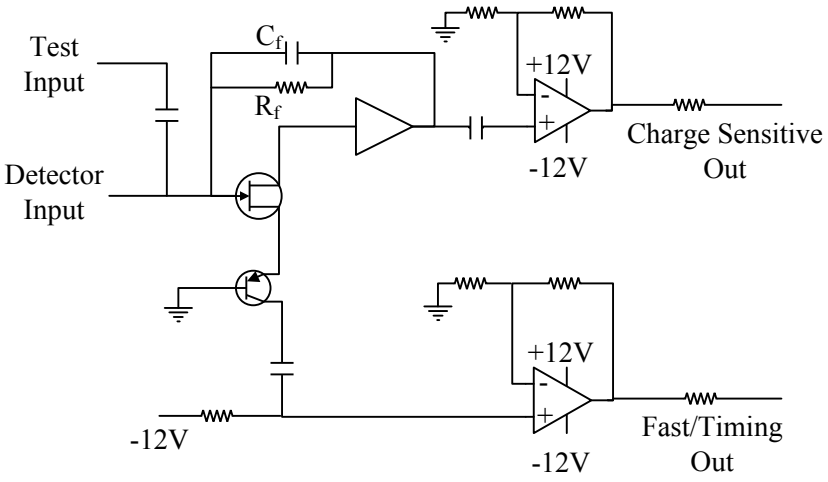

Figure 3.6: Brief schematic of the RIS-Corp charge sensitive, timing pick-off preamplifiers.

This signal is then integrated to generate a voltage signal with ∼1ns rise time. This allows for fast-timing of the incident particle simultaneously with charge sensitive

pre-amplification in one integrated circuit chip-set without added bulk or additional cabling between detector output and fast timing circuitry.

In the lab, we were able to achieve a time resolution of up to ∼150 ps full-width half-max (FWHM), as seen in Figure 3.7. This ideal resolution was possible because of a small angular coverage of the detector due, largely, to distance from the source, low noise background and single isotope analysis. However, in the actual experiment, we were able to achieve a maximum timing resolution of ∼400ps. This was highly dependent on the condition/level of radiation damage, background noise, larger solid angula coverage (θ ∼8°) and a wider range of isotopes detected at varying energies on each individual silicon detector. On average, most silicon detectors had a timing resolution between 600-1200ps during the actual experiment.

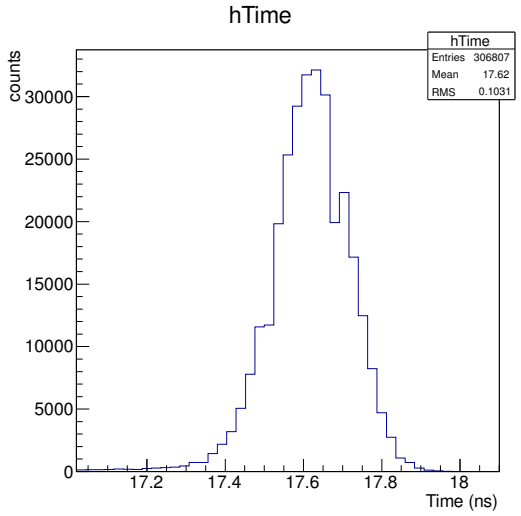

Figure 3.7: Preamplifier resolution in a best case scenario using a plastic scintillator and FAUST silicon detectors. Maximum resolution is on the order of 150 ps at full-width half-maximum. Particles detected were ^{129}Xe at 15 MeV/nucleon beam particles detected on beam center.

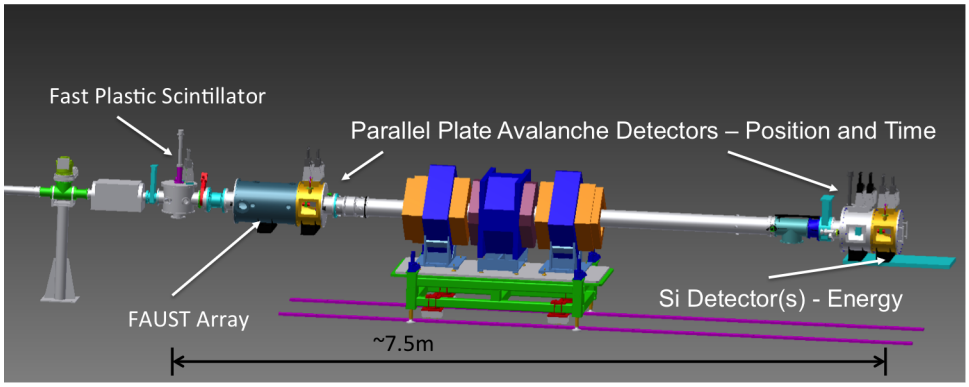

Figure 3.8: A 3-dimensional rendering of the FAUST-QTS beam line showing detector and beam-line component positioning.

Figure 3.9: Image of the fast plastic scintillator (BC-408) mounted in its custom housing with mylar windows installed. The Hammamatsu R1635 photomultiplier tube is typically mounted to the windows on the left or right hand side of the housing (not shown).

The fast plastic scintillator, used in both laboratory testing and online in the beam experiment, was a 10 μm thick, BC-408 fast scintillating plastic. The plastic was mounted and glued with optical cement (BC600) between two pieces of lucite. This puck was wrapped in 2.4μm Mylar, then mounted inside a custom fabricated housing (Figure 3.9) upstream of the FAUST array (Figure 3.8). The light generated

by the BC408 plastic was then read out with a Hammamatsu R1635 photomultiplier tube and used as a common stop in the timing electronics after 135 ns of delay.

Figure 3.10: Quadrupole Triplet Spectrometer, days after installation showcasing the triple quadrupole magnets.

3.2.3 Quadrupole Triplet Spectrometer

The Quadrupole Triplet Spectrometer (QTS), as seen in Figure 3.10, consists of three large bore (∼8 inch inner diameter) quadrupole magnets focusing in the X-, Y-, and then X-direction (respectively) relative to the beam axis (Z-axis) in the laboratory frame of reference. The spectrometer also consists of two customizable detection chambers, one before and one after the magnets, to allow E-ToF mass PID and/or ΔE-E isotopic identification depending on the energies of the particles of interest. For this experiment we employed the E-ToF mass PID. This was accomplished using a Parallel Plate Avalanche (PPAC) detector before and after the quadrupole triplet

for accurate time of flight measurement and a 5 cm x 5 cm, 1000 μm thick silicon detector for accurate particle energy measurement. The 5 cm x 5 cm, quadrant segmented silicon semiconductor detector was chilled to 5°C with thermal and vibrational isolation. In this way, it was possible to calculate the particle's mass based on the time of flight, energy and particle flight path length, as seen in Figure 3.8 (3D rendered beam line). The total particle flight path length was 547.6 cm between PPACs. Particle energy calibrations were performed with elastically scattered beam particles and the calibration beams listed previously in Table 3.2. A 1/4 inch thick aluminum collimator was placed just upstream of the 1000μm silicon detector in order to decrease the rate of elastically scattered beam particles. The magnets and rear detection chamber for the QTS had been previously used in a number of campaigns with BigSol[96, 97, 98, 99, 100] focused on production of radioactive ion beams.

Table 3.4: The reaction system equilibrium charge state and magnetic rigidity for transport calculations

Reaction	^{136}Xe+^{64}Ni	^{124}Xe+^{58}Ni	^{124}Sn+^{64}Ni
Mean Equillibrium Charge State	49+	49+	48+
Magnetic Rigidity (T m)	1.552	1.445	1.542

Optimal settings for each experimental reaction system were determined through a series of optical transport calculations. Basic, 1st order optics were calculated analytically using the TRANSPORT[105] code based on the flight path of the beam through FAUST-QTS to the detection plane behind the spectrometer. The magnetic rigidity (Bρ) of each beam/target combination in its equilibrium charge state, tabulated in Table 3.4, was used for this calculation. This allowed for the determi-

nation of the base magnetic field settings (in kiloGauss) for the spectrometer and was the basis for the higher-order calculations used in RAYTRACE[106] and COSY-Infinity[107]. Magnet current settings for the actual experiment were determined by using the measured minimum current to generate a magnetic field as measured by a Hall probe. These currents were then compared to previous campaigns of experimental data[96, 97, 98, 99, 100] taken with the QTS. A linear fit for current(A) as a function of Bρ was obtained. The empirical function, current (A) for a given Bρ (T m), is shown in Table 3.5.

Table 3.5: Empirical Bρ to current equations for each for the three quadrupole magnets in the QTS.

Magnet	Q26	Q27	Q28
Empirical Current (A)	$86.61\cdot\left(\frac{B\rho}{1.962}\right)$	$657.76\cdot\left(\frac{B\rho}{1.962}\right)$	$78.04\cdot\left(\frac{B\rho}{1.962}\right)$

Results obtained for each reaction system from DIT[108]+GEMINI[83] and CoMD[3] were used for RAYTRACE[106] calculations. The output of DIT+GEMINI simulations were used as a first order approximation of the reaction dynamics and fed into RAYTRACE. This allowed for the general simulation of the particle through the triplet and gave a rough estimate of the acceptance of the spectrometer. However, events from CoMD, used for physics calculations, were used to explore the theoretical response of the triplet to events from a range of interactions. Several variations of the results from CoMD were used. Specifically, elastically scattered beam particles (impact parameters 10-15 fm) were used directly, as were the results from CoMD filtered to select on PLFs from a ternary breaking of the reaction system. In order to preserve the dynamical physics on long time scales, the simulations were calculated

out to t = 3000fm/c. The purpose of this study was to approximate the effect of the magnetic fields on elastically scattered beam particles vs. the particles of interest. This is important as the cross-section for elastically scattered beam particles far exceeds the particles of interest and magnetically tuning the spectrometer provides a means of defocusing the unwanted beam-like particles while maximizing the transmission of the particles of interest.

Additionally, a large subset of the CoMD simulation results ($\sim 5 \cdot 10^5$ events), also on long time scales, were cooled with GEMINI prior to analysis via RAYTRACE to give a background of a larger range of possible reaction products expected to be successfully transported through the spectrometer. The data fed into RAYTRACE from CoMD was filtered to represent the maximum angle of transmission through FAUST into the spectrometer ($\theta \leq 2.3^\circ$) and took into account considerations such as focal plane size (5 cm x 5 cm Si detector at the end of the spectrometer) and annulus dimension of the beam pipe/quadrupole magnets. Further analysis of transport efficiencies is detailed in Section 4.

The flight path through the spectrometer can be visualized using the COSY-Infinity optics package[107]. In this way, it is possible to get a feel for the flight path, acceptance issues, and higher-order optical effects based on particle Bρ and angle of emission off the beam axis in degrees. In Figure 3.11, it is possible to visualize the flight path of particles through FAUST-QTS for PLFs from the ^{136}Xe+^{64}Ni reaction system at three, discrete angles (in θ) with respect to the entrance of the triplet. Specifically, the dispersion in the XZ- and YZ- coordinate planes can be visualized in Figure 3.11a and Figure 3.11b respectively. In this instance, PLFs from ternary breaking of the reaction system emitted at θ = 1.0° - 1.7° are visualized with only first order optical aberrations taken into account. The different line colors represent discrete theta angles (purple = 1.7°, red = 1.5°, blue = 1.0°) at a constant magnetic

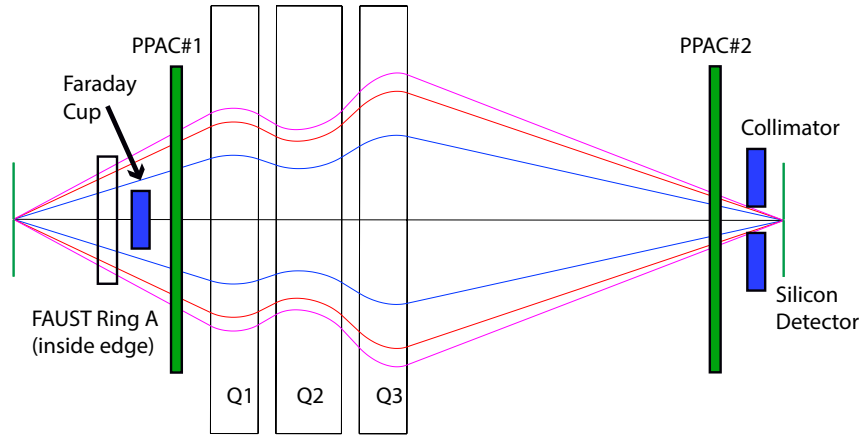

(a) XZ-optics coordinate plane

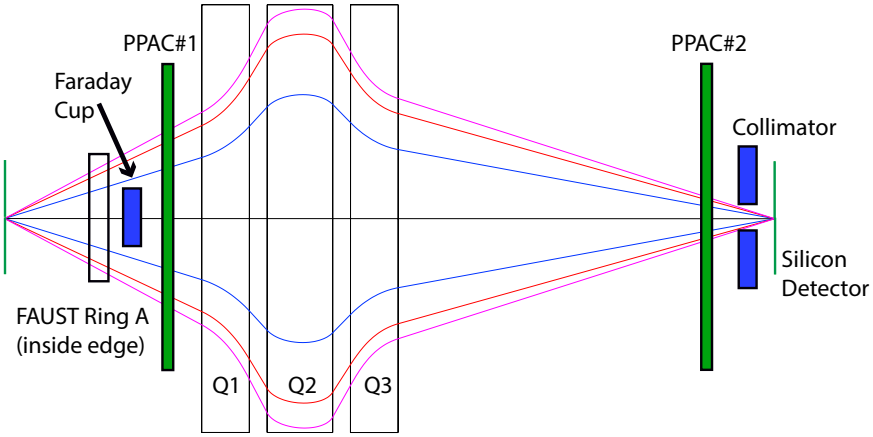

(b) YZ-optics coodrinate plane

Figure 3.11: COSY-Infinity simulations showing the flight path of ^{136}Xe at 15 MeV/nucleon at a three, discrete theta angles (purple = 1.7°, red = 1.5°, blue = 1.0°) at a constant magnetic rigidity (Bρ = 1.45T m). The optics calculations take into account 1st order effects only and are for demonstration purposes.

rigidity (Bρ = 1.45T m). Elastic beam like particles would be at higher rigidities, as expected. It should be noted that in Figure 3.11, the X- and Y-axis are to scale while the Z-axis is at some reduced scale to allow a reasonable visualization of focusing effects within a given optics plane through FAUST-QTS.

Visualization of higher-order magnetic field effects on the ion optics were also possible within COSY-Infinity. Higher order optical effects ($>1^{st}$ order) have a significant effect on the re-focusing of the ion image at the focal plane. This is important in attempting to more precisely approximate the magnetic settings that would be required to transport the particles of interest by approximating the most probable starting point for tuning the spectrometer and understanding how the magnets function cohesively as a set. This was an important factor to consider when empirically fine-tuning the spectrometer during the initial phase of data collection in order to more efficiently and analytically tune the spectrometer for maximized efficiency for the particles of interest. It was found that by under compensating the 3^{rd} quadrupole magnet (X focusing) by $\sim$5%, it was possible to compensate for higher-order optical effects. To this end, it was also found that effects beyond 3^{rd} order had little to no noticeable effect either visually or numerically within COSY-Infinity. These effects are discussed in greater detail in Section 4.

Schematic diagrams, previously described in Figures 3.8 & 3.11, detail the detector arrangement within FAUST-QTS. In this instance the collimator is shown at the end of the spectrometer just before the focal plane Si detector. This collimator was used in an attempt to minimize the number of elastically scattered beam particles incident upon the detector. Although the schematic diagram of the collimator hole appears to be symmetric, the collimator was designed such that only half (left/right) of the 2 cm diameter hole used in the experiment was allowed to transmit charged particles. The collimator allowed only two of the four quadrants of the focal plane detector to be exposed to charge particle transmission through the spectrometer. The reasoning for this is two-fold. First, the elastics in the experiment are not of great interest and come in at a rate that far exceeds that of the PLFs of interest. However, the elastics are still of use for calibration points. Second, the detector life

and resolution can be greatly extended if only a portion of the detector is exposed to higher energy elastics for a shorter amount of time. Since the focal plane detector was segmented into quadrants, the detector could be rotated 180° to expose two quadrants not previously exposed to charge particles. Overall, lower beam current incident upon the detector would likely have resulted in less damage.

3.2.4 Data Acquisition and Electronics

The electronics set-up for the FAUST-QTS allows for the conversion of analog signals from the silicon, PPAC, cesium iodide, and plastic scintillator to digital signals. These digital signals are collected by Versa Module Europa bus (VME) digital electronics modules and recorded to disk by the data acquisition software (DAQ). The electronics diagrams for the detectors and trigger logic are shown in Figures 3.12 through 3.16. In this experiment, acceptable events were triggered either by the FAUST or the QTS silicon detectors, both in singles mode. Table 3.6 details the abbreviations and short descriptions of the electronics modes used in this experiment.

Silicon detector electronics can be divided into four groups: full signal with timing (FAUST Rings A-D), attenuated signal (FAUST Rings B&C), full signal without timing (FAUST Ring E), and triplet silicon signals. All four groups are detailed, together, in Figures 3.13 and 3.14. The charge sensitive preamplifiers with fast timing output (CS-TPO) in FAUST rings A-D are mounted in custom preprinted circuit motherboards from RIS-Corp and housed inside custom designed boxes. The custom designed preamplifier housing boxes are designed to (1) act as a Faraday cage and to (2) mount directly to the front of the vacuum chamber that houses the FAUST array, in order to keep noise to a minimum.

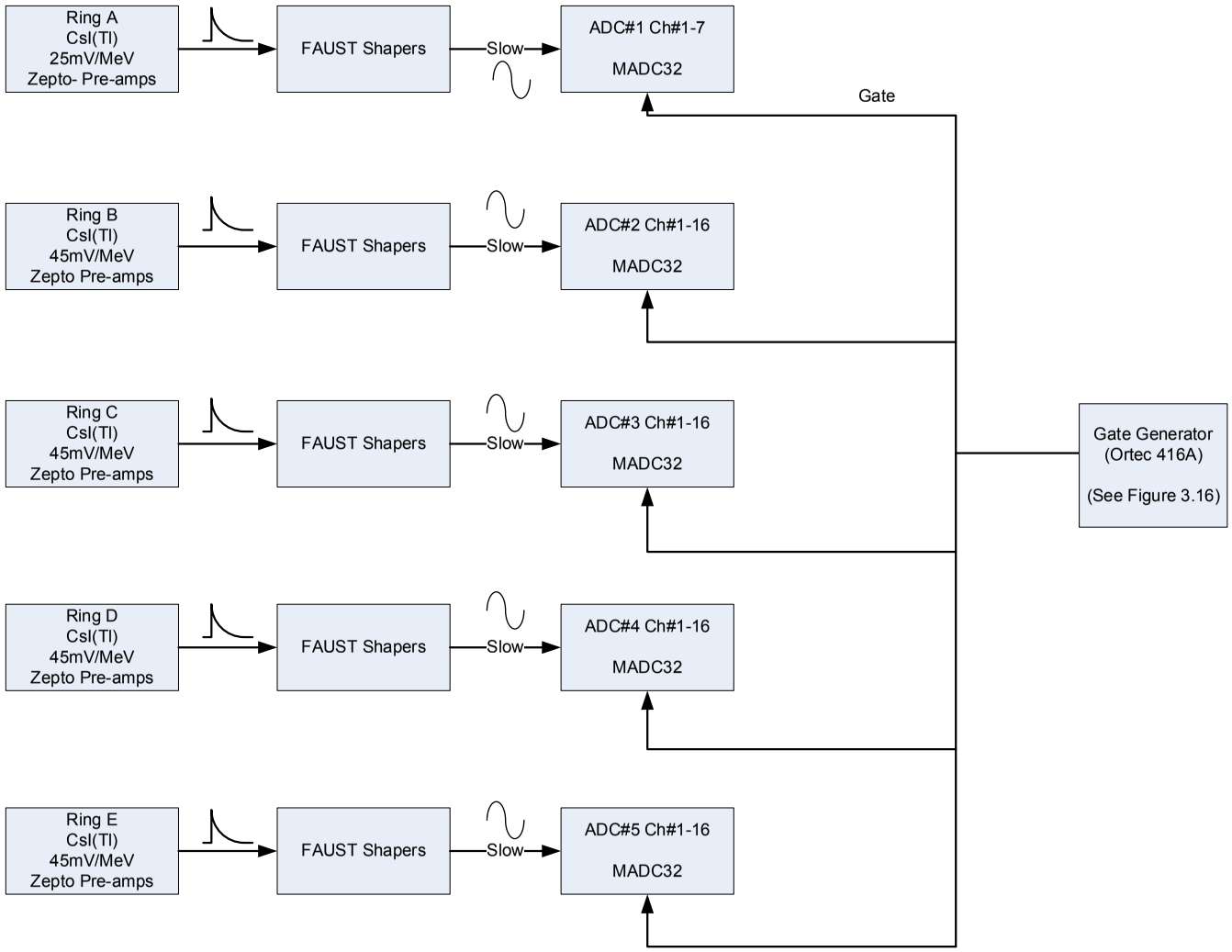

Figure 3.12: CsI Electronics Diagram for the experiment.

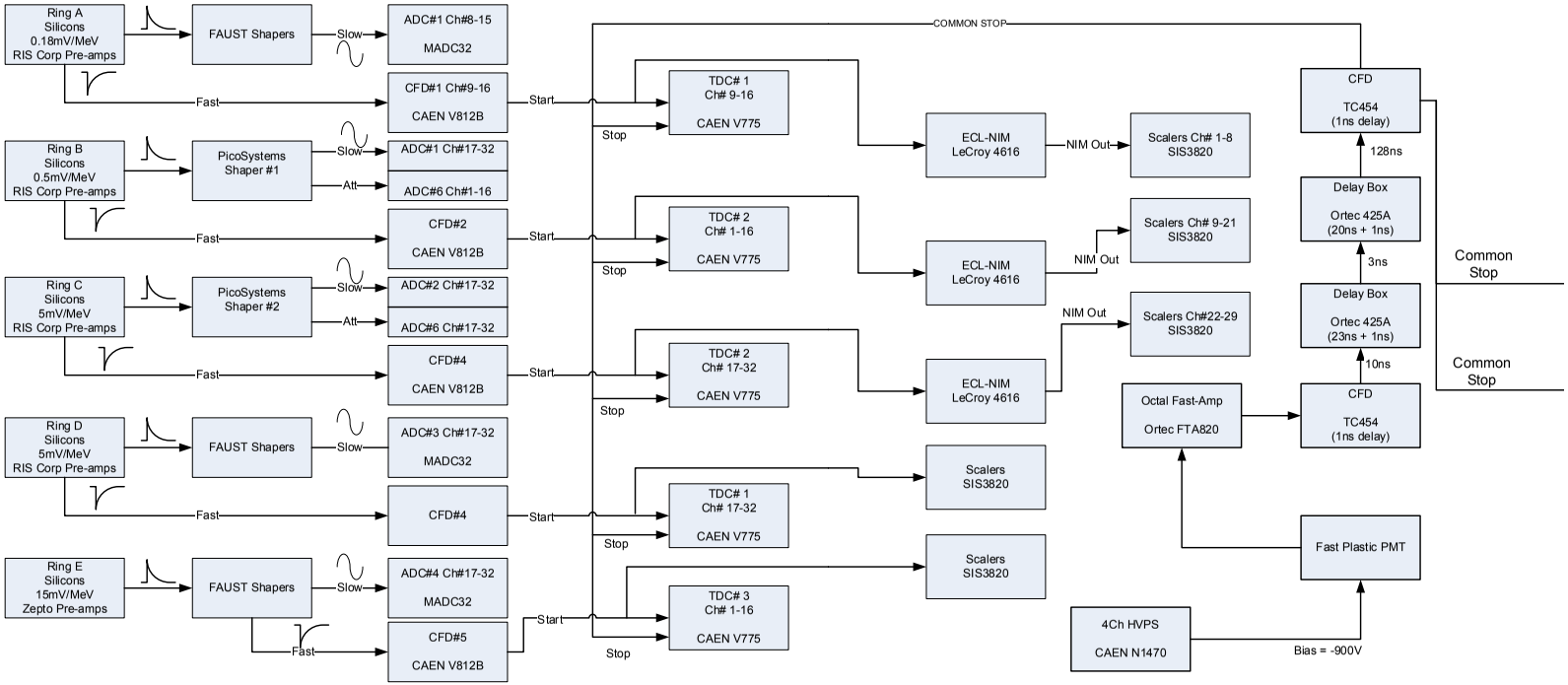

Figure 3.13: Timing Diagram for the experiment: Part 1.

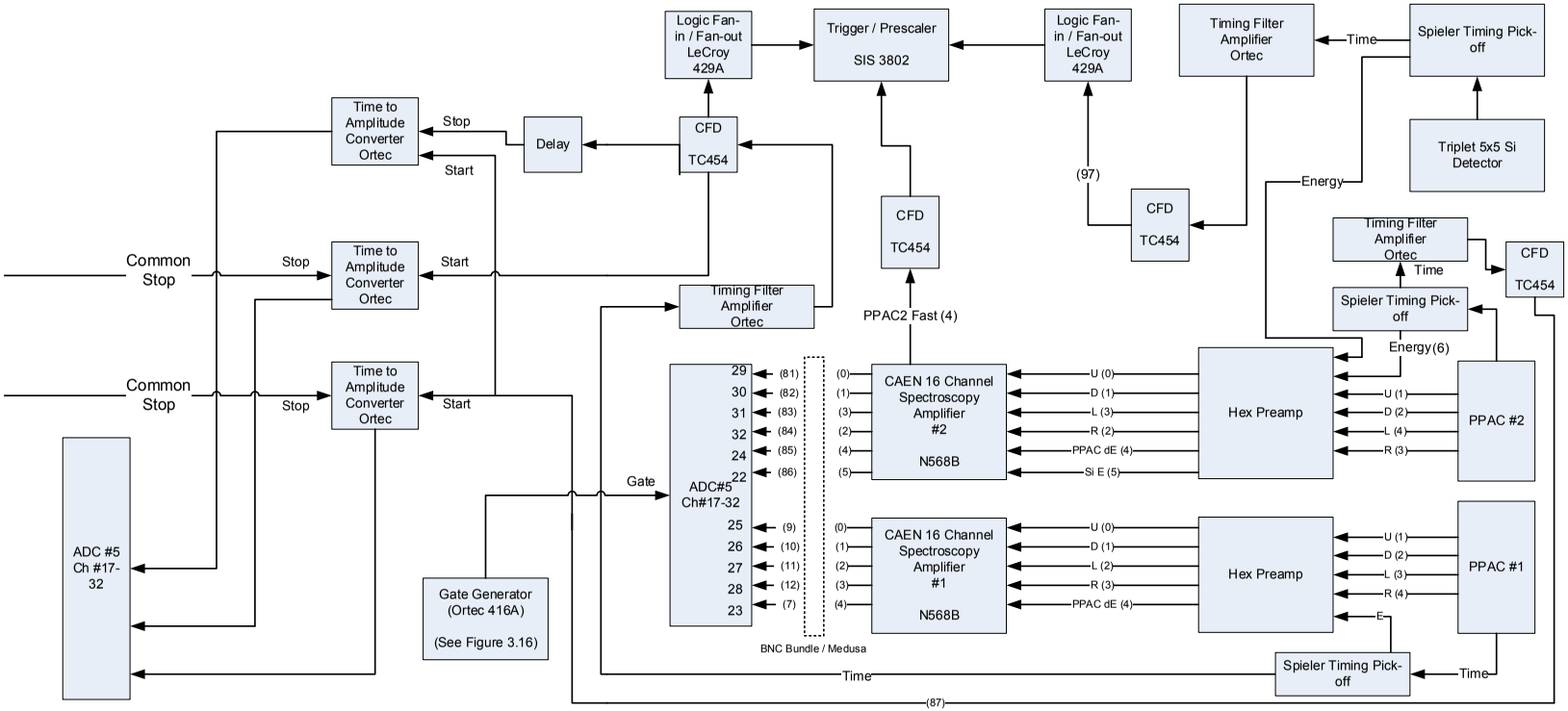

Figure 3.14: Timing Diagram for the experiment: Part 2.

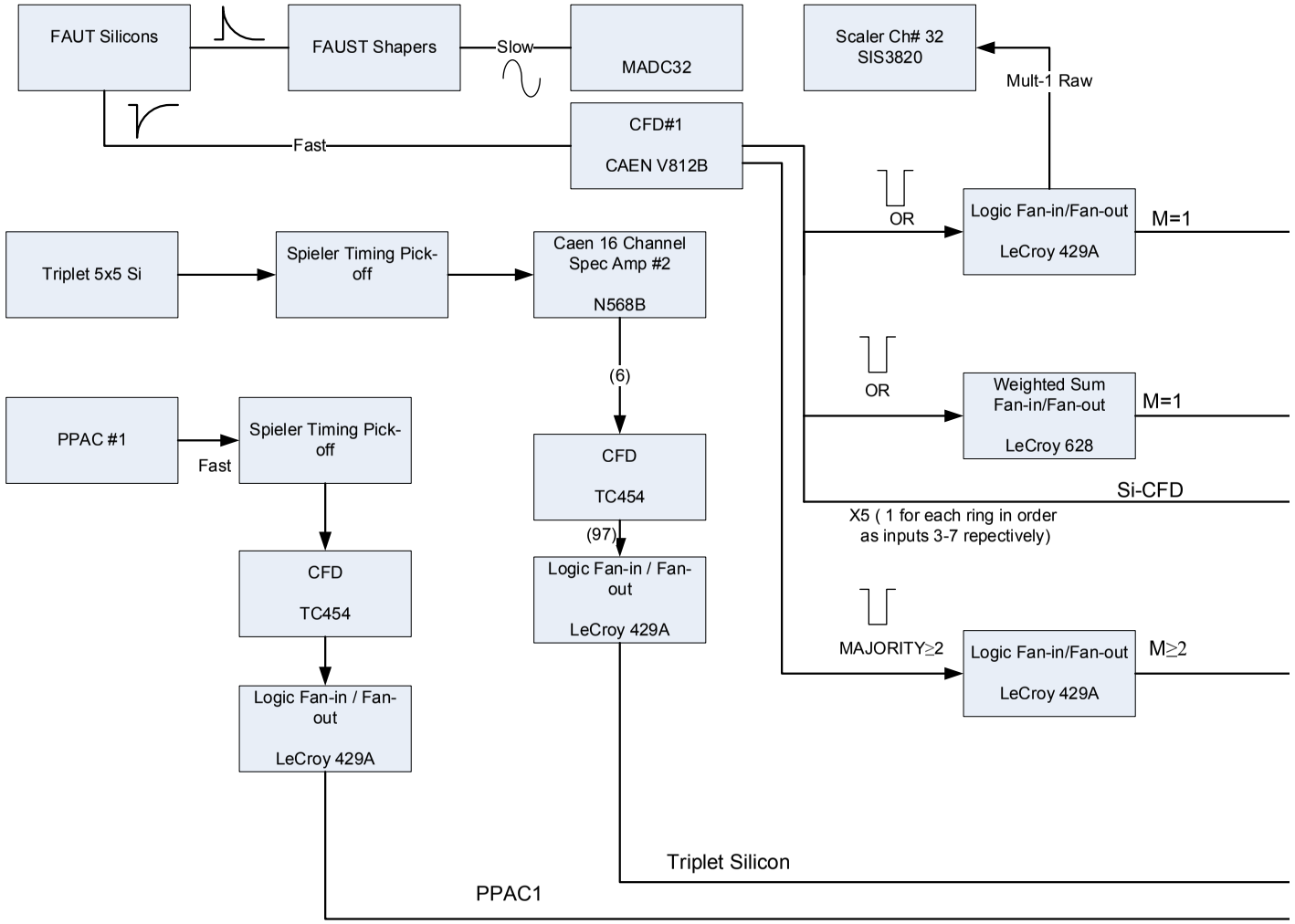

Figure 3.15: Trigger Logic Diagram for the experiment: Part 1.

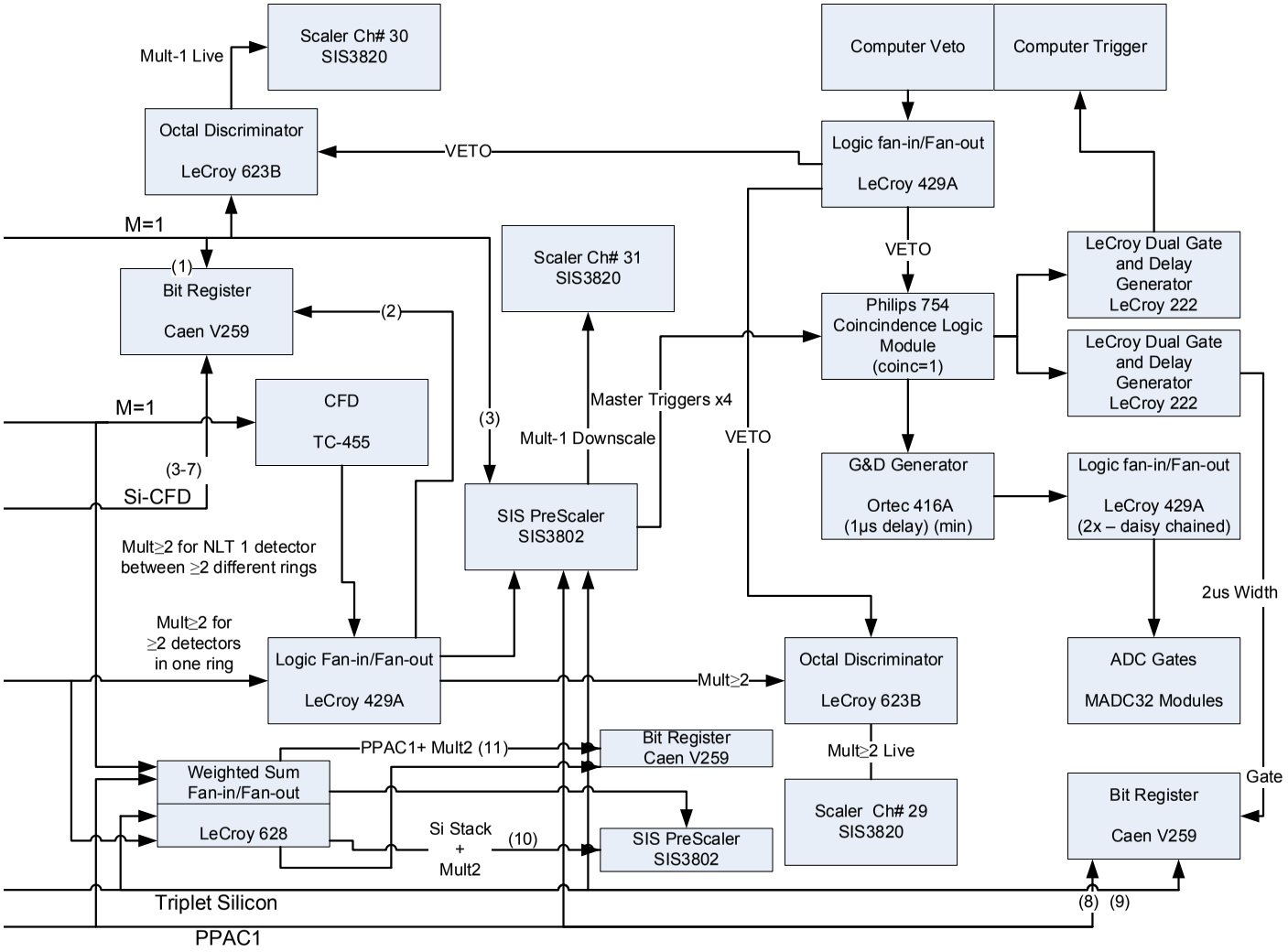

Figure 3.16: Trigger Logic Diagram for the experiment: Part 2.

Table 3.6: Short description, abbreviations and examples of the electronic modules used in the experiment. Additional information about the electronics modules can be found in Refs. [109, 110]

Module Name	Abv.	Function	Example Modules
Shaping Amplifier	-	Amplifies, integrates and differentiates the signal producing an uni- or bipolar signal	FAUST, PicoSystems, CAEN N568 Shapers
Timing Filter Amplifier	TFA	Amplifies, integrates and differentiates the signal producing a clean, unipolar, fast timing signal	ORTEC 474
Analog to Digital Converter	ADC	Converts analog peak height to digital signal	Mesytec MADC32
Constant Fraction Discriminator	CFD	Determines if the signal is above a set threshold based on a constant fraction of peak amplitude. Provides a consistent triggering time via NIM or ECL signal.	TC454, CAEN V812B
Leading Edge Discriminator	Octal	Determines if analog signal is above a set threshold	LeCroy 628B

Table 3.6 – Continued

Module Name	Abv.	Function	Example Modules
Charge Sensitive Preamplifier	Pre-amp	Integrates charge for the detector signal and provides a voltage output and initial amplification	Zepto Pre-amps, RIS-Corp Pre-amps
Timing Pick-off Preamplifier	TPO	Creates a fast (1 ns or less) unipolar output signal for accurate timing	Spieler Pick-offs, RIS-Corp Pre-amps
Logic Fan-in/Fan-out	Logic FI/FO	Creates a Logical OR signal if any input fired	LeCroy 429A
Gate Generator	-	Creates an adjustable width logic signal	LeCroy 222, GG8000, 8010
Scaler	-	Counts signals received	SIS3800
PreScaler	-	Sets Triggers and Downscale via remote connection	SIS3820

FAUST Ring E and the Triplet Si preamplifiers are of the Zepto systems style and are mounted in similar custom preamp housing boxes for the same reasons. All silicon detector preamplifiers are supplied with +/- 12 volts and bias voltage directly to the motherboards. Preamp supply voltage was supplied by Topward Dual-Channel DC Voltage power supply modules. Bias power supply for all of the FAUST silicon detectors was provided via WIENER Plein and Baus MPOD High Voltage power supply modules. These modules are remotely controlled via microprocessor and provided, on average, between 35-45V of bias voltage to each detector individually. The triplet silicon detector was supplied bias voltage by a Tennelec High Voltage Supply module.

The first two cases of silicon detectors electronics, full signal with fast timing (FAUST Rings A-D) and attenuated signals (FAUST Rings B & C), are best described together as they utilize the same preamplifiers from RIS-Corp. After the preamplifiication stage, as described in Section 3.2.2, the gain and the shape of the silicon energy signal was adjusted by the shaping amplifier. The signals, from Rings A and D, are processed in custom FAUST timing/shaping amplifiers with a bipolar shaping time of 0.5μs. The preamplifier energy signal from Rings B & C were processed by CAMAC Pico Systems shaping amplifiers[111]. A full energy signal and an attenuated signal (attenuated to 1/2 of the full energy signal) were cabled from the Pico Systems shaping amplifiers. This was done to get good resolution on lower energy particles on the full energy signal and detect a larger number of the higher mass particles that implanted in the silicon on the attenuated signal. These higher mass particles imparted a higher energy into the silicon detectors and required a higher range energy scale. Only the slow energy signal was used from the shaping amplifiers as the timing signal comes directly from the RIS-Corp preamplifiers. The slow, shaped amplifier signal was then read out by Mesytec MADC32 peak sensing, VME

analog-to-digital converters (ADCs). Timing signals from the RIS-Corp preamplifiers were processed by CAEN V812B constant fraction discriminators (CFDs) set with 12ns delay by onboard dip-switch, piggy-back chip combination. The ECL timing signal from the CFDs was then read out by CAEN V775 TDCs set to maximum resolution (35 ps/channel, 143 ns full range) and a SIS3800 VME scaler module. In the case of Ring D, the ECL signals from the CFDs were converted to a NIM signal via a Lecroy 4616 ECL-NIM converter and then passed to a NIM version of the SIS3800 scaler module.

The energy signals from Ring E were pre-amplified via the Zepto systems preamplifiers and then shaped/amplified by the FAUST timing amplifiers. The slow signal was processed in the same fashion as Rings A-D. The fast timing signals out of the FAUST timing amplifiers were processed by CAEN V812B constant fraction discriminators (CFDs) set with 12ns delay by onboard dip-switch, piggy-back chip combination. The ECL timing signal was then read out, directly, by a CAEN V775 TDCs set to maximum resolution (35 ps/channel, 143 ns full range) and a SIS3800 VME scaler module after being converted to a NIM signal via a Lecroy 4616 ECL-NIM converter module. The timing start signal was generated by each silicon detector in the FAUST array. The common stop comes from the fast plastic scintillator upstream of the FAUST array. It is delayed by 135 ns before being fed to the CAEN V775 TDCs, as described in Section 3.2.2.

The energy signals from the QTS silicon detector were first passively split. The split occurred on the input of a Spieler Timing Pick-off amplifier (LBL-21X7422), where one half of the passively split signal was sent to a Zepto systems charge sensitive preamplifier in similar fashion to the FAUST silicon signals. The other half of the signal from the Spieler pick-off was used to generate a fast timing signal. This resultant fast timing signal was then preprocessed by an ORTEC 474 Timing Filter

Amplifier. The clean, preprocessed signal was then discriminated by a Tennelec 454 CFD with 1ns of delay. This timing signal was then used in the trigger logic.

The triggering, as schematically shown in Figures 3.15 and 3.16, relied solely on the signals from the silicon detectors in this experiment. The trigger signals from the FAUST silicons were generated by the CAEN V812B CFDs on the OR output. This OR was then split via LeCroy 429A logic fan-in/fan-out modules for each CFD OR signal. The output of these fan-in/fan-out modules was then sent to a LeCroy 628 weighted sum fan-in/fan-out to generate a weighted sum of all the FAUST silicon triggers. The output signal from the LeCroy 628 was used to create the FAUST singles trigger, a global singles trigger between the QTS and FAUST detectors, and as in input to the high multiplicity trigger discussed immediately below.

Additionally, the "majority output" of the CAEN CFDs were utilized to trigger on multiple hits within the same ring of FAUST as an input to the FAUST high multiplicity trigger. Other trigger logic paths were connected (as shown) for diagnostics purposes, such as to trigger on PPAC coincidences or singles, but these were not used for taking physics data. Each of the trigger signals was sent to a SIS3800 pre-scaler module input where each trigger was enabled and downscaled remotely. The output from the SIS3800 prescaler was then sent to a scaler to count the event rate for each trigger was, as well as to a Philips 754 coincidence module set to coincidence = 1. From the coincidence module, the signal was sent to either a LeCroy 222 or ORTEC 416A gate generator. From these gate generators, the computer trigger and 2 μs ADC gates were generated. A computer busy signal (VETO) was generated and sent to the coincidence module by the VM-USB computer after it received the computer trigger. The VETO was used to inhibit the generation of additional gates until the computer was done acquiring data. Typical live time during the experiment was between 95% to 97% live.

The electronics pathway for the cesium iodide signals is far simpler and reminiscent of the FAUST silicon signals. The photodiodes collect the photons generated from the incident particle's interaction with the cesium iodide crystal. These photons are detected by photodiodes mounted to lucite light guides glued (with optical cement) to the back of the cesium iodide crystal. The signal from the photodiode was pre-amplified via Zepto systems charge sensitive preamplifiers. Preamplifier gains are as tabulated in Table 3.7. These gains were chosen based on the expected particle-of-interest energy loss as predicted by CoMD simulations. In particular, Rings A & B were gained to detect PLFs where as Rings C - E were gained to detect IMF and LCPs at a range energies. The preamplifier signal was shaped by the FAUST timing amplifiers (0.5μs shaping time) with the slow, bipolar, shaped signal recorded by Mesytec MADC32 peak sensing ADCs.

Table 3.7: Preamplifier gains for FAUST

Detector Gain	Silicon	CsI(Tl)
Ring A	0.18 mV/MeV	25.0 mV/MeV
Ring B	0.5 mV/MeV	45.0 mV/MeV
Ring C	5.0 mV/MeV	45.0 mV/MeV
Ring D	5.0 mV/MeV	45.0 mV/MeV
Ring E	15.0 mV/MeV	45.0 mV/MeV

Time of flight and position information for particles that escaped through the center of FAUST and entered the QTS were also recorded (digitized). The signals were generated by Parallel Plate Avalanche Counter detectors (PPACs). The PPACs were mounted one in front of the triplet and one after the triplet spectrometer but before the silicon detector. In this way, position sensitive information was made

available before the rays were transported through the triplet, as was the flight time difference between the two PPACs. Each PPAC, with 6 torr of isobutane gas flowing at 30-40 cm^3/second, was biased with 530V of bias from a Tennelec High Voltage Power Supply. The signals from the up (U), down (D), left (L) and right (R) signal were pre-amplified by custom designed hex-amplifiers. The U, D, L and R signals were then shaped by a CAEN N568B, 16-channel Spectroscopy amplifier.The resultant amplified signals were then digitized via Mesytec MADC32 peak sensing ADCs. The timing signal from the PPAC was passively split via Spieler Timing Pick-off amplifier, with half of the signal being pre-amplified, shaped and digitized like the U, D, L and R signals. The other half of the passively split signal had background noise reduced and the timing signal amplified by an ORTEC timing filter amplifier and discriminated by a Tennelec 454 CFD. The signals from both PPACs were treated in the exact same way. The timing signals resulting from both PPACS were then taken from the CFDs and measured via and ORTEC 566 time-to-amplitude converter with PPAC#2 being the start and PPAC#1 being the stop (effectively in common stop mode).

3.3 Particle Identification

In the current configuration of FAUST and its associated electronics, there are two types of particle identification (PID) possible, Si vs. CsI(Tl) ΔE-E PID of energetic LCPs/ IMFs that punch through the Si and Energy-ToF mass measurement of less energetic IMFs/PLFs that are not energetic enough to punch through the silicon. Particles identifiable via ΔE-E were isotopically or elementally identified first. These particles were then used for the energy calibration of the detectors. Once the PID and energy calibration were complete for these particles, the particles identifiable via Energy-ToF were then identified using the energy calibration from ΔE-E and

calibrated timing spectra. Particle identification will be described in this order as it is the logical chain of events used for this experiment.

3.3.1 Silicon vs. CsI (SiCsI) Particle Identification

This particle identification technique is versatile enough to get isotopic identification of charged particles from Z = 1 to Z = 10 and elemental identification for large Z-value particles up to the beam. For this experiment, it was rare to have IMFs identified with a Z>16 in Si-CsI(Tl) ΔE-E. The energy lost by a charged particle through a material (such as silicon in this particular instance) as a function of distance (dE/dx) can be described by the relationship

$$-\frac{dE}{dx} \propto \frac{Z^2}{\nu^2} \propto \frac{Z^2 \cdot A}{KE} \tag{3.1}$$

where KE is the kinetic energy of the incident particle with charge = Z and mass = A. This is a reduced form of the *Bethe-Bloch formula* (Eq. 3.2):

$$-\frac{dE}{dx} = \frac{4\pi}{m_e c^2} \cdot \frac{nz^2}{\beta^2} \cdot \left(\frac{e^2}{4\pi\varepsilon_0}\right)^2 \cdot \left[ln\left(\frac{2m_e c^2\beta^2}{I \cdot (1-\beta^2}\right) \cdot \beta^2\right] \tag{3.2}$$

where c is the speed of light, ε_0 is the vacuum permittivity, n is the electron density of the stopping material, $\beta = v/c$, and e and m_e are the electron charge and mass respectively.

The PID procedure is accomplished using a linearization method[112] to linearize the 2-D plots of Si-CsI(Tl) ΔE vs E. This linearization of the 2-D plots allows for their projection onto a 1-D axis with each linearized ΔE-E trace forming, what could be likened to a mass-spectrum generated in traditional chemical mass-spectrometry. These 1-D projections are then fit with gaussian functions for each isotope providing a quantitative method of isotopic (or elemental) particle identification. Much of this

procedure was adopted directly from the NIMROD-ISiS[87, 113] data analysis software and adjusted for use with the FAUST array as there are a number of similarities between the detector arrays. In an effort to reduce the amount of redundant effort put into software development for PID and calibration for experiments performed in the future, the two detector array PID and calibration software have been made more similar. This was accomplished by retrofitting the existing NIMROD-ISiS software to the FAUST event structure. Also of note, a great deal of effort has previously gone into making the PID and calibration of NIMROD-ISiS more user friendly through a large number of graphical user interfaces (GUIs). These have been incorporated into the FAUST-QTS software as well.

3.3.2 Linearization

The first step in the linearization method is to hand pick lines for the most prominent isotope for each element. This is accomplished by picking ∼20-40 points following the curvature represented in the 2-D spectra for each detector (Figure 3.17). A spline fit between each of these points is generated using 100 points per spline according to the method described by May et. al[112]. Using the spline fit points, the data was then linearized into 2-D linearized spectra and 1-D mass spectra shown in Figure 3.18. The linearization algorithm calculates the relative distance between two closest fit lines for each experimental data point. An arbitrary value, LinZ, is then assinged to the data point. For a simple example, the value of LinZ of a point located equidistant to the fit line for Z = 5 and Z = 6 would be given a LinZ = 5.5. More analytically, the value of LinZ is determined by the Equations 3.3 - 3.5 where $\text{Line}_1(\text{Line}_2)$ is the Z line and $\text{Dist}_1(\text{Dist}_2)$ is the distance from the point to the respective line. In this way, Equation 3.3 is used when the data points are to the left of Line_1, Equation 3.4 when the data points are between the two lines, and

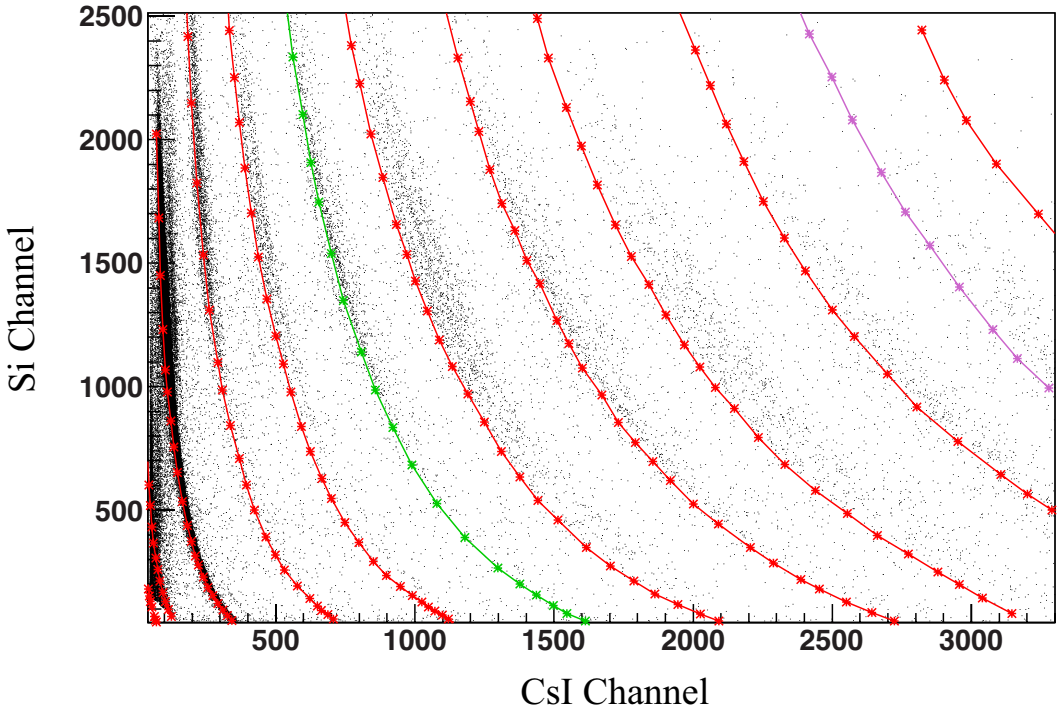

Figure 3.17: 2D Si-CsI ΔE-E spectra with picked points overlaid.

Equation 3.5 when the data points are to the right of Line_2.

$$LinZ = \frac{Dist_2}{|Dist_2 - Dist_1|} Line_1 - \frac{Dist_1}{|Dist_2 - Dist_1|} Line_2 \tag{3.3}$$

$$LinZ = \frac{Dist_1}{|Dist_1 + Dist_2|} Line_2 + \frac{Dist_2}{|Dist_1 + Dist_2|} Line_1 \tag{3.4}$$

$$LinZ = \frac{Dist_1}{|Dist_1 - Dist_2|} Line_2 - \frac{Dist_2}{|Dist_1 - Dist_2|} Line_1 \tag{3.5}$$

The distance to each line was calculated by first splitting the 100 point, splined line into 99 individual line segments. The distance from the data point to each line segment was then calculated. The minimum distance determined in this way was then used in Equations 3.3 - 3.5. A linearized version of the original 2-D ΔE-E plot

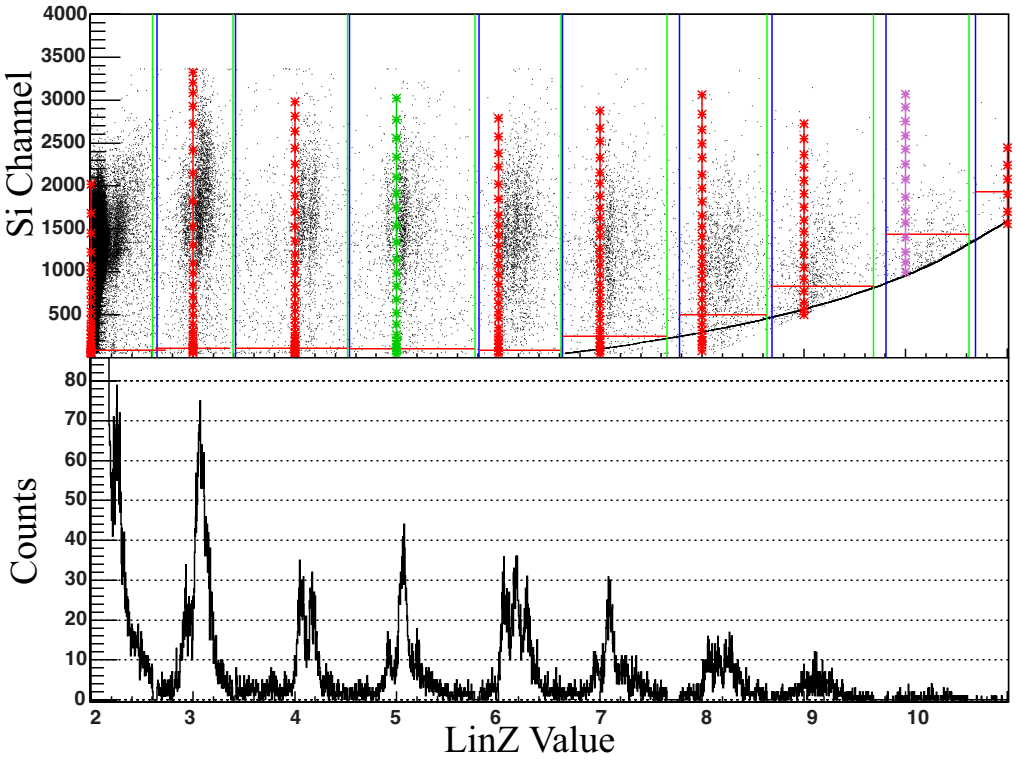

Figure 3.18: Linearized ΔE-E spectra (top) and mass spectra (bottom) zoomed on Z = 2 - 10. The upper panel shows the linearized version of Figure 3.17. The right/left limits shown in blue/green represent the upper and lower mass limits for a given element. The lower red line represents the lower energy threshold for a given element. An upper software limit can be set, if needed. Normally the upper limit is a function of the detector gain. The lower panel shows the x-projection of the linearized ΔE-E spectra detailing the isotopic resolution.

was then generated. The linearized 2-D histogram is plotted with the original Y-axis value versus the linearization value (LinZ) determined from Equations 3.3 - 3.5 for the experimental data points. This process is repeated until the linearized 2-D histogram contains nominally linear, well separated lines for the given isotope or element depending on the energy resolution of the respective Si-Csi(Tl) telescope.

The left and right as well as upper and lower limits are placed on each isotope (Z = 1-2) or element (Z≥3). This method allows for a clear Z (or isotopic) band as

well as removing any noise from each linearized band of data. Based on where the four limits are set determines the resolution of isotopes in the respective 1-D mass spectra, which will be subsequently used for Gaussian function fitting (Section 3.3.3).

3.3.3 Gaussian Fitting for PID

The 1-D, linearized mass spectra of the experimental data produced in the previous section (Section 3.3.2) was fit with Gaussian functions in order to define the Z and A of each peak (Figure 3.19). Each peak is representative of one isotope of a

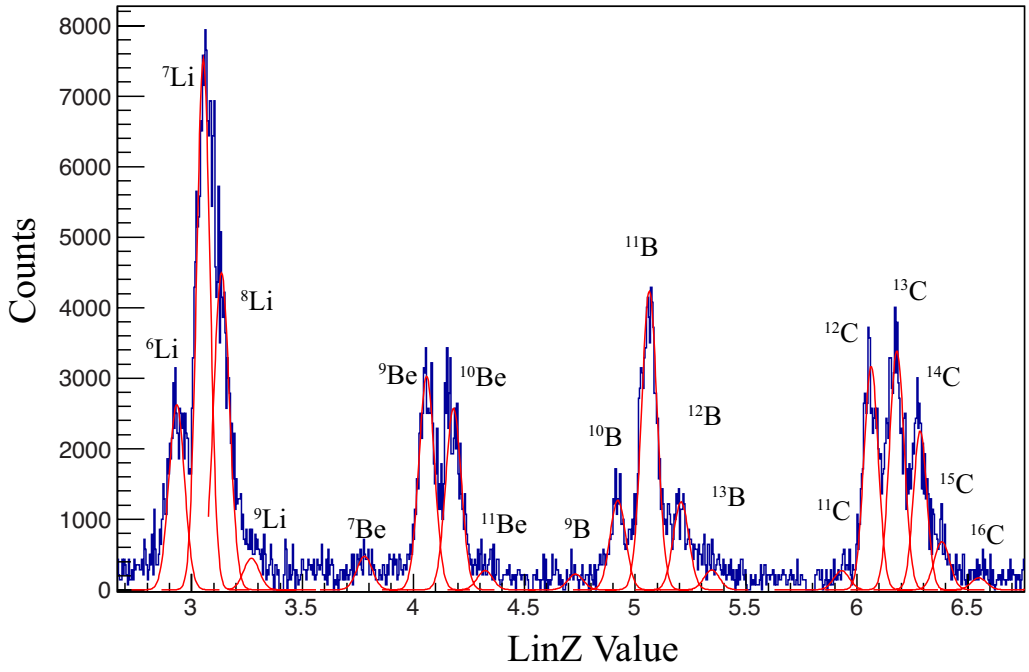

Figure 3.19: 1D Projections of the Si-CsI linearization showing the Gaussian fits for the Z = 3-6 isotopes.

given element (Z). The Gaussian functions used for fitting the 1-D spectra were of

the form

$$G(x) = C \cdot e^{-0.5 \cdot \left(\frac{x-\mu}{\sigma}\right)^2} \tag{3.6}$$

where C is the height parameter (amplitude), μ is the mean, and σ is the standard deviation (or width) of the Gaussian fit for a given peak. The parameters for each individual Gaussian fit were determined by minimizing the error between the sum of the Gaussians and the experimental data spectra for a given Z-value through a graphical user interface (GUI). The A (mass) of each Gaussian was manually assigned either via natural abundances (Z = 1-2) or by comparing to experimental yields for similar reaction systems from experimental data from MARS[114] and NIMROD-ISiS[87]. In the case where isotopic identification was not possible, a single broad Gaussian function was fit over the entire elemental (Z) band. This process was carried out for both the full energy Si-CsI(Tl) spectra as well as the attenuated Si-CsI(Tl) spectra. In this way it is possible to have a particle identified in both. In the case that these PIDs are not the same, the logic for determining which was the assumed PID is described in Section 3.3.4.

3.3.4 Finalizing PID

The final step in the Si-CsI(Tl) particle identification process is to check the particle identification as it is possible to get PID in both the full and attenuated spectra for the Si-CsI telescopes. Because of the way the Gaussian fits are calculated, it is allowable for one to adjust the cuts on the 1-D mass spectra based on standard deviation (pSigma) and the percent contamination of one isotope into another (%Contam) for each Gaussian fit. The percent contamination is defined by

$$\%Contam = \frac{\left(\sum_{i=0}^{N_{gauss}} G_i(LinZ)\right) - G_{max}(LinZ)}{G_{max}(LinZ)} \tag{3.7}$$

where N_{Gauss} is the number of Gaussian functions for a given element, G_i(LinZ) representing the i^{th} Gaussian at point LinZ, and G_{max}(LinZ) representing the highest amplitude G_i(LinZ) for a given element. The Z and A are determined for each particle by the G_i(LinZ) that returned the value for G_{max}(LinZ).

The location of the particle with respect to its standard deviation from the mean of the Gaussian fit (pSigma) was determined by the function

$$pSigma = \frac{|LinZ - \mu|}{\sigma} \tag{3.8}$$

where μ and σ are the mean and width parameters of the Gaussian fit function as determined from Equation 3.6 in Section 3.3.3.

The first cut placed on the experimental data was to only accept particles with a pSigma$\leq$3.0. This removes particles near the edge of the elemental distribution that have less than a 1% confidence interval of being a particle of interest and not noise. Additionally a %Contam = 100% was set (akin to vertical lines in the valley of the gaussian distributions between each isotope for a given Z) to allow allow a maximum number of particles through to the physics tape analysis. Additionally, due to saturation issues at the high end of the energy band of the attenuated silicon energy signal, the E-ToF attenuated signals were rejected. Consequently, the particles identified in the attenuated E-ToF that were not identified in the region of saturation were available in the full E-ToF spectra.

Since a particle can receive multiple Z and A identifications (though ΔE-E and/or E-ToF), we use a tagging system to label the sources of Z and A identification and then later select the source with the best resolution, and highest confidence, to finalize the identification and write the particle to "Physics Tapes" (described in Section 3.6). Particles can be identified by full and attenuated ΔE-E, as well as full

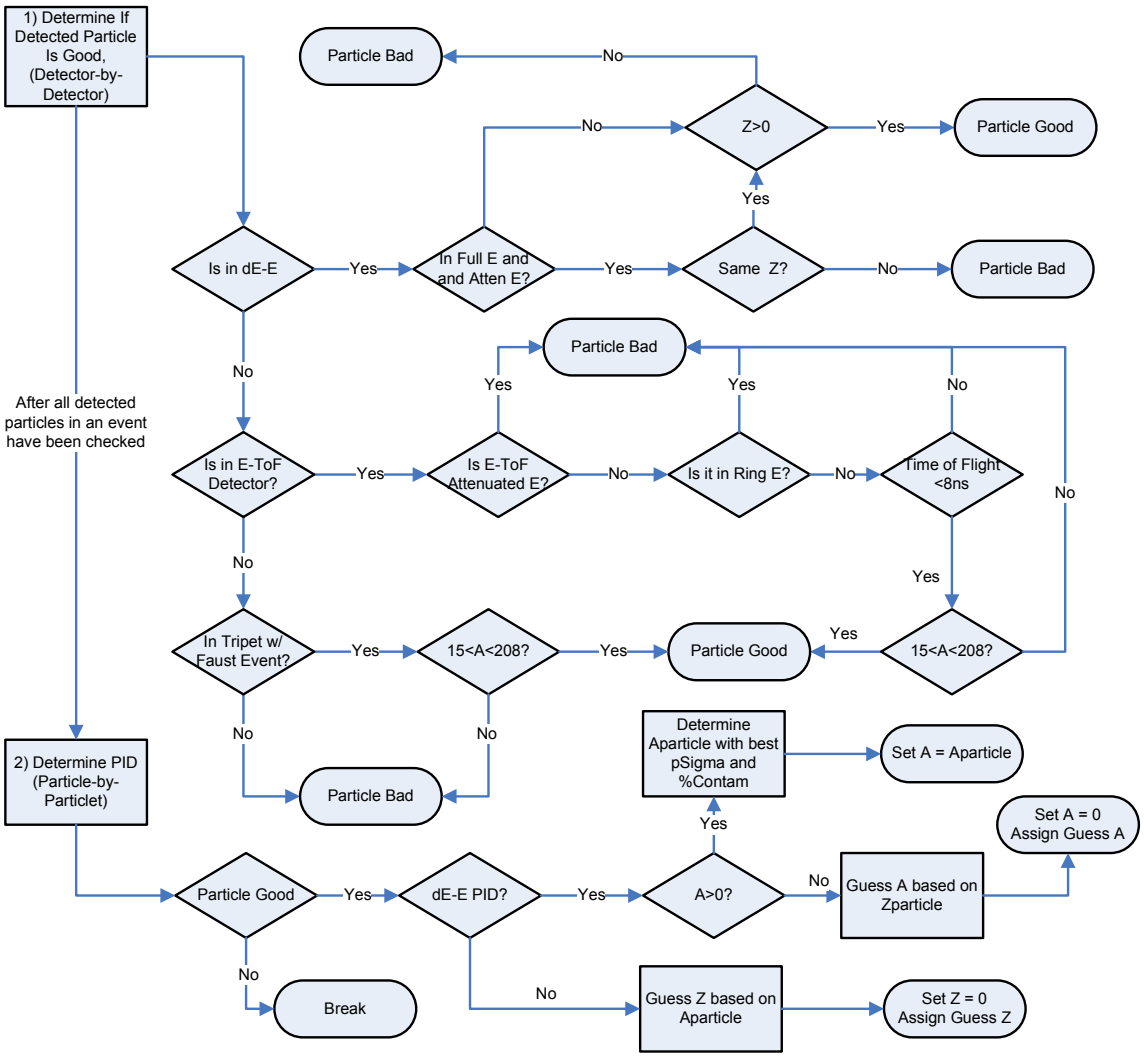

Figure 3.20: Flow chart depicting the process for checking and comparing the particle identifications in different detector types within the FAUST-QTS analysis software.

and attenuated E-ToF. Particles detected in the attenuated E-ToF were rejected and marked as bad. Particle identification logical hierarchy is described in the flow chart depicted in Figure 3.20.

The full Si-CsI(Tl) ΔE-E was first checked for particle identification followed by the attenuated ΔE-E. If the particle was fully identified in both the full and attenu-

ated ΔE-E, and the A matched between the two, the signal from the full ΔE-E was accepted. If either one had isotopic identification but not the other, the one with isotopic identification was accepted. Otherwise, if neither had isotopic identification, but rather only elemental (Z) identification and the Z matched between the attenuated and full signals, the particle signal with the lowest pSigma and %Contam was accepted. Subsequently the E-ToF detector channels were checked for particles. The E-ToF particles must first have their energy and time calibrated (Sections 3.4 and 3.5 respectively). Once the particle has a calibrated energy and time signal, the particle can be mass identified using a series of equations (Eqs. 3.9 - 3.11).

$$\beta = \frac{L}{t \cdot c} \tag{3.9}$$

$$\gamma = \frac{1}{\sqrt{1-\beta^2}} \tag{3.10}$$

$$A_{\text{E-ToF}} = \frac{E_{frag}}{(\gamma - 1) \cdot 931.5} \tag{3.11}$$

Equation 3.9 describes the velocity (v/c) as a function of flight path length (L), time (t) and speed of light (c). This velocity is then used to calculate the Lorentz factor in Eq. 3.10. From there, the mass of the fragment ($A_{\text{E-ToF}}$) is described in Eq. 3.11 as a function of the Lorentz factor (γ) and the energy of the fragment (E_{frag}). Particles in the full E-ToF were checked to ensure the particle was not detected in ring E as there were no fast timing signals in those detectors. The particle was then checked to ensure time of flight to the detector was real ($t \leq 8\ ns$) and that the mass of the E-ToF particle was within the detectable range ($15 \leq A \leq 208$). Finally, particles detected in the triplet Si detector by Si energy vs. PPAC-to-PPAC timing in coincidence with a signal from FAUST, the mass was identified via a procedure similar to that described in Eqs. 3.9 - 3.11.

3.4 Energy Calibration

The energy of the particles detected in FAUST-QTS during the experiment along with calibrations beams (Table 3.2) scattered at pre-determined energies and source data (^{228}Th and ^{252}Cf) were used to create energy calibration points. The code LISE++[115, 116] was used to calculate the scattering energy of each particle with respect to the average angle it was detected at for the relevant detector. In the case of the triplet spectrometer, the projectile elastics and a "picket-fence" style pulser calibration were used in order to span the entirety of the energy spectra in the triplet detectors. This was necessary as the magnetic fields of the triplet spectrometer were not strong enough to focus the lighter calibration beams used in the calibration of FAUST.

3.4.1 Faust Energy Calibration

For the FAUST array, the punch-in energy of lighter incident particles and calibration beams were used to calibrate FAUST. The punch-in points are defined as the point on the 2D Si-CsI plot that represents the energy at which a given isotope can pass through the silicon detector and deposit a detectable amount of energy in the CsI(Tl) crystal. Additionally, the energy implanted in the Si detector for the projectile elastics that were stopped in the Si detector of the Si-CsI(Tl) telescopes were used to double check the punch-in energy calibration. This can be visualized in Figure 3.21 where the red points on the 2D histogram represent the punch-in point for each isotope.

After picking the punch-in points, the energy required to punch through the 300 μm thick silicon detector (and just into the CsI) was calculated using energy loss tables tabulated in the SRIM database[117, 118] directly from the data analysis software. The calibration between the particle energy and silicon detector raw ADC

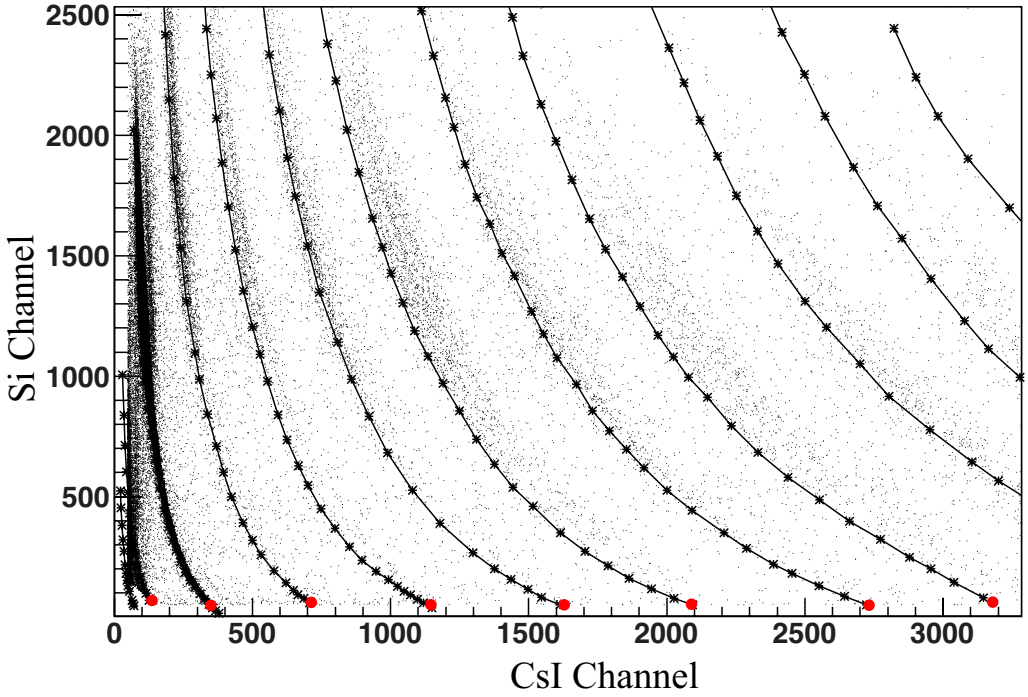

Figure 3.21: Punch-in points overlaid on top of a 2D Si-CsI ΔE-E Histogram.

channel number was assumed to have a linear relationship

$$E = SiChannel\# \cdot m + b \tag{3.12}$$

where m and b represent the slope and intercept of the calibration respectively. Figure 3.22 shows a typical silicon detector calibration where the blue circles represent the punch-in points determined from the raw, 2D Si-CsI histogram. The punch-in points were fit using Eq 3.12. The green squares represent the calibration points as detected from the calibration beams. The results of this calibration procedure show that the punch-in point calibration is in excellent agreement with the points from the calibration beams.

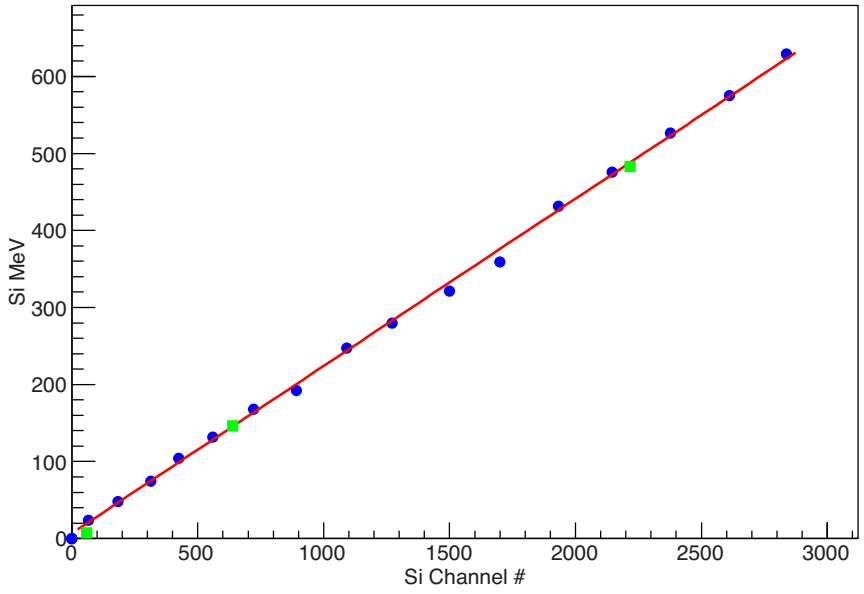

Figure 3.22: FAUST silicon energy calibration using punch-in points and calibration beams. The punch-in calibration points are in blue and the calibration beams are shown in green. The calibrations beam points accending from lowest energy to highest are ^{4}He(lower), ^{22}Ne(mid), and ^{40}Ar (upper). This plot represents a typical FAUST silicon detector.

It is possible to calibrate the CsI(Tl) detectors through a variety of methods including that of Tassan-Got[119] and Tabacaru[120] et al. relying on Birk's formula[109, 110] to obtain a calibration fit. In this experiment, energy loss calculations were used, event-by-event, to determine the energy lost in the CsI relative to the calibrated energy deposited in the silicon detector in this experiment. After completing the energy calibration for the silicon detectors, the total energy for each particle was determined. The total energy for all particles was calculated, event-by-event, by taking the calibrated energy loss in the silicon detector and using energy loss tables from SRIM[117, 118] based on the particle identification. The difference in the energy lost in the silicon detector vs. the total energy of the particle, as determined event-by-event using SRIM calculations, was then assigned as the CsI energy for that

detector.

3.4.2 Triplet Spectrometer Energy Calibration

Energy calibration for the particles detected in the silicon detector at the back of the triplet was completed in a similar fashion to that used for the FAUST array. The difference, however, is that there were no particles detected that punched through the silicon, as we had used a single 1000 μm silicon detector to stop the particles. In this way, we were able to use the experimental production beams' elastic scattering to obtain three calibration points at higher energies. For the lower energies, where elastic beam particle calibration was not possible, a picket-fence style pulser calibration was used where pulses were injected into the preamplifier via capacitive coupling. The digitized channel value of each input pulser setting was recorded via ADC and read-out by the data acquisition software. The pulser data was then calibrated by fitting with a linear function similar to Eq. 3.12. This function provided a mV to channel# calibration function. The elastically scattered particles were then calibrated with this function to determine their mV value based on the recoded ADC channel# populated by the detected particles. This mV value represents the mV value that would have been read on the oscilloscope if a pulser calibration had been used to generate these points. Since there is now common ground between between the pulser calibration and elastically scattered particle calibration via a mV to channel# relationship, it was then possible to convert the pulser mV calibration to MeV based on the known energy of the elastically scattered particles as determined by average scattering angle and energy loss through the QTS. This allowed for the calibration of the upper end of the energy spectra by the beam particles and the detector linearity to be determined by pulser calibration. The calibration in terms of MeV as a function of mV is shown in Figure 3.23a. The error of the calibration

fit (as visualized in Figure 3.23b) was found to be on the order or ±2.0%.

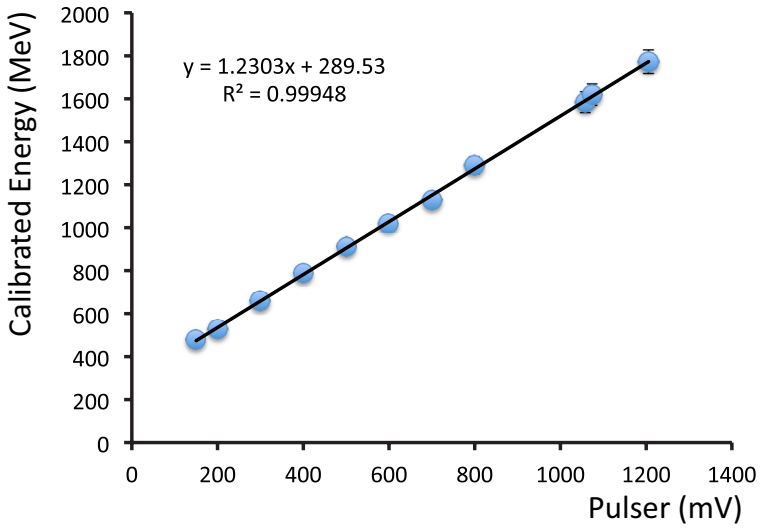

(a) Triplet (QTS) energy calibration and fit parameters utilizing the picket-fence method with elastically scattered beam particles. Error bars are shown; some are smaller than the points.

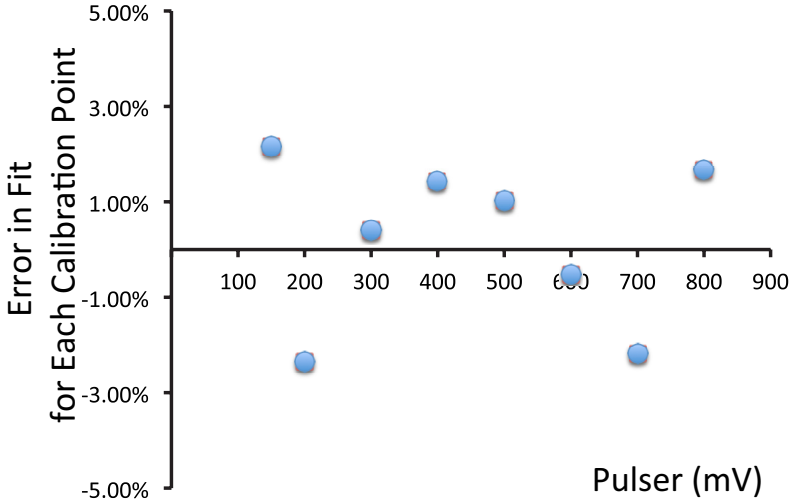

(b) Triplet (QTS) energy calibration fit error derived from fit in Figure 3.23a.

Figure 3.23: Triplet (QTS) energy calibration and fit parameters utilizing the picket-fence method with elastically scattered beam particles. Error bars are shown; some are smaller than the points.

3.5 Energy Versus Time-of-Flight (E-ToF) Time and Mass Calibration

3.5.1 E-ToF Time Calibration

Time calibration was achieved via a set of picket-fence style pulser calibrations. Each line on the TDC or TAC-ADC spectra was representative of a specific delay introduced into the timing signal for a bank of detectors. In this way, it was possible to get an accurate measure of the resolution of the respective TDC or TAC-ADC time spectra. The time calibration for the triplet silicon detector is shown in Figure 3.24. The time per channel as determined by this calibration was 50.0ps per channel with an error of ±0.8%. This is the expected value based on a full range setting of 200ns on the TAC. This calibration was then used to determine linear fit parameters

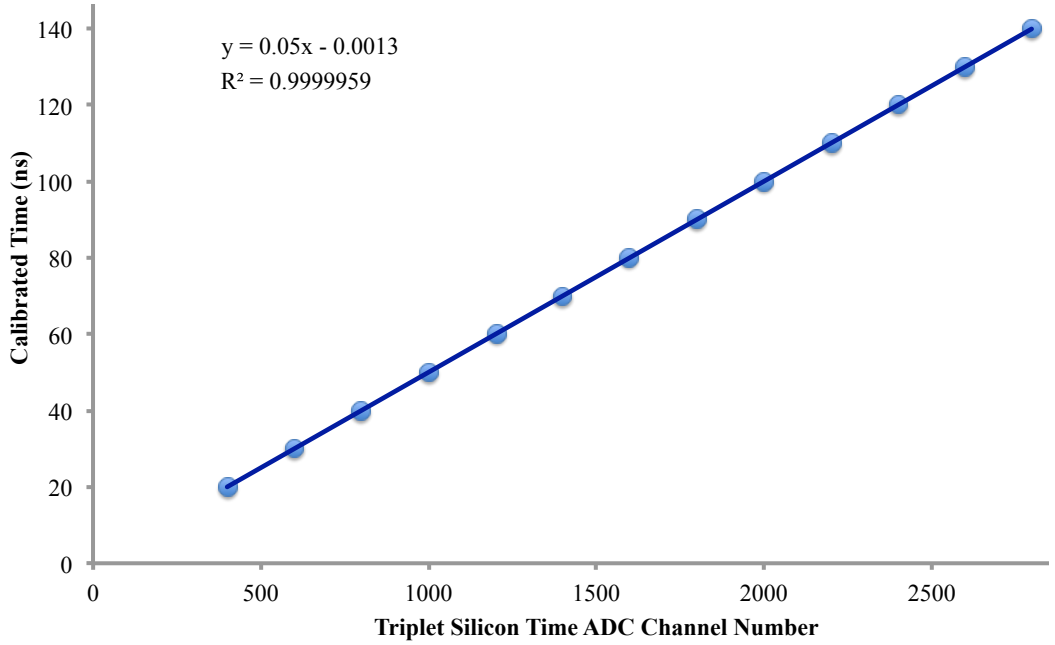

Figure 3.24: Triplet (QTS) time calibration and fit using PPAC-to-PPAC time-of-flight. Error bars are shown and are typically smaller than the plotted calibration points.

for the time calibration of the raw data. The centroid of the timing signal from the experimentally scattered elastic beam particle from each of the three physics systems was chosen from the energy versus time plot for the given detector. In this way, the pulser determines the slope or linearity of the calibration and the beam gives the intercept. The mean free path to the detector, mass and calibrated energy of the scattered beam particle are known and used in the time calibration. Using a relativistic technique, the time of flight of the elastically scattered particle was determined. More specifically in the case of particles detected in the QTS, we first determined γ from the equation:

$$\gamma = \left(\frac{E}{931.5 \cdot A}\right) + 1 \tag{3.13}$$

where E is the calibrated energy and A is the mass of the elastically scattered beam particle. Using Eq. 3.13, we can then determine the velocity (v/c) of the particle through the QTS via:

$$\beta = \sqrt{1 - \left(\frac{1}{\gamma^2}\right)} \tag{3.14}$$

and through a simple conversion

$$v = \beta \cdot 29.9792458 \tag{3.15}$$

to get the velocity in terms of cm/ns. Thus, the time of flight of the particle can be calculated via

$$t_0 = L/v \tag{3.16}$$

where L is the flight path between PPACs. In the case of the triplet, the elastically scattered particles via simulation deviated from the linear flight path by a few mm

over the 547.6 cm linear distance, PPAC-to-PPAC. Therefore, the linear flight path between PPACs was used in the calculation of the flight time. The time calibration function is shown in Eq. 3.17. In Eq. 3.17, ToF is the flight time and Channel$\#_{particle}$ is the raw time channel number of the particle, t_0 is defined in Eq. 3.16, Channel$\#_0$ is the channel number of the elastically scattered beam particle used to calibrate t_0, and W_{bin} is the width of the ADC channel in time (50ps in this case) as determined via linear fit in Figure 3.24.

$$ToF = t_0 + ((Channel\#_0 - Channel\#_{particle}) \cdot W_{bin}) \tag{3.17}$$

3.5.2 E-ToF Mass Calibration

At this point, the mass calibration can be found by determining the velocity of the particle using the known flight path and time of flight(Eq. 3.18). Then through determination of the Lorentz factor (Eq. 3.19) and using the calibrated energy of the particle, the mass can be determined as in Eq. 3.20.

$$\beta = \frac{L}{t \cdot c} \tag{3.18}$$

$$\gamma = \frac{1}{\sqrt{1-\beta^2}} \tag{3.19}$$

$$A_{\text{E-ToF}} = \frac{E_{frag}}{(\gamma - 1) \cdot 931.5} \tag{3.20}$$

The mass of each particle identified by E-ToF is determined on an event-by-event basis.

However, mass lines for even numbered masses were analytically determined for a range of masses by calculating a number of points in energy and time for masses from A = 110-148. As seen in Figure 3.25, mass lines laid over top of an actual

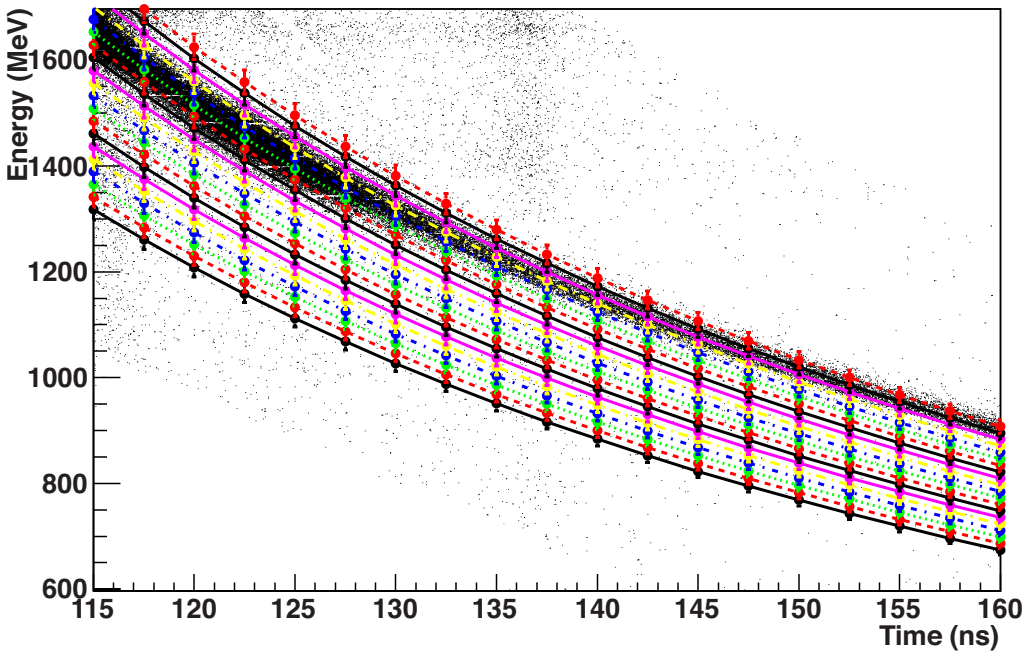

Figure 3.25: Triplet (QTS) calibrated using calibrated PPAC-to-PPAC time-of-flight (Figure 3.24) and calibrated silicon energy(Figure 3.23). Error bars are shown for both time and energy. Each new line represents an even mass number ranging from A=110 (lowest black, solid line) to A=148 (upper red, dashed line).

energy vs. time 2D histogram for QTS events in coincidence with a FAUST event have small error bars for both the energy and time component. The energy and time calibrations used for calculating the mass lines are the same ones previously derived in Sections 3.4.2 and 3.5.1, respectively. In this way, the calibrated experimental data and the plotted mass lines are from the same calibration set. The time error bars are smaller than the plotted points and are not visible. It can be seen that, in fact, there are masses close to that of the elastically scattered particle at higher energies (low damping) but the detected particles get progressively heavier as the energy gets lower and the time of flight lengthens. The masses at lower energies and time, show that there is an increase in mass for these PLFs that have been

damped due to possible nuclear interaction. This, along with the associated reaction dynamics and mechanism analysis, will be further discussed, in Section 5.

3.6 Physics Tapes Production

As in the particle identification technique, several sets of tapes were produced prior to finalizing the final "Physics Tapes". Raw tapes were first produced from the experimental data by reading out the raw data collected by the front-end computer and translating them into tapes readable by the analysis software. This translation/conversion involved the production of reduced physics tapes from the raw physics tapes. Both the raw and reduced physics tapes had event-by-event information of the signal recorded by each ADC and TDC. The detector identification number and type was present in both the raw and reduced tapes. This was possible as the C++ objects for reading out the data from the VME modules was preprogrammed to represent the detector number, location, and type *a priori*. The reduced tapes were used in the linearization (Section 3.3.2) and Gaussian fitting processes (Section 3.3.3).

The reduced tapes, combined with the linearization and Gaussian fitting data base, were then used to create particle identification (PID) tapes. In the PID tapes, the information for each fragment was written to event-by-event data structures where information was retained both for the entire event and each individual particle within that event. These were referred to as PIDEvent and PIDParticle objects, respectively. Each PIDParticle object contains the charge, mass linearization value (LinZ), percent contamination, fraction of sigma and the mass identification for each FAUST ΔE-E (full or attenuated) detector type.

The final tapes produced, referred to as "Physics Tapes" or PhysTapes, are used for all the subsequent analysis discussed herein. The PhysTapes contain only frag-

ments that have a correct particle identification (Z and/or A), energy and time calibration. The physics particles (PhysParticles) contain information similar to the PIDParticle except that in the production of the PhysTapes, the correct, calibrated energy (and identifying detector type) is recorded. The PhysTapes contain the A and Z identification as well as the calibrated energy, momentum, velocity, theta and phi all in both the center-of-mass and laboratory frame of reference. In the case of the particles detected in the E-ToF channels, the mass is calculated using the energy and time calibration described above in Sections 3.4.2 and 3.5.1. The theta and phi angles of each particle are determined from their respective detector number that they were identified in. Using the known angular coverage of each detector, as determined by computer aided design (CAD) drawings and read from a detector map ASCII file, it was possible to Monte-Carlo over the possible range of angles covered by a given detector. In this way, the PhysParticle retained the mean theta and phi value and the randomized theta and phi value of the given detector for each accepted particle. In the case of particles detected in the QTS that had a $\theta = 0.9°$-$2.3°$ or $\phi = 0°$-$360°$ in PPAC#1 (a fine granularity, position sensitive detector) the theta and phi were kept and recorded for both the real and Monte-Carlo calculated theta and phi. Where the theta angle was outside this range in a few particles, either due to noise or double hit in the PPAC, the theta and phi were determined via Monte-Calro calculation over the range mentioned above.

The final charge and mass identification of the particle was kept along with its associated %Contam and pSigma value. In the case of a particle not having an isotopically resolved A (or Z in the case of E-ToF), a GuessA (or GuessZ) was assigned. There are three assignment schemes for the guessed values based on the range of the known value of Z (or A) for the given particle. If a particle had a known Z (elementally identified) from Z = 1-9 but no isotopically identified A, then the GuessA would

be the most probable A for a given Z based on the isotopic abundance determined via other detectors with isotopic resolution from the same reaction system within the data collected for this thesis. Otherwise, if $10 \leq Z \leq 39$, the GuessA value was determined by bootstrapping[121] (randomly sampling) isotopic distribution tables as determined by Souliotis et al[114] using MARS[122] resulting in a narrow distribution around the most probable A for a given Z. A similar method was used for particles where the mass was determined by E-ToF and a GuessZ was required. For A $\leq$20, the most probable isotope from the experimental data was used. For $21 \leq A \leq 89$, the bootstrapping isotopic distribution tables as determined by Souliotis et al[114] was used resulting in a narrow distribution around the most probable Z for a given A. For A $\geq$90, the most probable charge was calculated based on the valley of stability through a form of the semi-empirical mass formula shown in Eq. 3.21.

$$Z = \frac{23.7 \cdot A}{(0.71) \cdot \left(\frac{A^{\frac{2}{3}}}{2}\right)} + 2 \tag{3.21}$$

A specific constraint was not placed on the pSigma or %Contam allowing constraints to be varied later on, if required, for different analysis. Lastly, the momentum and velocity vectors in both the lab and center-of-mass frames, determined from the accepted energy and angle, were calculated in the PhysParticle object.

3.7 Experimental Software Filter

To compare simulated data with experimental data, the simulated data was first run through a software representation of the FAUST-QTS called the FAUST-Filter[123, 124, 125]. For this experiment, the FAUST filter was updated by structuring the software to be similar in structure to the NIMROD-ISiS filter (or NimFilter). This makes the filter more compatible between the two data analysis software suites.

The FAUST-Filter takes into account the geometry and energy thresholds of each element and isotopes for each detector as determined by experimental data. This data is stored in a database containing the energy threshold for each identified isotope by detector for this particular experiment. Filtering the theoretical simulation data allows the theoretical calculation to be processed and examined the exact same way as the experimental data.

4. CHARGED ION TRANSPORT ANALYSIS

An important feature of using a spectrometric device in a nuclear physics experiment is understanding the physics that affect particle transport. This is important in order to efficiently detect the particles of interest. The Optical and Transport considerations required to conduct this experiment are detailed in Section 4.1. This detailed background is then followed by an analysis of the effects of elastics scattering with respect to particles of interest through FAUST-QTS. This is of great interest as the spectrometer is centered at $\theta = 0^\circ$ in the laboratory frame of reference. This requires careful consideration of the physics involved as detailed in Sections 4.2 and 4.3.

4.1 Optics and Transport Analysis

As detailed previously, in Section 3.2.3, FAUST-QTS is a forward array coupled to a triple quadrupole spectrometer. The physical, geometric acceptances of the spectrometer are shown in Figure 4.1 as they were previously shown in Section 3.2.3. The unreacted beam at $\theta = 0^\circ$ is stopped in the Faraday cup while the reaction products and scattered beam that escape through the center of ring A in FAUST are refocused through the QTS. The refocused particles are identified by E-ToF through two PPACs and a thick silicon detector. The particles' mass, charge state, angle of entrance into the spectrometer, and momentum are all careful considerations that must be taken into account when calculating charged particle transport flight paths. Since the spectrometer is at $\theta = 0^\circ$ and without any electro-magnetic devices upstream, the spectrometer is bombarded by particles with a wide range of magnetic rigidities (Bρ). The particles of interest must be refocused and detected while the remainder of particles must either be removed prior to the entrance of the spectrometer (by FAUST or Faraday cup in this experiment), focused off the focal plane, or

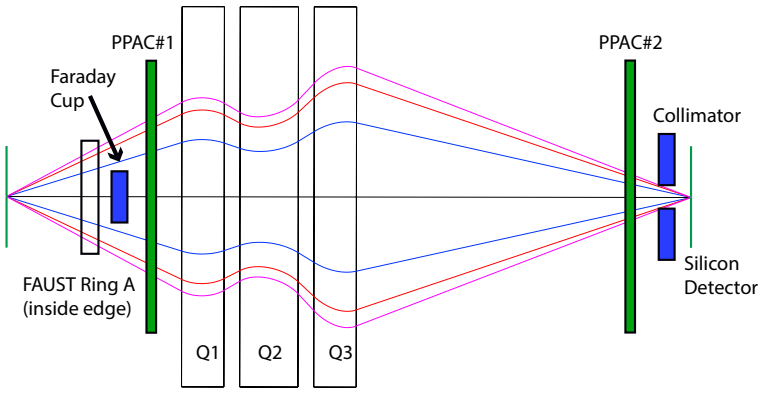

(a) XZ-optics coordinate plane

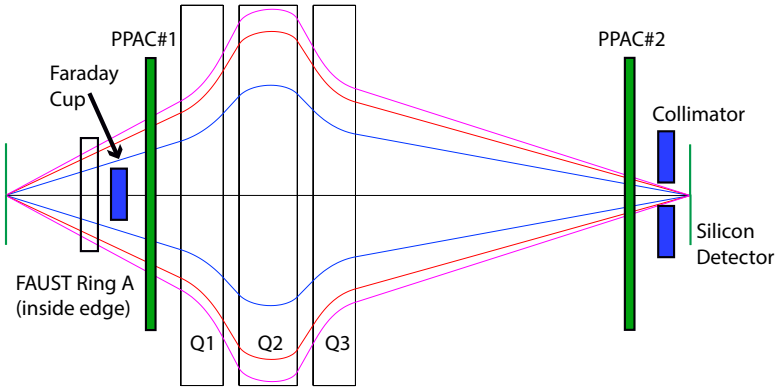

(b) YZ-optics coodrinate plane

Figure 4.1: COSY-Infinity simulations showing the flight path of ^{136}Xe at 15 MeV/nucleon at a three, discrete theta angles (purple = 1.7°, red = 1.5°, blue = 1.0°) at a constant magnetic rigidity (Bρ = 1.45Tm). The optics calculations only take into account 1st order effects and are for demonstration purposes only.

detected and VETO-ed out by electronics *ex post facto*.

Several rounds of simulations have been examined for a number of probable cases of transport through the QTS using RAYTRACE[106] and COSY-Infinity[107]. The QTS is not a symmetric spectrometer. The entrance flight path is significantly

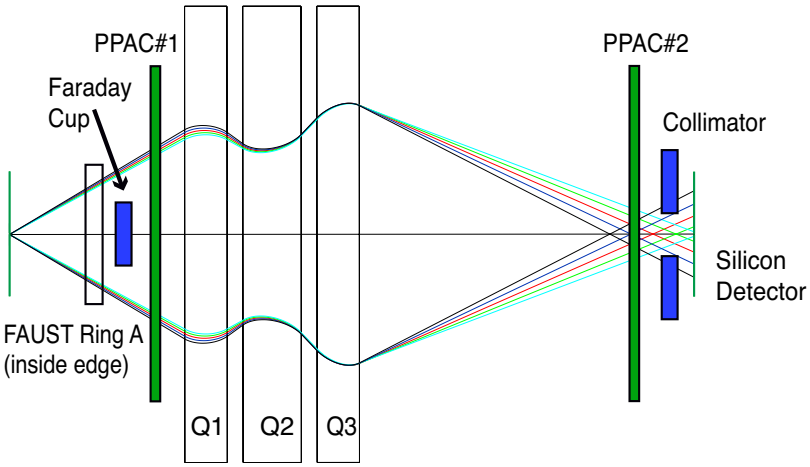

(a) XZ-optics coordinate plane

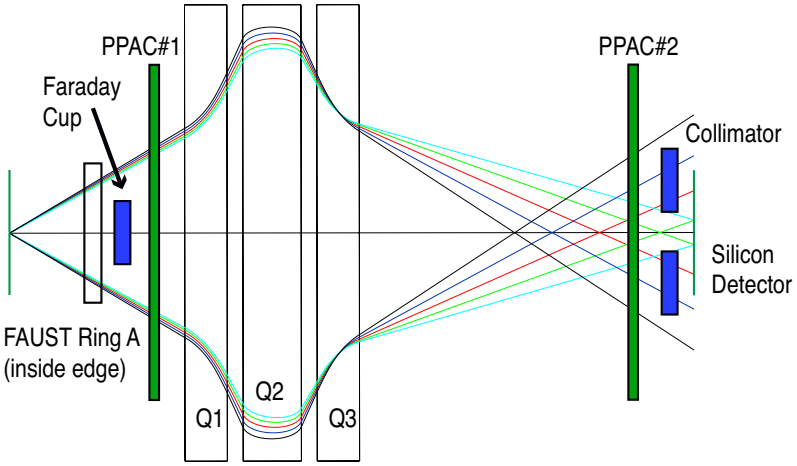

(b) YZ-optics coodrinate plane

Figure 4.2: COSY-Infinity simulations showing the flight path of ^{136}Xe at 15 MeV/nucleon at five, discrete magnetic rigidities centered around a constant magnetic rigidity setting of Bρ = 1.45Tm for the QTS magnets. The five settings are represented by values in increments of $\pm$5% of the rigidity setting of the QTS (Bρ = 1.45Tm). The optics calculations take into account 3rd order effects and represent a single theta value of $\theta = 1.5°$. Red = $\pm$0%Bρ, Light Blue = +5%Bρ, Dark Blue = $-$5%Bρ, Green = +10%Bρ, and Black = $-$10%Bρ

shorter than the exit flight path, requiring careful calculation of the magnetic fields required to transport particles of interest. As one would expect, the higher-order

field effects are fairly significant. Simulations via COSY-Infinity illustrate the effects of Bρ on focusing particles through the triplet as shown in Figure 4.2, where Quadrupole#1 (Q1) and Quadrupole#3 (Q3) have decoupled (unequal) magnetic fields. Previously we have seen that if the triplet behaved to 1^{st} order, the transport would be simpler, but would also not afford the opportunity to remove unwanted particles after refocusing. The fact that there are higher (up to 3^{rd}) order effects predicted, allows for careful placement of collimation after Q3 to aid in re-focusing the image of the particle of interest with decreased contamination from other particles. Such collimator also alleviates some of the dependance on the use of electronics *ex post facto* as the only other means to remove contamination from the particles of interest via computer VETO or FAST CLEAR. Figure 4.2 illustrates several values of Bρ for a single theta value of $\theta = 1.5°$. As the value of theta increases (up to a maximum of $\theta = 2.3°$) so do the aberrations in the focal image. This is particularly true for the YZ-plane where it can be seen that even at $\theta = 1.5°$ the flight path of the particles are nearing the edge of the triplet aperture in the 2^{nd} quadrupole magnet (Q2).

Corrections to the higher-order effects can be made by decoupling the magnetic fields on Q1 and Q3. By decreasing the Q3 magnetic field by 5% of that on Q1, there is a significant decrease in the predicted aberrations. Typically, for a symmetric spectrometer, the coupling of the X-focusing magnets (Q1 and Q3) would be preferred. However, the decoupling of Q1 and Q3 in the QTS improves the focusing power by decreasing the focal plane aberration.

4.2 Geant4-Raytrace Analysis of Elastic Scattering

In addition to aberrations in the focal plane image and exclusion of reaction products not of interest and elastically scattered beam particles, it is also impor-

tant to ensure that inelastic particles are not swamping the data stream or masking the particles of interest detected at the focal plane of the QTS. To address this concern, GEANT4[126] was used to simulate elastically scattered beam particles through FAUST-QTS. GEANT4 is a software tool that models the interaction of particles with matter. We used the package to model the interaction of elastically scattered beam-like particles within the FAUST-QTS prior to filtering with RAYTRACE. The entire FAUST array and the QTS, up to the entrance of the first quadrupole magnet, were constructed inside of GEANT4. The simulation included the Faraday cup located between FAUST and the QTS as shown in Figure 4.3. The physical beam

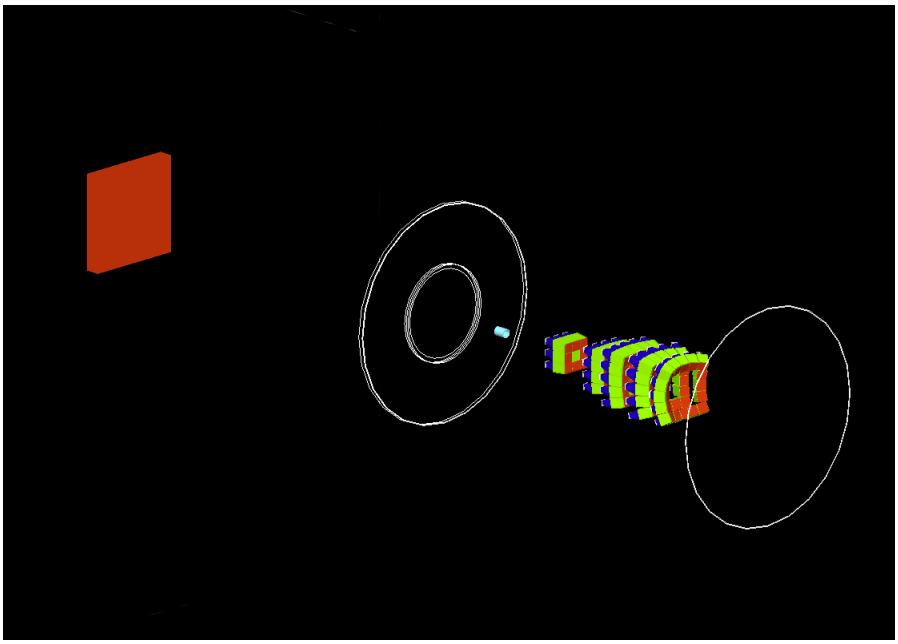

Figure 4.3: Cross Sectional view of the FAUST-QTS in GEANT4. The FAUST array is shown as the array of five, multicolored rings. The large, red square detector behind the FAUST array represents the front of the first quadrupole magnet. The beam piping is hidden to allow the display of the detectors and beam line components. The small blue cylinder behind the FAUST array is the Faraday Cup covering a range of $\theta = 0 - 0.9°$. Note, the beam enters from the right of the figure.

piping is not shown in the figure for display purposes. However, it was included in the simulation for geometric constraints. The elastic scattering cross-section as a function of θ was extracted from LISE++ using the reaction of ^{136}Xe+^{64}Ni at 15 MeV/nucleon. The cross-section was found to vary with θ^{-4}. One billion primary elastics were simulated covering an angular range of $\theta = 0.75^\circ - 2.3^\circ$. Ring A of FAUST was allowed to act as a collimator in order to achieve the correct, square angular distribution in θ and ϕ. Of particular interest were particles that interacted with the knife edge of the cup[127, 128]. Once the particles interacted, it was postulated that a small number of particles could lose energy, be inelastically scattered, enter the triplet and be mistaken for particles of interest at the focal plane of the QTS. This possibility exists because the knife-edge scattered particles span a range of energy that overlaps with the energy range of the PLFs of interest. This combined with the fact that the inelastic (knife-edge) scattered beam particles are near the same mass as some of the PLFs of interest drew some concern.

Particles that survived the passage through FAUST and entered the QTS were then analyzed via RAYTRACE. The particles were divided by software flag as to whether or not they had interacted with the cup and were analyzed separately as to be able to efficiently retain the identity of the ray through the analysis. Reasonable rays for RAYTRACE were considered to be rays with a ΔB$\rho\pm$10% of the central Bρ =1.45 Tm covering an angular range of $\theta = 0.75^\circ - 2.3^\circ$. However, the acceptance criterion of what defined a reasonable ray was tested. As such, the ΔBρ was varried $\pm$10% and $\pm$5% with an angular acceptance decreased to $\theta = 0.75^\circ - 1.7^\circ$. This had negligible effect on the number of knife-edge scattered particles that made it through the triplet. As such, the criterion for defining a reasonable ray was retained at ΔB$\rho \pm 10\%$ and $\theta = 0.75^\circ - 2.3^\circ$. Using the same settings, events of interest from CoMD were also transported through the QTS in order to analytically determine the efficiency

ratio between knife-edge scattered particles to events of interest, as described in Section 4.3. This was done as the knife-edge scattered particles presented the slight possibility of being misinterpreted as PLFs of interest.

4.3 Transport Efficiencies and Events of Interest Coincidence Analysis

A large number of elastics from the simulation were lost in the cup from $\theta = 0.75^\circ \sim 0.89999^\circ$. However, the angular coverage was required to ensure that any particle that interacted with the lip of the cup was examined. The angular coverage of $\theta = 0.75 - 0.89999^\circ$ represents the region covered by the lip (wall) of the Faraday cup. Of the one billion events that were simulated, 5.68391×10^8 particles arrived at the entrance of the triplet. Table 4.1 tabulates the transmission of beam-like, scattered particles to the triplet. There is $\sim 2.9 \times 10^{-4}$ difference in intensity between elastic and inelastically (knife-edge) scattered beam particles. Analysis of the transport through RAYTRACE found there was an efficiency ratio of 3:4 for the elastics vs. inelastic particles respectively. The CoMD events of interest were found to have an efficiency of 68% through the QTS. The transport efficiency of the events of interest from CoMD was expected to be high as this is where the QTS is tuned. The total CoMD event ensemble covered a triangular impact parameter distribution ranging from b = 0 - 15 fm, with the events of interest accounting for 0.7% and the elastics accounting for ∼50% of the total distribution. It was found that without regard to coincidence events between FAUST and the QTS, 1:40 particles detected at the focal plane of the QTS could be inelastically scattered knife-edge particles.

However, when one takes into account the low beam rate of 1.5×10^5 particles per second (pps), an ADC gate width of 2 μs and a coincidence requirement between FAUST and the QTS to be considered to generate PID Tapes, the probability diminishes quickly. Using a Poissonian distribution to estimate the probability of two

Table 4.1: Transmission of particles through the QTS

Particle Type	# of Events in QTS	% Efficiency
Pure Elastics	5.68199×10^8	3%
Inelastics	1.98115×10^5	4%

beam particles in one cycle (beam burst) from the cyclotron, it was determined that a 1:14,520 probability existed, thereby rapidly decreasing the chance of getting real physics events of interest with a coincident inelastically scattered beam particle.

5. REACTION MECHANISMS AND DYNAMICS ANALYSIS

Reaction dynamics below the Fermi energy provide a complex environment to probe reaction mechanisms and to investigate the interplay between a range of competing mechanisms. This energy regime also provides for an environment to learn about the transition from quasi-fission to multi-fragmentation. Additionally, there have been a number of theoretical observables proposed to be sensitive to the symmetry energy[25, 45, 11, 44, 48, 41, 47, 46] particularly associated with the ternary breaking of the reaction system. There has been a range of experimental work at or above the Fermi energy[26, 50, 57, 58, 59, 60, 61, 62, 63, 64, 65, 66, 67, 68, 69, 70] undertaking systematic studies by looking at the reaction dynamics and mechanisms. There has also been work done using a number of heavy, mostly symmetric, systems examining the evolution of the reaction system at energies just below the Fermi energy[56, 55] with more recent work progressing toward more asymmetric systems over a range of energies[76, 77, 129]. However, the studies have largely focused solely on the reaction dynamics with little exploration toward the influence of the symmetry energy. We are interested in exploring the reaction mechanism in the energy regime covering the transition from quasi-fission to multi fragmentation and how the symmetry energy might influence these mechanisms. Specifically we have chosen to focus on the ternary breaking of the reaction system into three heavy reaction partners. We are interested in looking for the breaking of the quasi-projectile into an IMF and a PLF as it has been predicted to be sensitive at this energy[25, 45, 11, 44, 48, 41, 47, 46].

Since we are interested in the breaking of the reaction system into three heavy fragments (Z$\geq$3) in semi-peripheral to peripheral collisions ($b \sim 5 - 9fm$), it is

important to impose cuts on the physics data to ensure the events of interest are selected appropriately. The event selection for particles detected in FAUST-QTS will be discussed in Section 5.1. A description of the reaction plane and specific cuts associated with analyzing the reaction plane will be discussed in Section 5.2. In Section 5.3, an analysis focused on Quasi-Projectile (QP) break-up correlations will be discussed. In Section 5.4, a comparison of the experimental results to those from the dynamical and statistical models will be made. Finally, in Section 5.5, we examine the dynamical vs. statistical nature directly of experimental events to tease out more detailed information about the underlying, dynamical reaction mechanisms.

5.1 Event Selection

A number of event selection cuts were made on the physics data in order to facilitate the analysis with respect to the reaction mechanisms resulting in a 3-body fragmentation of the reaction system. As mentioned in Section 3.3.4, the PhysTapes already contain events in the QTS that are coincident with particles in FAUST. In this Section, and subsequent analysis, the data will only be analyzed for those events where there are two particles with Z$\geq$3 (multiplicity = 2). In this experiment, the detector thresholds were such that we don't expect to detect the quasi-target (QT). Figure 5.1 shows the multiplicity of events with Z$\geq$3. The events with multiplicity = 2 for fragments with Z$\geq$3 (shaded in red) are about an order magnitude less than the multiplicity = 1 events and approximately two orders of magnitude greater than the number of events with multiplicity ≥ 3.

Additionally, cuts have been placed on the triplet particles such that only particles that are PLF-like (not beam-like) and within the mass range of $A = 100 - 190$ are accepted. The process of applying cuts can be visualized in a series of figures. First, looking at the energy vs. time (E vs. T) histogram in Figure 5.2a, there are already

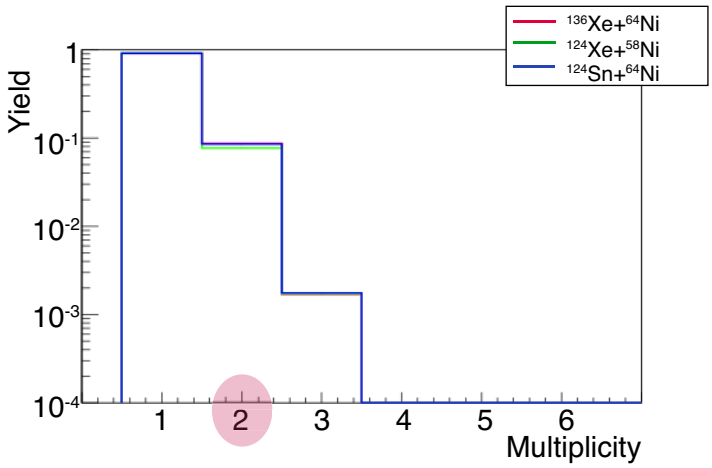

Figure 5.1: Normalized yield of heavy fragment ($Z \geq 3$) multiplicity. Shaded region highlights a multiplicity=2 representative of a 3-body breaking of the system. The QT will not be detected in the current detector arrangement. All three systems are overlaid and color codes as per the legend.

a number of features present due to the acceptance logic detailed in Section 3.3.4. Namely, it is required that particles in the triplet must be coincident with a particle in FAUST and the mass of the particles in the triplet must be between A=100-190. The parabolic hard cut-off in near the top of the E vs. T plot represents the mass of $A = 190$. The parabolic hard cut-off near the bottom represents mass of the $A = 100$. The wide horizontal band at $E = E_{beam}$ represents energetic PLFs (or beam) that had a coincident IMF or noise which created a timing signal in PPAC#1, thereby smearing the time. The wide, vertical band at $t \sim 110$ ns represents incomplete charge collection in the silicon detector at the focal plane of the triplet for beam-like particles. The incomplete charge collection could be due to the fact that the beam and energetic PLFs were focused at very discrete positions on the face of the silicon detector causing radiation damage, and also near the center of the detector where the quadrant junctions exist. Next, cuts on energy and time were applied as represented in Figure 5.2b. The green shaded area represents a cut in time and the red shaded

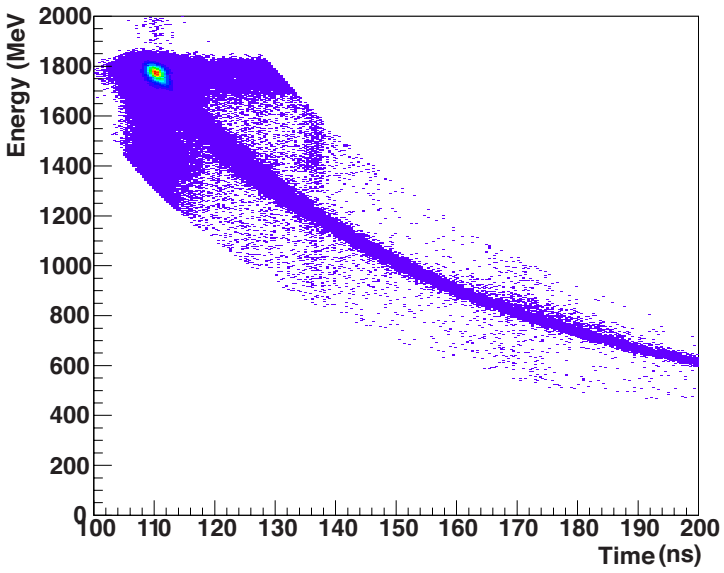

(a) Raw Energy vs. Time histogram as written to the PhysTapes

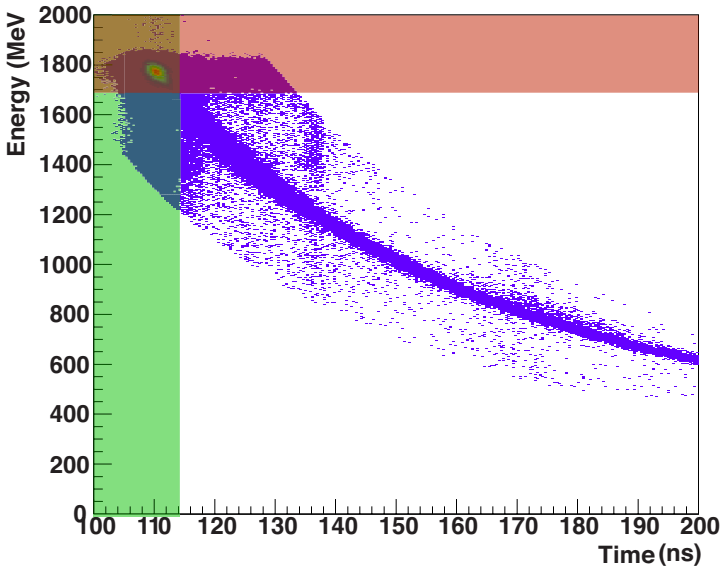

(b) Raw Energy vs. Time histogram as written to the PhysTapes with cuts in energy and time to remove beam-like PLFs. The reaction system ^{136}Xe $+^{64}$ Ni is shown for illustrative purposes but all systems have the same time cut and similar energy cuts. The surviving PLFs in the unshaded region are likely the result of a damped collision at mostly semi peripheral impact parameters.

Figure 5.2: Cuts in energy vs. time applied to the QTS energy vs. time spectrum. Cuts are described in each subfigure.

area represents a cut in energy to remove beam-like particles, as we are interested in semi-peripheral collisions with significant damping. The time cut is applied to all systems the same. However, the energy cut was applied so it just removed the beam-like PLFs with $E_{PLF} > 0.88\% \cdot E_{beam}$. The surviving PLFs, in the unshaded region, are likely the result of a damped collision at mostly semi peripheral impact parameters. Because we have focused on events with multiplicity = 2 for particles with Z≥3, the two heaviest fragments (IMF and PLF) are assumed to account for a majority of the momentum of the quasi-projectile source. A final additional cut is made on the physics data before it is processed for analysis in the subsequent sections. This final cut consists of removing QPs with an QP energy (E_{QP}) less than 25% of the beam energy (E_{beam}) or

$$E_{QP} > 0.25 \cdot E_{beam} \tag{5.1}$$

as shown in Figure 5.3. E_{QP} is defined as the sum of the PLF and IMF lab frame kinetic energies as described by Baran[44]. Anything less than $E_{QP} > 0.25 \cdot E_{beam}$ cannot justifiably be called a QP as most of the energy has not been collected and there is a natural cut-off in the 1D histogram at this energy.

Since the QT in this experiment is not detected, all other particles (except the PLF and IMF) are assumed to have originated from the QT. As such, we determined the properties of the QT through momentum conservation. The QT reconstruction procedure will be discussed in greater detail in Section 5.2.

5.2 Reaction Plane

Since the reactions of interest are dynamical in nature, as outlined in the introduction (Section 1.2), it is important to define the reaction plane to better describe the observed phenomena. In Figure 5.4, the parallel velocity (V_{par}), or the veloc-

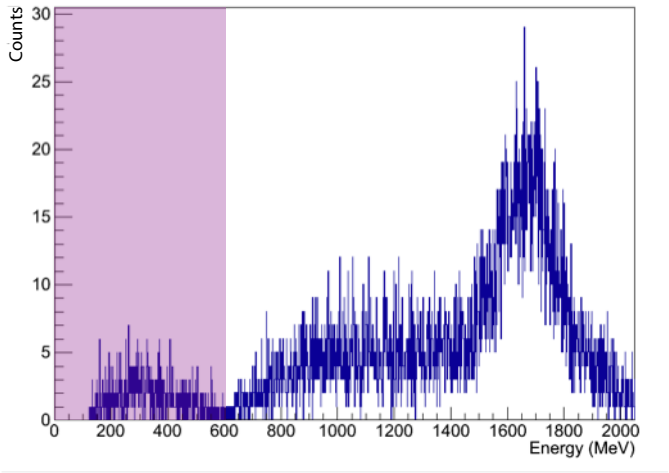

Figure 5.3: Energy cut applied to the reconstructed QP energy spectra. Shaded region represents the region of $E < 0.25 \cdot E_{beam}$.

ity parallel to the beam direction, versus the perpendicular velocity (V_{perp}) in the laboratory frame of reference is shown. It can be seen that a majority of the reaction products from QP breakup are forward focused as one would expect, because of both the inverse kinematics of the reaction system and detector acceptance. The anisotropic distribution of particles can be better described and treated analytically by calculating the reaction plane oriented distributions. The following sections will go into detail of the description of the reaction plane and terminology. Additionally, a description of the cuts on QP energy and mass used to disentangle some of the observables will be described.

5.2.1 Definition of Reaction Plane

Using the velocity of the two heaviest detected fragments (the PLF and the IMF in the case of a 3-body breaking), the velocity of the QP can be reconstructed. Much of the terminology[50, 58, 59, 62, 63] has been in use since first described by Stefanini et al.[55]. The velocity of the QP in the center of momentum as determined by the

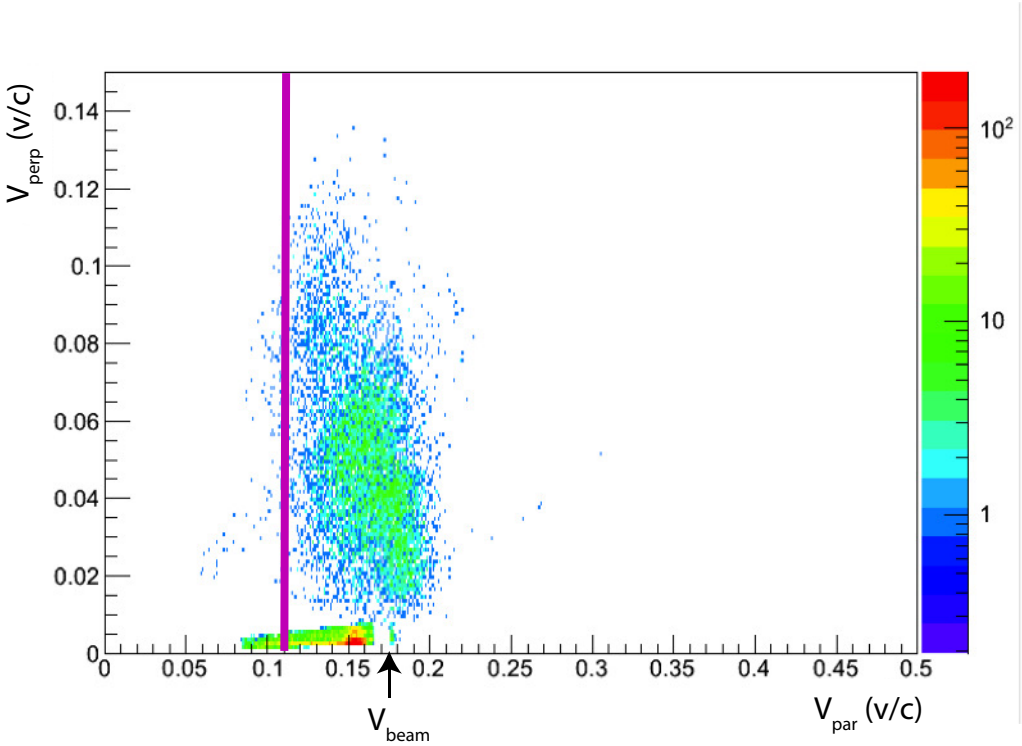

Figure 5.4: Parallel vs Perpendicular velocity of the fragments detected from the QP breakup. The mid velocity (center of momentum) is indicated by the vertical, purple line. The beam velocity is indicated by the arrow. A large portion of the particles are emitted in the forward directions in the center of momentum frame as expected.

two heavy fragments is defined by

$$\vec{v}_{QP} = \frac{\vec{v}_{PLF} \cdot m_{PLF} + \vec{v}_{IMF} \cdot m_{IMF}}{m_{PLF} + m_{IMF}} \tag{5.2}$$

where $\vec{v}_{PLF}$, $\vec{v}_{IMF}$, m_{PLF}, and m_{IMF} are the velocities and masses of the PLF and IMF respectively. This can be visualized in Figure 5.5 where the red line connecting the white circle (the QP) with the red circle (the QT) represents the axis of separation between the QP and the QT. The velocity of the QP ($\vec{v}_{QP}$) is aligned along this axis. The $\vec{v}_{QP}$ starts at the center of momentum and points in the direction of the

QP. The unit vector representing the separation axis ($\vec{n}_{sep}$) can be described by

$$\vec{n}_{sep} = \frac{\vec{v}_{QP} - \vec{v}_{QT}}{|\vec{v}_{QP} - \vec{v}_{QT}|}. \tag{5.3}$$

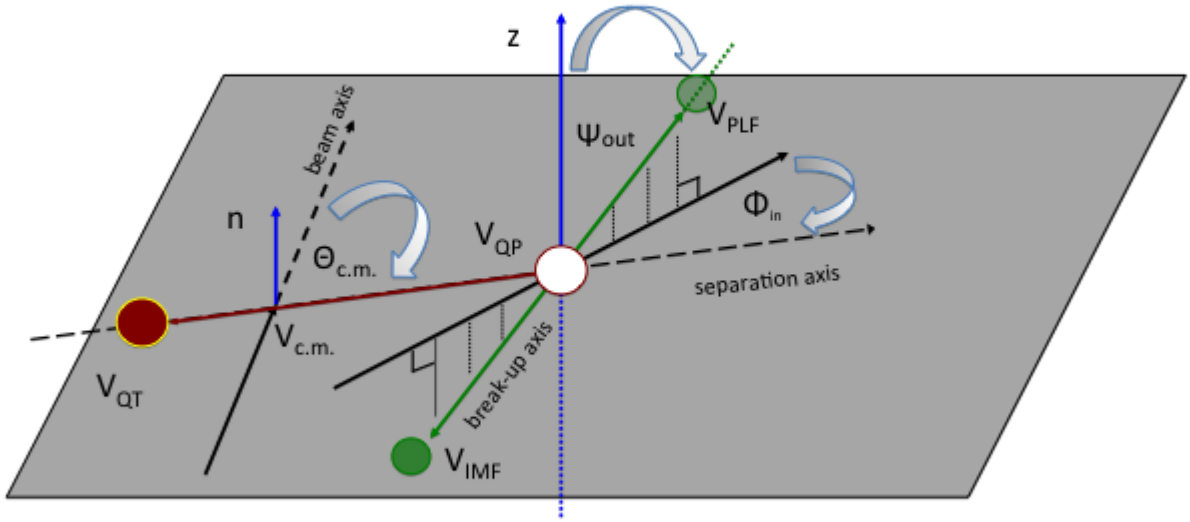

Figure 5.5: Schematic of the Reaction Plane indicating the definition of the in- and out-of-plane angles Φ_{in} and Ψ_{out}, respectively. **n** is the vector normal to the reaction plane (grey plane). The PLF in this case is shown deflected out of the reaction plane ($\Psi_{out} < 90°$) and in the direction of the beam ($\Phi_{in} > 0°$).

However, since the QT is not detected in the experiment, the QT has been reconstructed using the QP velocity and applying momentum conservation laws. Specifically, the momentum of the QP in the center of momentum frame ($\vec{p}^{QP}_{CM}$) can be calculated by

$$\vec{p}^{QP}_{CM} = m_{QP} \cdot \vec{v}_{QP} \tag{5.4}$$

where m_{QP} and $\vec{v}_{QP}$ and the mass and center of momentum velocity of the QP respectively. Assuming that all particles not detected in the PLF and IMF must be contained in the QT, that there are only two reaction partners at the time of separation, and that any pre-equllibrium emission of LCPs are negligible, the momentum of the QT in the center of momentum frame, $\vec{p}^{QT}_{CM}$, can be estimated by

$$\vec{p}^{QT}_{CM} = -\vec{p}^{QP}_{CM}. \tag{5.5}$$

The $\vec{v}_{QT}$ in the center of momentum of the systems can be calculated by

$$\vec{v}_{QT} = \frac{\vec{p}^{QT}_{CM}}{m_{QT}}. \tag{5.6}$$

The reaction plane (shown in gray in Figure 5.5) can be defined by beam velocity vector ($\vec{v}_{beam}$) and the QP-QT separation axis ($\vec{n}_{sep}$). The vector normal to the reaction plane ($\vec{n}_{norm}$) is defined by

$$\vec{n}_{norm} = \frac{\vec{n}_{sep} \times \vec{n}_{beam}}{|\vec{n}_{sep} \times \vec{n}_{beam}|}. \tag{5.7}$$

The vector $\vec{n}_{beam}$ is the unit vector of the beam axis. The "break-up axis" of the QP is defined by the relative velocity between the two heaviest fragments and is defined by

$$\vec{v}_{rel} = \vec{v}_{PLF} - \vec{v}_{IMF} \tag{5.8}$$

with the vector pointing in the direction of the heavier PLF (not the lighter, emitted IMF). The unit vector for $\vec{v}_{rel}$ will be defined as $\vec{n}_{fiss}$ (in keeping with the established nomenclature[50, 55, 58, 59, 62, 63]) for the remainder of this discussion. The out-of-plane angle, Ψ_{out}, details the deflection of the break-up axis with respect to the

vector normal to the reaction plane, $\vec{n}_{norm}$ (Figure 5.5). The in-the-reaction-plane azimuthal angle (in-plane angle), Φ_{in}, describes the angle of the in-plane projection of the break-up axis with respect to the QP-QT separation axis ($\vec{n}_{sep}$). The angle Φ_{in} will be considered positive when both $\vec{n}_{sep} \times \vec{n}_{fiss}$ and $\vec{n}_{norm}$ point into the same half space. Using this sign convention, positive values of Φ_{in} correspond to the PLF being deflected toward the beam direction. The chosen orientation of the break-up axis allows Φ_{in} to vary from -180° to 180° and refers to the direction of the PLF velocity.

The system-to-system angular distributions of Ψ_{out} and Φ_{in} are shown in Figure 5.6. Each system is color coded as shown in the legend. In Figure 5.6a, the Ψ_{out} distribution is clearly centered around the reaction plane with nearly symmetric tails of the distribution above $(0^{\circ} - 90^{\circ})$ and below $(90^{\circ} - 180^{\circ})$ the reaction plane. There is not a clear dependence on system asymmetry at this juncture; only that the two $Z = 54$ systems have a broader peak centered in the plane with the $Z = 50$ system having a slightly narrower peak. The dip near $\Psi_{out} = 90^{\circ}$ is not an acceptance issue but appears to be due to secondary decay effects as is described by the statistical cooling of CoMD simulations with GEMINI; both of which will be discussed in greater detail in Section 5.4. As before, we define the system asymmetry, δ_{sys}, as

$$\delta_{sys} = \frac{N_{sys} - Z_{sys}}{A_{sys}} \tag{5.9}$$

where $N_{sys}, Z_{sys},$ and A_{sys} are the neutron, proton, and mass values of the aggregate system.

In the case of the Φ_{in} angular distribution spectra, there are also some interesting features. The two $Z = 54$ systems trend well together. The $Z = 50$ system has a slightly higher preference for an alignment of the PLF in the backward direction

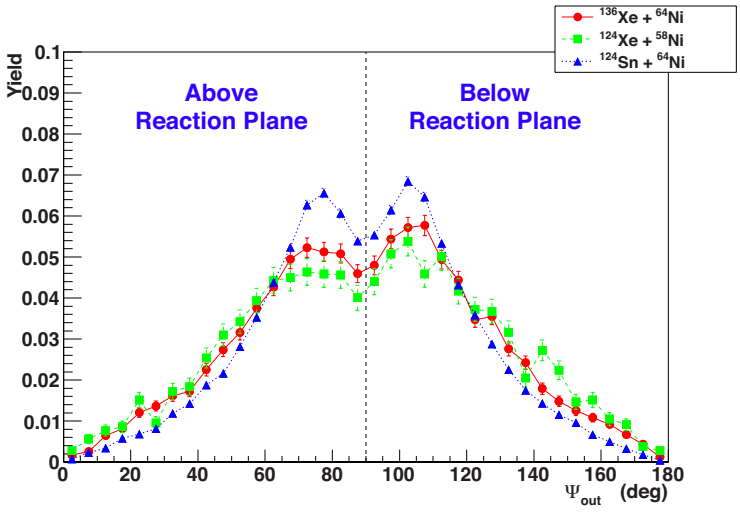

(a) Ψ_{out} systematic angular distributions

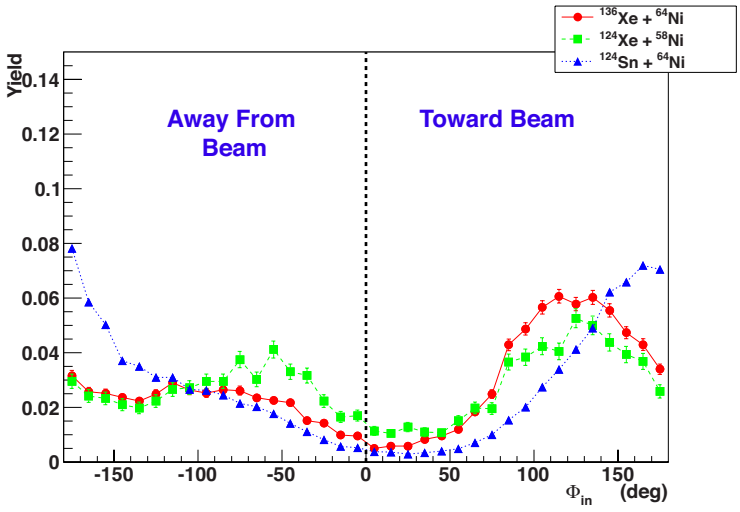

(b) Φ_{in} systematic angular distributions

Figure 5.6: Angular distributions of Ψ_{out} and Φ_{in} shown system-by-system. The red(solid) line, green(dashed), and blue(dotted) lines represent the ^{136}Xe+^{64}Ni, ^{124}Xe+^{58}Ni, and ^{124}Sn+^{64}Ni systems respectively.

(opposite of $\vec{v}_{QP}$ along $\vec{n}_{sep}$). This is in contrast to the two $Z = 54$ systems who have a nearly flat distribution in the "Away From Beam" direction (Figure 5.6b) with a peak in alignment near $\Phi_{in} = 110°$ in the direction toward the beam with respect to $\vec{n}_{sep}$. All three systems show a preferential detection of the IMF being

emitted forward in the QP frame of reference, preferentially in the direction of the beam. It is not clear from either spectra in Figure 5.6 as to which contributions are dynamical and which are statistical.

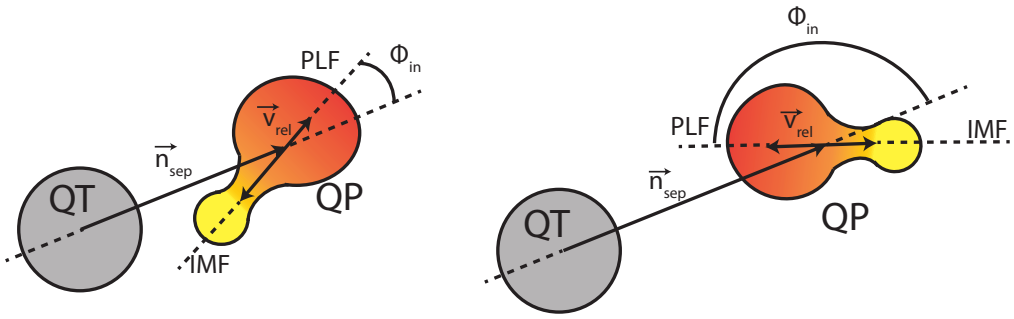

(a) QP rotation a shorter time after QP-QT separation

(b) QP rotation a longer time after QP-QT separation

Figure 5.7: 2D Projection of the QP-QT separation. The QT is described by the gray sphere on the left. The QP is described as the colored, deformed shape on the right. The QP, after some time, may then decay into a PLF and IMF. This is directly correlated to the degree of rotation[70, 130, 131] described by the in-plane angle Φ_{in} (in this case). The QP rotation can be visualized on short (a) and long (b) time scales using this cartoon representation.

The breaking of the QP with the IMF emitted forward (PLF aligned in the backward direction near $\Phi_{in} = 110°$) is indicative of a QP that breaks sequentially, on longer time scales with a high degree of rotation[70, 130, 131]. This can be explained more simply by the 2D, in-plane projection of the QP-QT separation shown in Figure 5.7. In Figure 5.7, the QP is shown as the colored, deformed fragment on the right that is breaking into a PLF and IMF, and the QT is shown as the gray sphere on left. The QP and QT are shown separating from each other. After the QP and QT separate, the deformed QP may break into two large ($Z \geq 3$) fragments (indicated by PLF and IMF). However, the angle of emission relative to the QP-QT

separation axis ($\vec{n}_{sep}$), is dependent on the degree of rotation of the deformed QP has undergone by the the time the QP breaks into the PLF and IMF. So, the emission of the IMF in the forward direction (away from the QT) is indicative of a QP that has rotated significantly before breaking. This can be seen in Figure 5.7b. This implies a longer time after QP-QT separation to allow for a larger degree of rotation. This is in contrast to an IMF that is emitted in the backward direction (toward the neck) where the QP breaks promptly. A prompt breaking of the QP, with the IMF being emitted toward the neck and PLF aligned strongly in the direction of $\vec{v}_{QP}$, indicates a lower degree of rotation as seen in Figure 5.7a.

A deeper analysis of the angular distributions will be discussed in Section 5.4. This discussion will include the statistical decay contributions that produce the dips at $\Psi_{out} = 90^{\circ}$ and $\Phi_{out} = 0^{\circ}$ in the out-of and in-plane distributions respectively. Additionally, a direct comparison to dynamical simulations will also be discussed.

5.2.2 QP Cuts

In order to explore the underlying trends focused around the reaction plane distributions, the distributions have been divided up by QP mass and energy, A_{QP} and E_{QP} respectively. For this analysis, the E_{QP} and A_{QP} have been divided as tabulated in Table 5.1 and visualized in Figure 5.8 . The cuts were applied this way to each system based on natural breaks in the spectra. The mass and energy of the QP are defined by

$$A_{QP} = A_{PLF} + A_{IMF} \tag{5.10}$$

and

$$E_{QP} = E_{PLF} + E_{IMF} \tag{5.11}$$

respectively. E_{QP} is the sum of the lab frame PLF and IMF kinetic energy. It has been shown to be a good, qualitative indication of the collision violence shown by De Filippo and Russotto et al. [50, 63] and described in transport models by Baran et al. [44].

Table 5.1: QP mass and energy cuts (A_{QP} and E_{QP})

Cut Name	Cut 1	Cut 2	Cut 3
A_{QP}	60-135 A	135-160 A	160+ A
E_{QP}	600-1200 MeV	1200-1500 MeV	1500+ MeV

Figure 5.8 shows the reconstructed QP mass and energy spectra with cuts overlaid. In Figure 5.8a, a mass spectrum of A_{QP} is shown with cuts overlaid as shown in the yellow, purple and gray regions. The highlighted regions represent the low, mid and high A_{QP} cuts respectively. The E_{QP} cuts, as shown in Figure 5.8b, detail the cuts placed on the energy of the reconstructed QPs in the regions highlighted in blue, green and red for the low, medium and high energy cuts respectively. The spectra shown for both the reconstructed QP mass and energy, in Figure 5.8, are from the ^{136}Xe +^{64} Ni system. However, all three cut regions (colored overlays) are applied the same to all reaction systems as shown in Figure 5.8 (and as Tabulated in Table 5.1). In this way, the reconstructed QPs are treated the same regardless of the system to system variances.

5.3 Quasi-Projectile Break-up Correlations

The reaction plane observables and the QP cuts as described in Section 5.2 will be used in the analysis of angular, velocity, and mass correlations in the subsequent

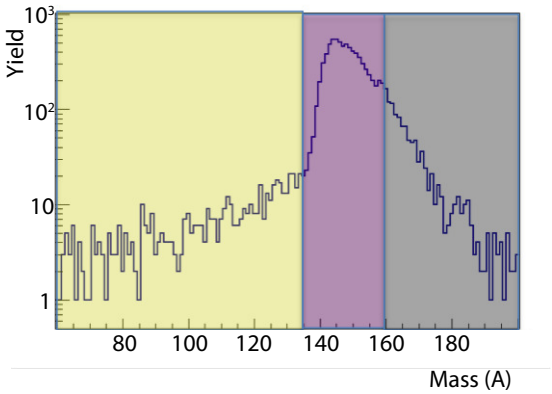

(a) A_{QP} cuts. Low, medium. and high A_{QP} cuts are as tabulated in Table 5.1. The cuts are graphically shown in the yellow, purple, and gray shaded areas respectively. The

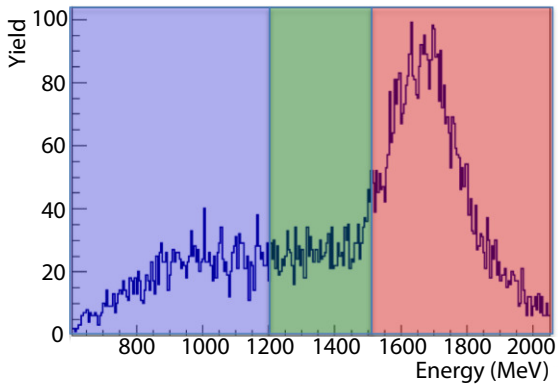

(b) E_{QP} cuts. Low. medium. and high E_{QP} cuts are as tabulated in Table 5.1. These cuts are graphically shown in the blue, green, and red shaded areas respectively.

Figure 5.8: A_{QP} and E_{QP} cuts. The ^{136}Xe+^{64}Ni system is shown for demonstration purposes. All reaction systems have the same reconstructed QP cuts applied as tabulated in Table 5.1.

subsections of this chapter.

5.3.1 Angular Correlations

One (of many) ways the angular distributions Ψ_{out} and Φ_{in}, as previously shown in Figure 5.6, can be disentangled is via the E_{QP} and A_{QP} cuts described above in Section 5.2.2. Using these cuts, the QP energy and mass contribution to the Ψ_{out}

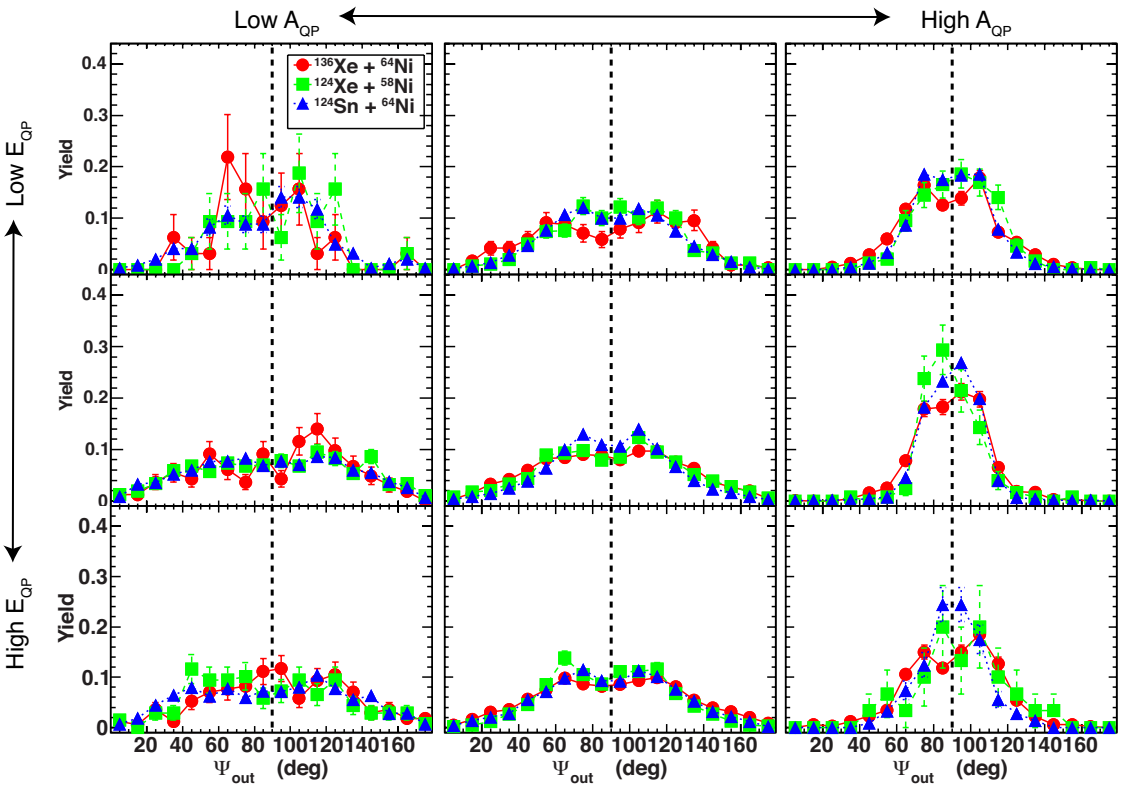

Figure 5.9: Ψ_{out} distribution as a function of A_{QP} and E_{QP} cuts applied. A_{QP} increases from left to right. E_{QP} increases from Top to Bottom. Cuts are as tabulated in Table 5.1. Each system is shown, with error bars, as per the legend.

and Φ_{in} distributions can be disentangled. We will show how the E_{QP} and A_{QP} can be used as a possible surrogate to impact parameter and time, as well as event selection for better examination of the underlying physics.

Looking at the Ψ_{out} distributions as a function of A_{QP} and E_{QP}, in Figure 5.9, there appears to be a large dependence on the mass of the QP. As the mass of the QP gets smaller, the distribution, with respect to deflection out of the reaction plane, becomes more isotropic. Although the distribution is still centered around $\Psi_{out} = 90°$, the distribution becomes broader with less structure. This isotropy would be indicative of a sequential breaking for the lower mass QPs on a longer time

scale. There is also a small trend of decreased anisotropy in Ψ_{out} as the energy of the QP increases. So, as the QP energy increases, the hot QP breaks or emits the IMF more isotropically. The higher mass, more damped QPs likely resulted from a mid-peripheral collisions resulting in a heavier QP that was more aligned with the QP-QT separation when it decayed. This would also be indicative of a QP that rotated for a short time after QP-QT separation before breaking into a PLF and IMF. The progression to higher E_{QP} (less damped collisions) and lower A_{QP} likely resulted from a more peripheral collision producing a more projectile-like QP. The out-of-plane distribution is indicative of QPs that have a larger range of rotation and thus a longer time until breaking into the PLF and IMF pair.

Equally as interesting, the Φ_{in} distribution as a function of A_{QP} and E_{QP} can be seen in Figure 5.10. The in-plane angular distribution shows a dependence on A_{QP} such that as the mass of the QP decreases (from right to left), there is a shift in the angular alignment of the QP break-up. So for heavy, damped QPs, the breakup is aligned near the QP-QT separation axis ($\Psi_{in} = 0$) and deflected slightly away from the initial beam (projectile) velocity. As A_{QP} decreases, the break-up is deflected farther away from the beam axis until it appears to "wrap-around" and become more aligned with the beam axis. This is also true for heavy QPs with increasing E_{QP} (less damped). "Wrapping-around" refers to the transition from the "Away From Beam" direction, across the $\pm 180^{\circ}$ line (Figure 5.5), and then more toward being aligned with the beam in the "Toward Beam" direction with respect to $\vec{n}_{sep}$ as previously described in Figure 5.6. It is possible to imagine that as the mass decreases there is more of a tendency to "spin" around (or "tumble" end-over-end if deformed) with the QP separating into the PLF/IMF pair. In this particular scenario, the PLF may separate away from the beam due to higher degrees of angular momentum, possibly linked to more peripheral impact parameters.

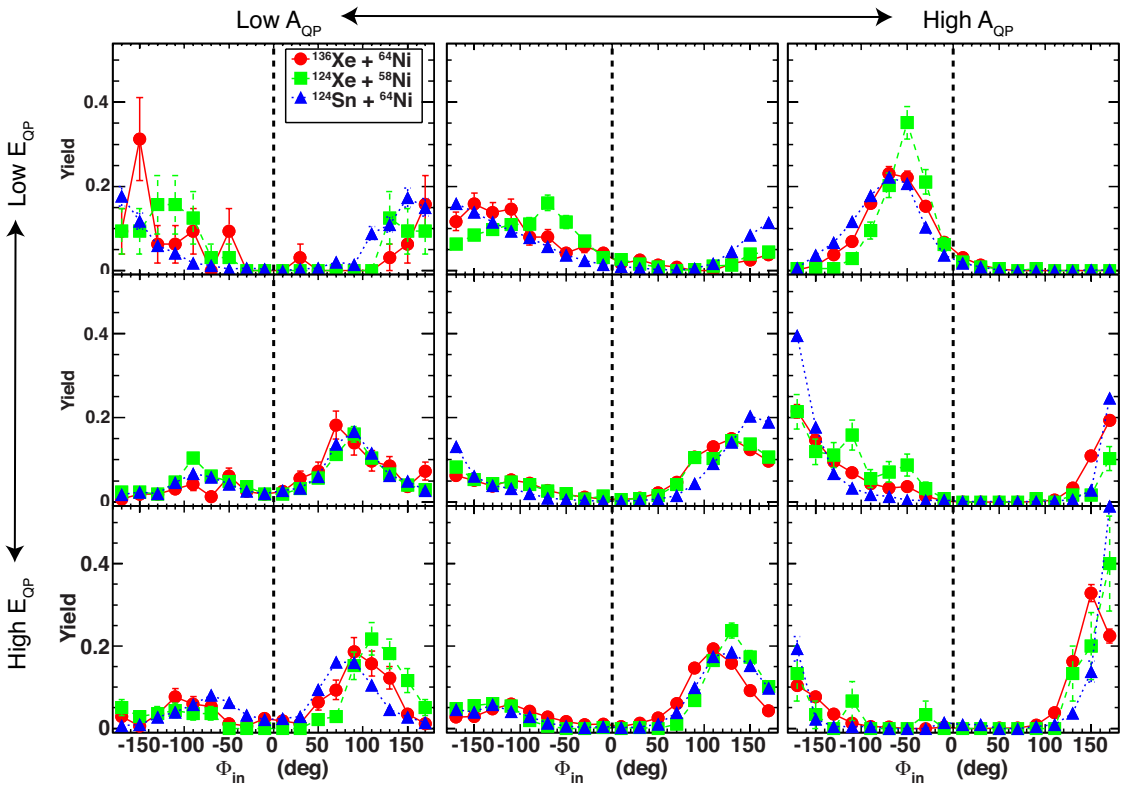

Figure 5.10: Φ_{in} distribution as a function of A_{QP} and E_{QP} cuts applied. A_{QP} increases from left to right. E_{QP} increases from Top to Bottom. Cuts are as tabulated in Table 5.1. Each system is shown, with error bars, as per the legend.

So, continuing with the analogy, as the mass of the QP decreases step-wise, it appears that the PLF velocity is deflected farther away from beam until is crosses over $\pm 180°$ and begins to be aligned more toward the beam. It is possible to imagine the case where as A_{QP} decreases to become more representative of a mass similar to the original projectile. This would be the case in a more peripheral collision. As such, the amount of angular momentum would increase, leading to a lighter QP tumbling before breakup.

We can visualize this phenomena through indirect comparison to SMF model calculations as shown in Figure 5.11. In the case of a lighter QP at more peripheral

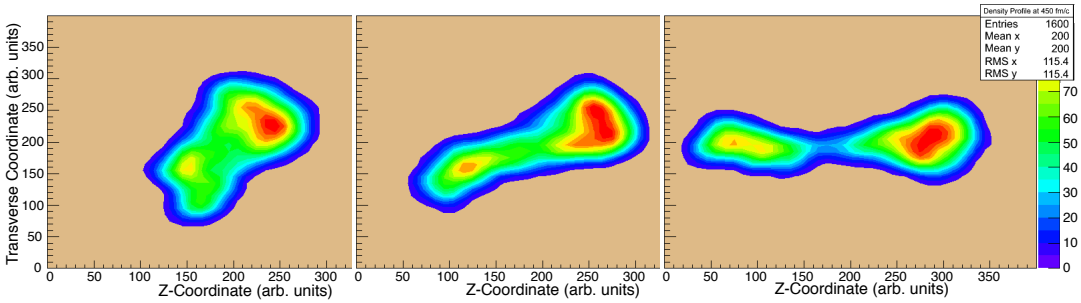

(a) t = 200 fm/c. (b) t = 300 fm/c. (c) at t = 450 fm/c.

Figure 5.11: A series of SMF model density contour plots representative of a ^{124}Sn + ^{64}Ni collision at an impact parameter of b = 8 fm. The frames are stopped at a time of t = 200 fm/c (a), t = 300 fm/c (b), and t = 450 fm/c (c). The QP (larger of the two nuclei, on the right) can be seen separating from the QT (grey, on left) and then rotating as a function of time.

impact parameters, Figure 5.11 is representative of a ^{124}Sn projectile on a ^{64}Ni target collision at an impact parameter of b = 8 fm. Figures 5.11a - 5.11c show the nucleon density contour for the reaction system. The figures are snap-shots in time such that we observe the evolution of the system at times t = 200, 300, and 450 fm/c respectively. The QP (larger of the two nuclei, on the right) can be seen separating from the QT with close to what would be the initial projectile mass at t = 200 fm/c. The QP is slightly deformed and through time-dependent analysis can be seen as rotating in 2D-coordinate space. By focusing on the highest nucleon density in the QP (red contours), the QP can be observed rotating significantly. This has been predicted to possibly result in a break-up[25, 45, 11, 44, 48, 41, 47] of the QP into a PLF and IMF.

For the case of a heavier QP near mid-peripheral impact parameters ($b = 5 - 6$ fm), Figure 5.12 represents a ^{124}Sn projectile on a ^{64}Ni target at an impact parameter of b = 6 fm. Figures 5.12a - 5.12c show the nucleon density contour for the reaction system. The figures are snap-shots in time such that we observe the evolution of

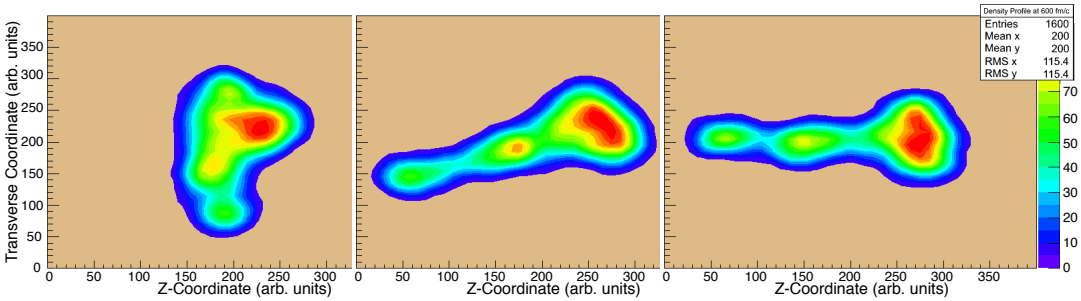

(a) t = 200 fm/c. (b) t = 450 fm/c. (c) t = 600 fm/c.

Figure 5.12: A series of SMF model density contour plots representative of a ^{124}Sn + ^{64}Ni collision at an impact parameter of b = 6 fm. The frames are stopped at a time of t = 200 fm/c (a), t = 450 fm/c (b), and t = 600 fm/c (c). The QP (moving from left to right) can be seen separating from the QT. The QP is predicted to break-up[25, 45, 11, 44, 48, 41, 47] into a PLF and IMF. Z-Coordinate is parallel to the beam axis. The Transverse Coordinate represents the plane transverse the the beam direction.

the system at times t = 200, 450, and 600 fm/c respectively. The QP can be seen separating from the QT (far left) with an elongated neck bridging between the PLF, IMF and QT. The mostly spherical PLF can be seen traveling close to the separation axis, $\vec{n}_{sep}$ with a high probability of the IMF being emitted backward of the PLF toward the neck region. The QP is more massive (encompassing the IMF and PLF) than a comparable QP at a larger impact parameters (Figure 5.11) and the initial projectile.

5.3.2 *Velocity Correlations*

Another method of analyzing angular correlations is to look at the relative velocity between the PLF and IMF ($\vec{v}_{rel}$) with respect to the velocity of the QP ($\vec{v}_{QP}$). In this way, it is possible to look at the cosine of the angle between the two velocity vectors, $cos(\theta_{prox})$[57, 65, 66, 67, 68, 69, 70, 132, 133, 134]. This quantity has been shown to be directly correlated to QP rotation and time-to-breakup after QP-QT separation[70, 130, 131]. The $cos(\theta_{prox})$ value is also a convolution of the in- and out-of-plane angles, Ψ_{in} and Φ_{out} respectively, in that it accounts for the 3-dimensional angle of the PLF (IMF) relative to the QP-QT separation axis ($\vec{n}_{sep}$). Specifically, it is possible to reconstruct the angle via

$$cos(\theta_{prox}) = \frac{\vec{v}_{QP} \cdot \vec{v}_{rel}}{v_{QP} * v_{rel}} \tag{5.12}$$

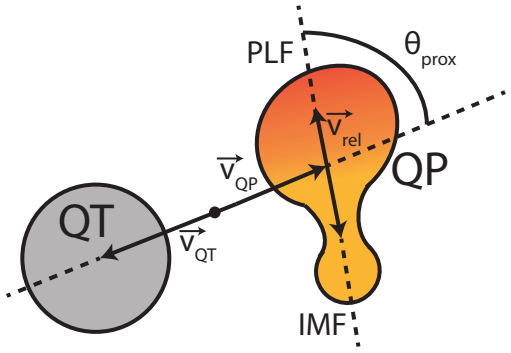

Figure 5.13: A cartoon depiction of what has been termed θ_{prox} or the angle between the PLF-IMF relative velocity and the QP velocity as per Eq. 5.12. The value of θ_{prox} accounts for the 3-dimensional angle of the PLF (IMF) relative to the QP-QT separation axis.

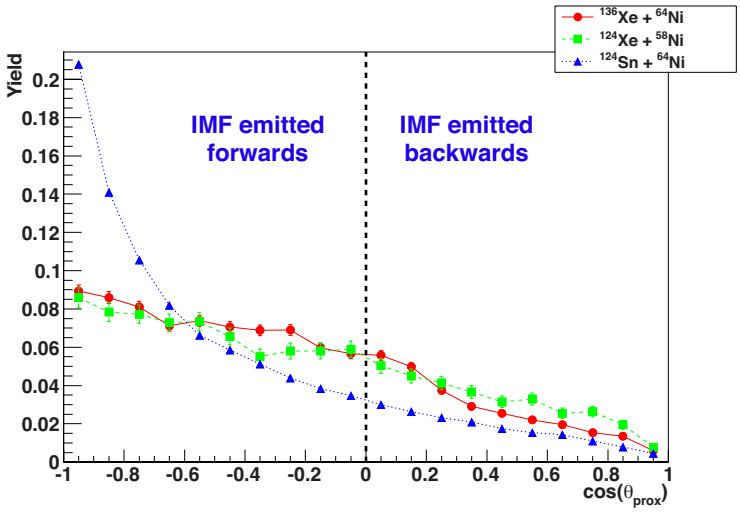

Figure 5.14: Distributions of $cos(\theta_{prox})$ system-by-system. Negative $cos(\theta_{prox})$ values correspond to a forward emission of the IMF and positive values correspond to a backward emission of the IMF from the QP. The red(solid) line, green(dashed), and blue(dotted) lines represent the systems ^{136}Xe+^{64}Ni, ^{124}Xe+^{58}Ni, and ^{124}Sn+^{64}Ni respectively.

as described by De Souza and collaborators[57, 65, 66, 67, 68, 69, 70, 132, 133, 134].

Examining the $cos(\theta_{prox})$ yields interesting information as to the alignment of the QP break-up. Specifically, $cos(\theta_{prox})$ yields information as to whether the IMF is emitted forward or backward of the PLF in the QP reference frame as depicted in Figure 5.13. The $cos(\theta_{prox})$ distributions from each system are shown in Figure 5.14. The data in this experiment trends toward the preferential forward emission of the IMF. This appears to be a similar trend noticed by Hudan[65] et al. and Henry[77] et al. at similar system energies and masses. The large backward-forward asymmetry in the distributions has been proposed previously[57, 67, 132, 133] to be a signature of dynamical fissioning of the emitting source and typically characterized by highly aligned decay. There does not appear to be a dependence of the $cos(\theta_{prox})$ on the system asymmetry, δ_{sys}. There does appear to be a dependence on the system Z (note

the case of ^{124}Sn+^{64}Ni). Figure 5.14 does show that there is preferential detection of the IMF being emitted in forward of the PLF in the QP frame of reference. This is true for all three systems with the $Z = 50$ system having a large peak at $cos(\theta_{prox}) = -1$ indicating an IMF emitted forward of the PLF aligned along the QP-QT separation axis. The two $Z = 54$ systems show a near isotropic distribution for $-1 \leq cos(\theta_{prox}) \leq 0$ and then dropping off above $cos(\theta_{prox}) \geq 0$.

However, the A_{QP} and E_{QP} cuts can be applied, as has been done previously in this section, in an attempt to gain more insight into the components contributing to the system wide distribution. In Figure 5.15, there is a similar trend as before in that there is a dependence on both A_{QP} and E_{QP}. Specifically, as the mass of the QP decreases and energy of the QP increases, the probability of a forward IMF emission increases. Once the A_{QP} reaches the lightest cut of QPs (Cut 1) and E_{QP} reaches the most energetic QP cut (Cut 3), the distributions generally become more isotropic in nature. These cuts also normalize the distributions more between the three systems. Especially in the case of the large peak at $cos(\theta_{prox}) = -1$ for ^{124}Sn+^{64}Ni, where it can be seen that the largest contribution to the peak is originating from the most energetic and heaviest QPs (bottom, right panel). Additionally, the $cos(\theta_{prox})$ is directly correlated to the QP rotation and thus the time to QP breakup after separating from the QT. The IMFs emitted backward, corresponding to a $cos(\theta_{prox}) > 0$, are indicative of a small rotation of the QP. This smaller rotation corresponds directly to a short time from QP-QT separation to QP breakup into a PLF and IMF pair[70, 130, 131]. Conversely, $cos(\theta_{prox}) < 0$ indicates a longer time between QP-QT separation and QP decay, thus a larger degree of rotation is possible. In Figure 5.15, we can see that the heaviest, least energetic QPs exhibit small rotations and short lifetimes corresponding to dynamical IMF emission close to the neck region. Lower mass, higher energy QPs show a higher degree of rotation, indicative of a more

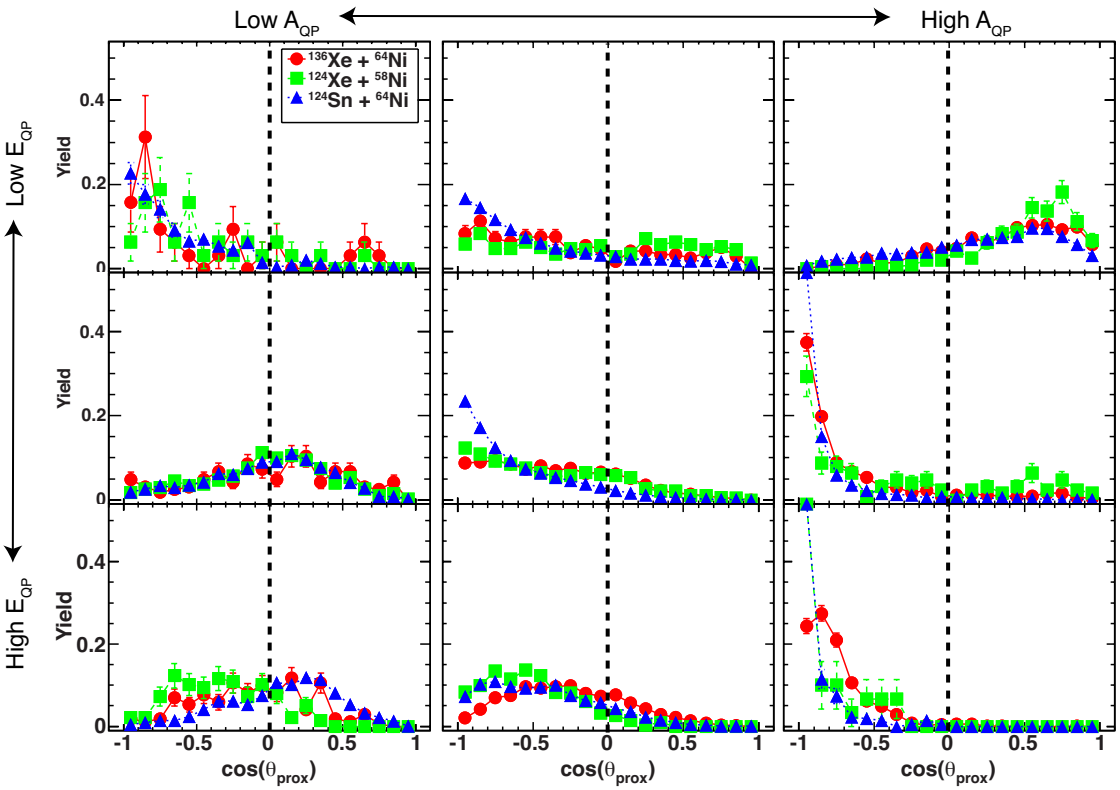

Figure 5.15: Distributions of $cos(\theta_{prox})$ as a function of A_{QP} and E_{QP} cuts applied. A_{QP} increases from left to right. E_{QP} increases from Top to Bottom. Cuts are as tabulated in Table 5.1. Each system is shown, with error bars, as per the legend. Distributions where $cos(\theta_{prox}) \geq 0$ represent QPs with a short rotation time before breakup.

semi-peripheral collision, with a wide range of IMF emission angles.

5.3.3 IMF Mass Correlations

Mass partitioning of the QP into the IMF and PLF is also predicted to be sensitive to the symmetry energy and dynamical processes in the Fermi energy domain[11, 44]. Particularly, the distribution of the emitted IMF mass is predicted to be sensitive. We have analyzed the A_{IMF} distributions as a function of the QP mass and energy. In Figure 5.16, the mass of the IMF emitted from the QP has been plotted as a function of A_{QP} and E_{QP} (as done in previous sections). There is a dependence on

A_{QP} and E_{QP} as expected. As A_{QP} decreases, the peak value of A_{IMF} decreases as well. This is expected as lighter QPs have fewer nucleons to emit.

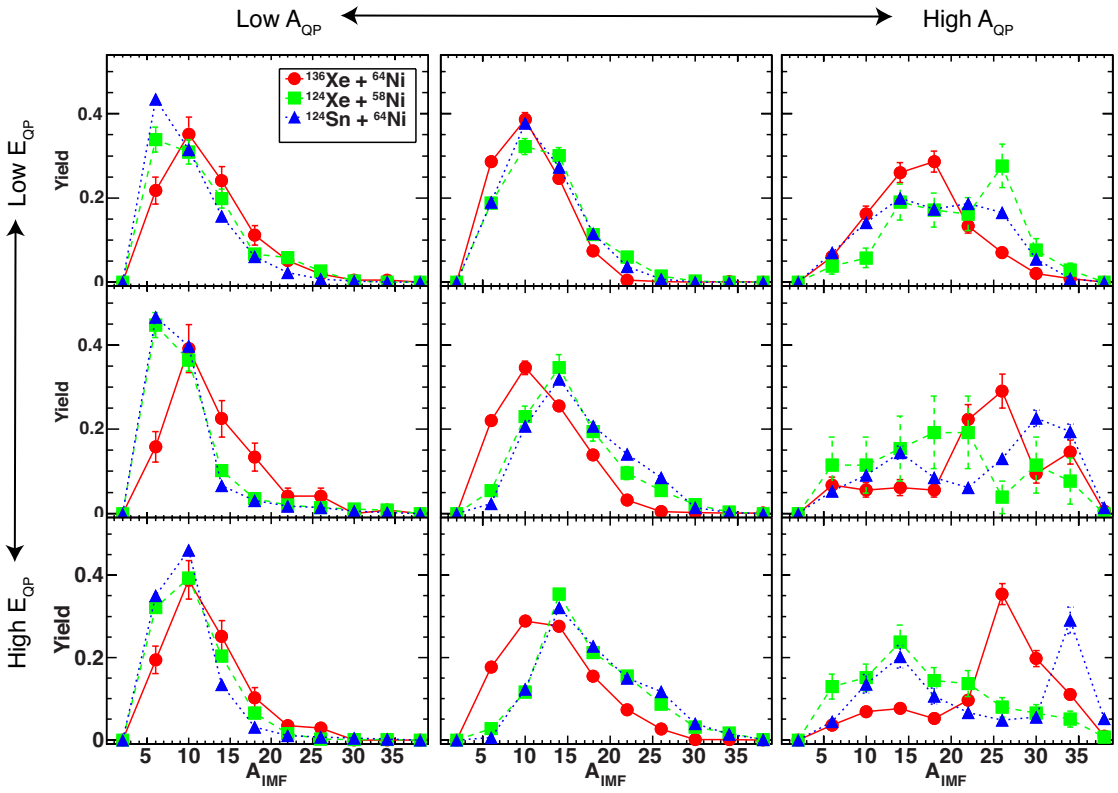

Figure 5.16: Distributions of the mass of the emitted IMF (A_{IMF}) as a function of A_{QP} and E_{QP} cuts applied. A_{QP} increases from left to right. E_{QP} increases from Top to Bottom. Cuts are as tabulated in Table 5.1. Each system is shown, with error bars, as per the legend.

As the E_{QP} increases, there is a broadening of the distribution and an increase in the peak A_{IMF} value in some cases. This would be expected as the phase space increases with an increase in energy allowing for heavier (and wider range of) IMFs to be emitted. For the heaviest QPs, as E_{QP} increases, the A_{IMF} increases as well. This suggests that as E_{QP} increases for a given A_{QP}, the QP breaks into a lighter

PLF. These more energetic QPs retain some memory of the entrance channel mass and break into a PLF with A_{PLF} close to A_{beam}. The more massive, lower energy QPs typically emit a light IMF as the QP decays to a less excited state as compared to a QP of similar A_{QP} at higher E_{QP}. This is the indication of a heavier, compound system decaying by light IMF emission. Overall, these trends suggest the mass partitioning is dependent on the violence of the collision.

5.4 Comparison to Simulations

It is important to look at the experimental data collected with respect to dynamical models. The dynamical models allow us to better probe the underlying physics. The dynamical models, focusing on the results from CoMD, can provide some insight into the influence of the symmetry energy, in addition to the dynamical breakup of the system. In this case, we are are interested in the 2-body breaking of QP and how the symmetry energy influences this break-up.

For direct comparison of dynamical simulations to experimental data, CoMD events were filtered by the FAUST filter and then analyzed in the same way as the experimental data. The CoMD was analyzed for each of the three systems and three permutations of the parameterization of the symmetry energy for each system, respectively. The experimental data was compared to both the hot output of CoMD (t = 3000 fm/c) as well as the cooled output after de-exciting with GEMINI[83, 84, 85] to account for secondary decay effects. The hot CoMD stopped at t = 3000 fm/c has, on average, $\sim$150 MeV ($\sim$0.75MeV/nucleon) of residual excitation energy for the system. There are several interesting features present when comparing both the hot and cooled CoMD simulations to the experimental data. In this section, the reaction plane observables were examined while also exploring the effects of secondary decay and the possible influence of the symmetry energy on the observation a 3-body

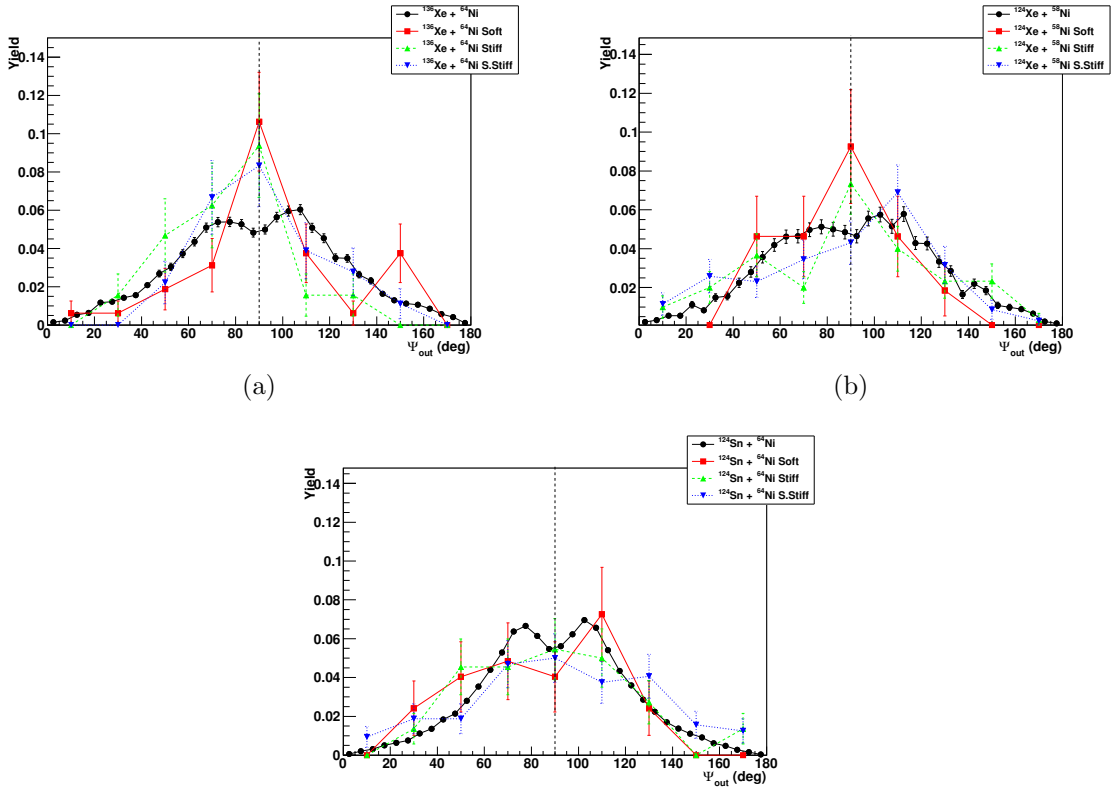

Figure 5.17: Comparison of experimental and CoMD Ψ_{out} Angular Distributions for ^{136}Xe+^{64}Ni (a), ^{124}Xe+^{58}Ni (b), ^{124}Sn+^{64}Ni (c) PLFs. Experimental data is shown in black (circles, solid line) with filtered CoMD results for the soft, stiff, and super-stiff case shown in red (circles, solid line), green (triangles, dashed line) and blue (upside-down triangle, dotted line) respectively.

breakup of the system.

In Figure 5.17, the Ψ_{out} distribution for each system is plotted separately with respect to the results of CoMD by symmetry energy. Each experimental system is plotted with the overlaid results from "hot" CoMD (t = 3000 fm/c) for each of the respective systems. The experimental data is plotted in black (circles, solid line) with the soft, stiff and super-stiff parameterizations of the symmetry energy plotted in red (squares, solid line), green (triangles, dashed line) and blue (upside-down

triangle, dotted line) respectively. The parameterizations of the symmetry energy have previously described in Section 1.1. A broad peak can be seen in the Ψ_{out} angular distribution, centered in the reaction plane ($\Psi_{out} = 90°$) for both the CoMD and experimental data. The results from CoMD agree as to the general shape of the distribution. Two features of note are that the hot CoMD does not reproduce the dip near $\Psi_{out} = 90°$ and there are not enough statistics for the 3-body breakup from the hot CoMD results to draw a clear conclusion as to the effect of the symmetry energy on the experimental results.

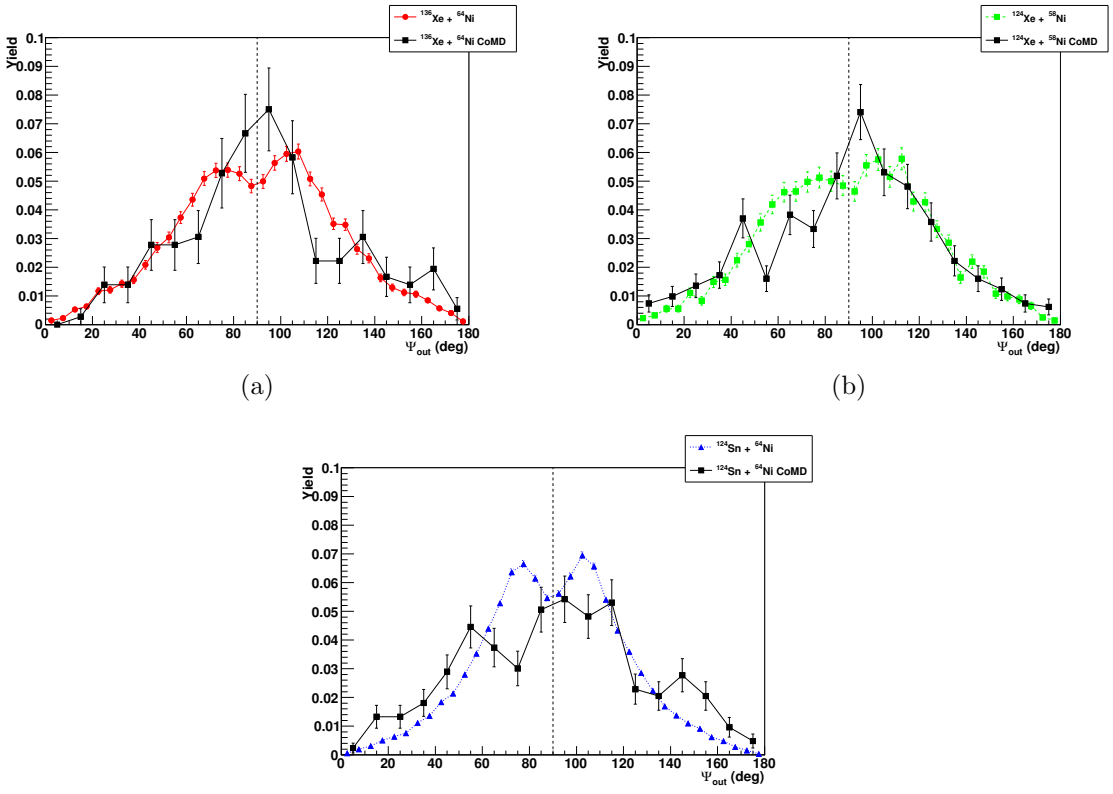

(a) (b)

(c)

Figure 5.18: Comparison of experimental and total CoMD Ψ_{out} Angular Distributions for ^{136}Xe+^{64}Ni, ^{124}Xe+^{58}Ni, ^{124}Sn+^{64}Ni PLFs. The total CoMD is the result of summing the CoMD events together from all three symmetry energy parameterizations. Experimental data is shown in black (circles, solid line).

The combined CoMD results for each system are plotted in Figure 5.18 in black squares with each experimental system plotted in color where ^{136}Xe+^{64}Ni, ^{124}Xe+^{58}Ni, and ^{124}Sn+^{64}Ni are plotted via red circles (solid line), green triangles (dashed line), and blue squares (dotted line) respectively. If we combine the three parameterizations of symmetry energy in order examine just the dynamical output of CoMD with higher statistics, system-by-system, we can see it is more clear that the experimental data and the hot CoMD simulations trend well and appear remarkably similar and with smaller error bars. There are certainly fluctuations in the CoMD data, but within error bars, the data trends well. However, the decrease in intensity centered at $\Psi_{out} = 90^{\circ}$ in the experimental data is still not reproduced. The hot CoMD distributions are generally the correct shape however, with some large fluctuations due to low statistics after the FAUST software filter.

In an attempt to explain why a decrease centered at $\Psi_{out} = 90^{\circ}$ in the experimental data exists, corresponding to PLF being aligned in the reaction plane, the CoMD was de-excited with GEMINI. When the reaction system is de-excited via GEMINI, we can see the general shape of the distribution from CoMD more closely agrees with the experimental data as shown in Figure 5.19. This can be seen in how the cooled CoMD now reproduces the decrease in intensity centered at $\Psi_{out} = 90^{\circ}$ and many of the fluctuations are now smoothed with respect to Figure 5.18. However, the cooling with GEMINI has now added a new feature in that the simulated results have a slightly wider dip in intensity centered at $\Psi_{out} = 90^{\circ}$ but, overall the distribution is better explained. Unfortunately, the cooling of the CoMD results via GEMINI does not yield any significant information about the symmetry energy effects (Figure 5.19). However, the CoMD+GEMINI sufficiently describes the dip in yield at $\Psi_{out} = 90^{\circ}$ resulting from the secondary decay of the hot QP.

In the case of Φ_{in}, there are a number of features present not fully explained by

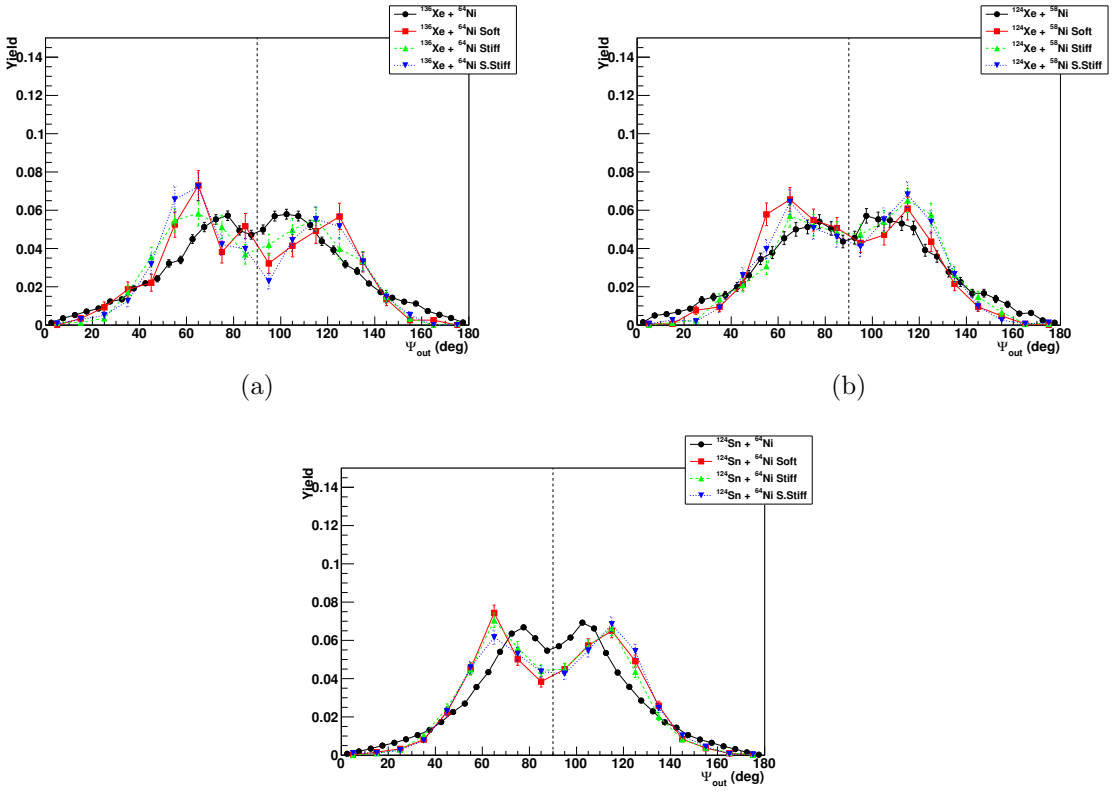

Figure 5.19: Comparison of experimental and cooled CoMD Ψ_{out} Angular Distributions for ^{136}Xe+^{64}Ni (a), ^{124}Xe+^{58}Ni (b), ^{124}Sn+^{64}Ni (c) PLFs. The cooled CoMD is the result of CoMD simulations cooled with GEMINI[83, 84, 85]. Experimental data are shown in black (circles, solid line) with filtered CoMD results for the soft, stiff, and super-stiff case shown in red (circles, solid line), green (triangles, dashed line) and blue (upside-down triangle, dotted line) respectively.

hot CoMD, and are better explained by cooled CoMD (CoMD+GEMINI), similar to what was observed in the case of Ψ_{out}. Particularly, the dip near $\Phi_{in} = 0°$ and the peak near $\Phi_{in} = 110°$ are clearly shown to be indicative of secondary decay of the QP. As was the case in the examination of the Ψ_{out} distributions, hot CoMD statistics were too low to make a clear judgement as to the influence of the symmetry energy directly to the experimental data combined with the hot CoMD poorly describing the in-plane angular distributions.

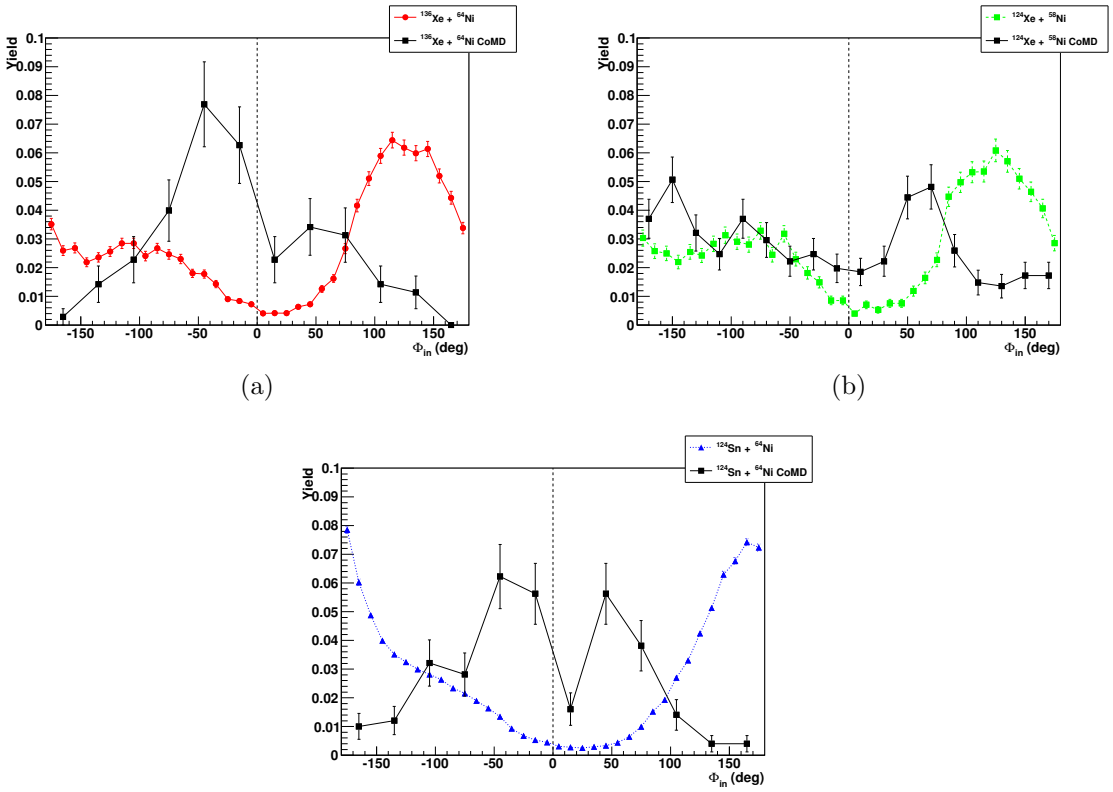

Figure 5.20: Comparison of experimental and total CoMD Φ_{in} Angular Distributions for ^{136}Xe+^{64}Ni (a), ^{124}Xe+^{58}Ni (b), ^{124}Sn+^{64}Ni (c) PLFs. The total CoMD is the result of summing the CoMD events together from all three symmetry energy parameterizations. CoMD data is shown in black (circles, solid line) with experimental results for the ^{136}Xe+^{64}Ni, ^{124}Xe+^{58}Ni, ^{124}Sn+^{64}Ni shown in red (circles, solid line), green (triangles, dashed line) and blue (upside-down triangle, dotted line) respectively.

In an attempt to get a better understanding of the dynamical distributions and contributions of the hot PLF, we can, again, combine the three parameterizations of the symmetry energy from within CoMD. In Figure 5.20, it can be clearly seen that the hot CoMD and the experimental data are not in good agreement. These combined CoMD results for each system are plotted in black squares with each experimental system plotted in colored circles. The colors for each system match the colors plotted

in Figures 5.6 and 5.14 where ^{136}Xe+^{64}Ni, ^{124}Xe+^{58}Ni, and ^{124}Sn+^{64}Ni are plotted via red (solid) line, green (dashed), and blue (dotted) lines respectively. For each of the three systems, the common feature is the irreproducibility of the experimentally observed peak near $\Phi_{in} = 100 - 180^{\circ}$ via CoMD. In all three cases, it appears as though the peak in the hot CoMD data is shifted toward the beam, near $\Phi_{in} = 50^{\circ}$. However, because the error bars are so large due to statistical fluctuations, a certain determination can not be made solely from the available statistics in the hot CoMD simulations. The individual parameterizations of the symmetry energy for the hot CoMD in Φ_{in} are not shown, as they are similar in statistics to the Ψ_{out} distributions as shown previously in Figure 5.17.

However, we can examine the effect of cooling CoMD with GEMINI on the Φ_{in} distribution. The GEMINI-cooled CoMD appears to shift the alignment of the PLF with respect to the QP-QT separation axis ($\vec{n}_{sep}$) away from the beam due to secondary decay effects as shown in Figure 5.21. In this way, the experimental data and the GEMINI-cooled CoMD are now in good agreement. The cooled CoMD reproduces the experimental data with reasonable accuracy especially in the case of the ^{124}Sn+^{64}Ni system. The two xenon systems have some disagreement as far as relative yield around the $\Phi_{in} = -180^{\circ}$ to -100° region. Overall there is much better agreement between experimental data and the cooled CoMD than with the hot CoMD. This suggests that the secondary decay of the hot PLF by particle emission deflects the PLF preferentially away from the beam-axis relative to the QP-QT separation axis. This reinforces the observation that the dip at $\Phi_{in} = 0^{\circ}$ is due to the secondary decay of the hot QP.

The examination of simulated and experimental $cos(\theta_{prox})$ data provides a complimentary picture of the processes involved with the evolution of the reaction system compared to the other observables mentioned thus far. We see that the experimen-

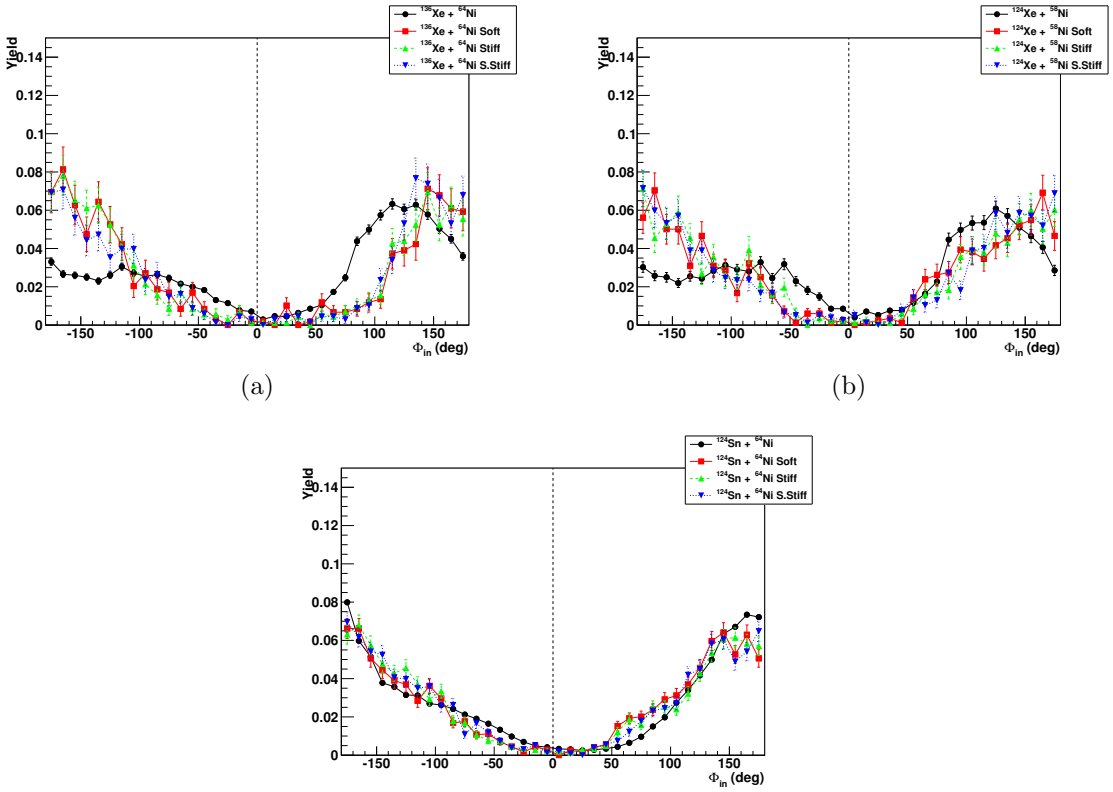

Figure 5.21: Comparison of experimental and cooled CoMD Φ_{in} Angular Distributions for ^{136}Xe+^{64}Ni (a), ^{124}Xe+^{58}Ni (b), ^{124}Sn+^{64}Ni (c) PLFs. The cooled CoMD is the result of CoMD simulations cooled with GEMINI[83, 84, 85]. Experimental data is shown in black (circles, solid line) with filtered CoMD results for the soft, stiff, and super-stiff case shown in red (circles, solid line), green (triangles, dashed line) and blue (upside-down triangle, dotted line) respectively. The dip at $\Phi_{in} = 0°$ is due to the secondary decay of the hot QP.

tal data is well described by secondary decay of the QP on longer time scales and matches well to simulations using CoMD+GEMINI. In Figure 5.22, we compare the results from hot CoMD events with respect to the experimental data. It can be seen that the dynamical emission of the IMF from the QP (in hot CoMD) is more peaked than that of the experimental data with the velocity of the IMF being less than that of the PLF in all three systems. This, relative to the velocity of the emitting QP in

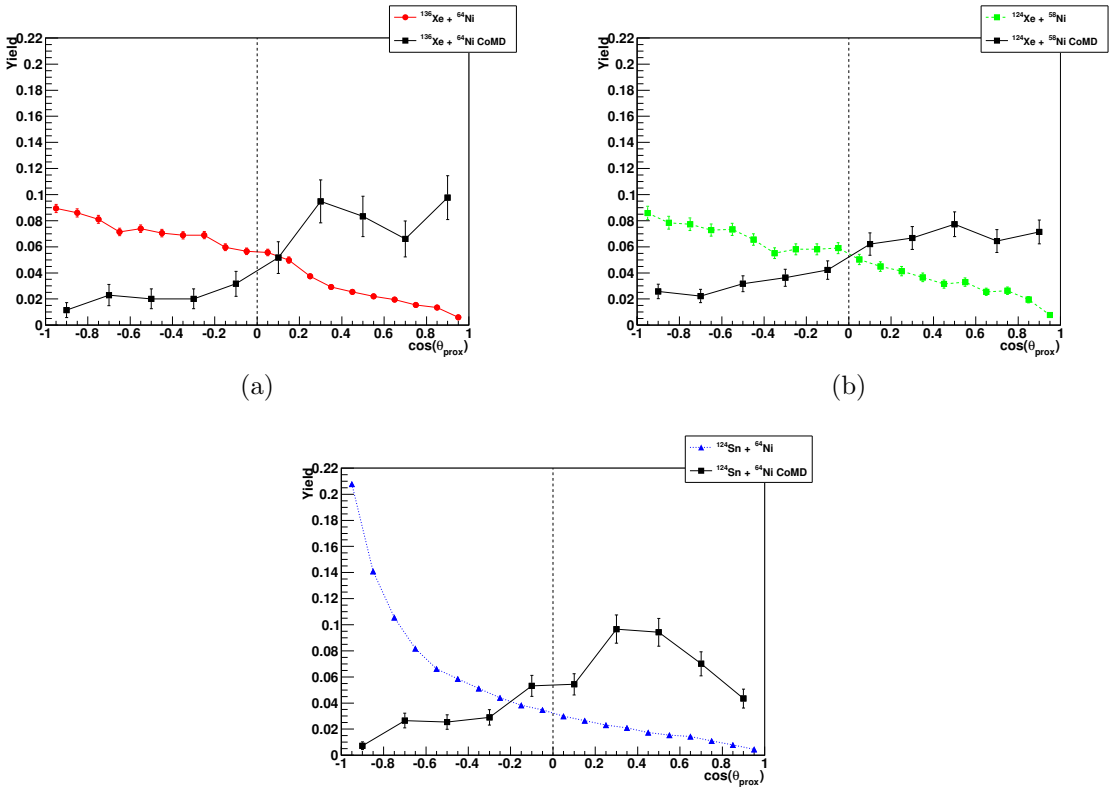

Figure 5.22: Comparison of experimental and total CoMD $cos(\theta_{prox})$ Angular Distributions for the ^{136}Xe+^{64}Ni (a), ^{124}Xe+^{58}Ni (b), and ^{124}Sn+^{64}Ni (c) IMFs. The total CoMD is the result of summing the CoMD events together from all three symmetry energy parameterizations. CoMD data is shown in black (circles, solid line) with experimental results for the ^{136}Xe+^{64}Ni, ^{124}Xe+^{58}Ni, ^{124}Sn+^{64}Ni shown in red (circles, solid line), green (triangles, dashed line) and blue (upside-down triangle, dotted line) respectively.

hot CoMD, suggests a more backward emitted IMF, typically thought of as an IMF emission toward the neck region ($cos(\theta_{prox}) > 0$) in a non-equillibrium emission. The hot CoMD, shown in Figure 5.22, is the result of summing over the three symmetry energy potentials within CoMD for each system. This was done to decrease the statistical error bars and examine the overall dynamical nature. The experimental data largely describes the IMF being emitted in the forward direction relative to the

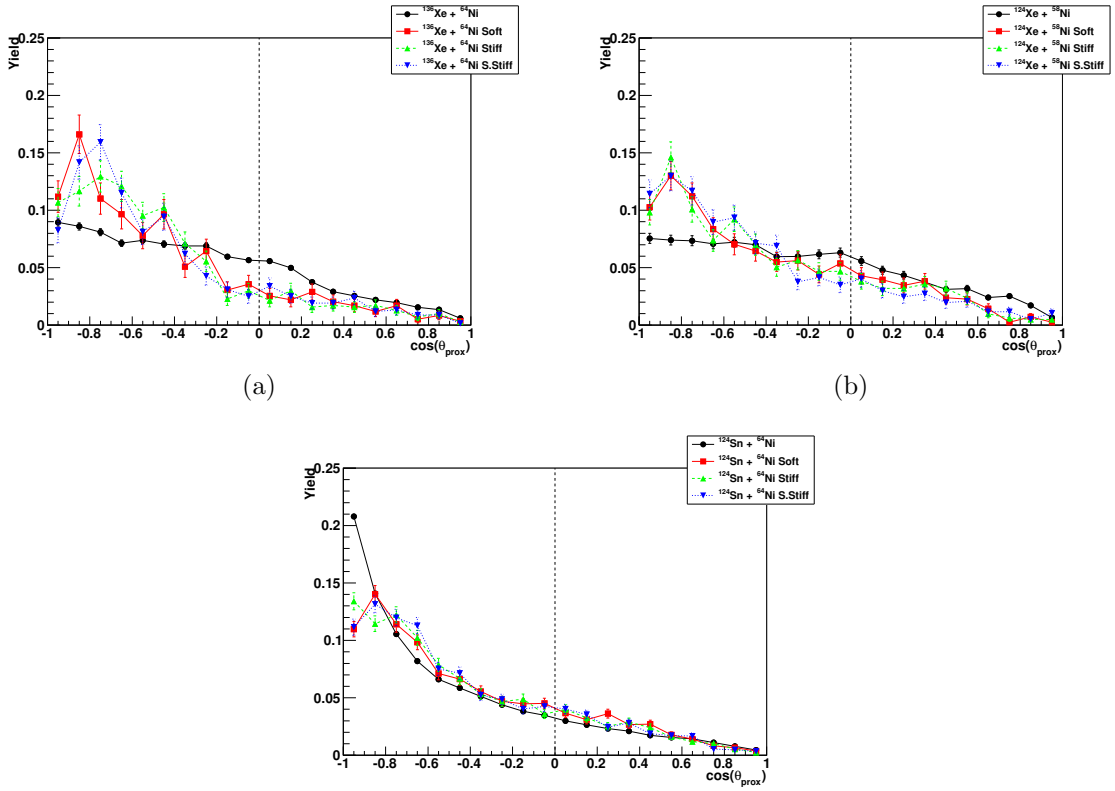

(a) (b)

(c)

Figure 5.23: Comparison of experimental and cooled CoMD+GEMINI $cos(\theta_{prox})$ Angular Distributions for the ^{136}Xe+^{64}Ni (a), ^{124}Xe+^{58}Ni (b), and ^{124}Sn+^{64}Ni (c) IMFs respectively. The cooled CoMD is the result of CoMD simulations cooled with GEMINI[83, 84, 85]. Experimental data is shown in black (circles, solid line) with filtered CoMD results for the soft, stiff, and super-stiff case shown in red (circles, solid line), green (triangles, dashed line) and blue (upside-down triangle, dotted line) respectively.

PLF.

However, secondary decay effects are taken into account by cooling CoMD via GEMINI as seen in Figure 5.23. The GEMINI-cooled CoMD is more peaked near $cos(\theta_{prox}) = -0.8$. This is indicative of the IMF emitted in the forward direction after the QP rotates for a significant amount of time before breaking up. The hot PLF can be seen cooling by secondary emission of a particle, thereby slowing relative

to the emitted IMF. The cooled CoMD more closely agrees with the experimental data suggesting IMF is emitted in the forward direction. The experimental data and cooled CoMD appear to suggest that secondary decays, especially with respect to the PLF, are significant and sufficiently describe the forward focused IMF emission via the $cos(\theta_{prox})$ observable.

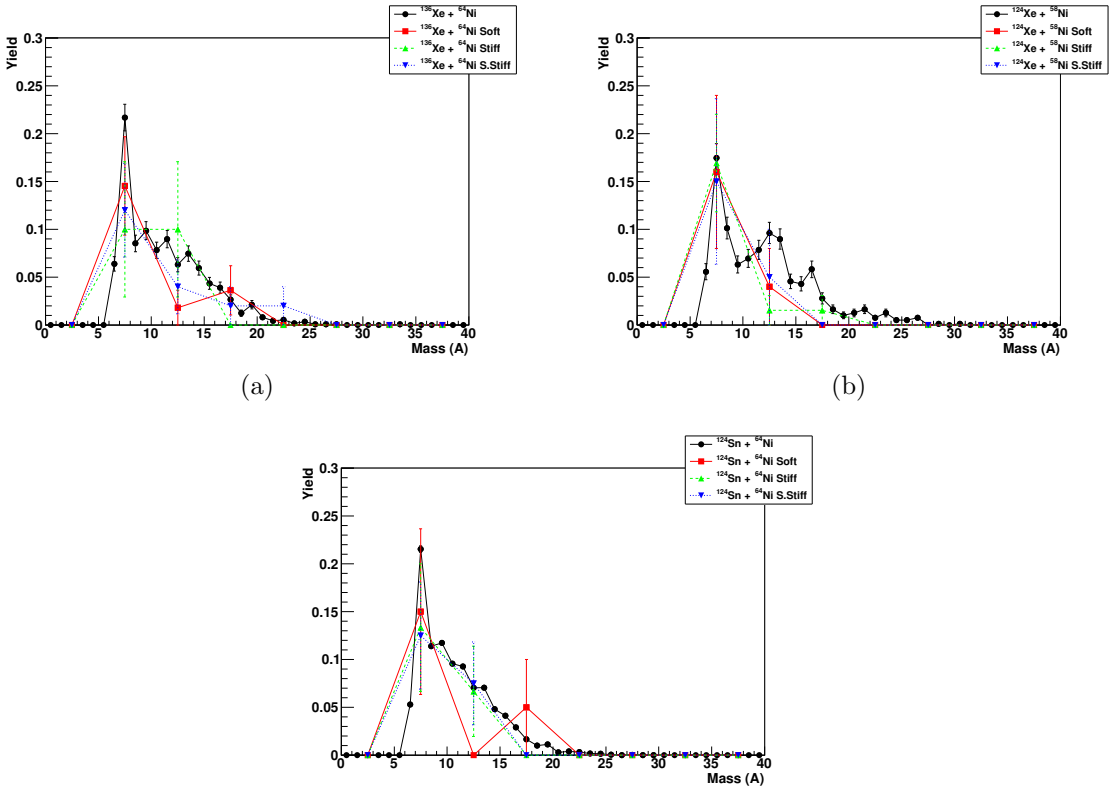

Figure 5.24: Comparison of experimental and CoMD A_{IMF} Distributions for the ^{136}Xe+^{64}Ni (a), ^{124}Xe+^{58}Ni (b), ^{124}Sn+^{64}Ni (c) systems. Experimental data is shown in black (circles, solid line) with filtered CoMD results for the soft, stiff, and super-stiff case shown in red (circles, solid line), green (triangles, dashed line) and blue (upside-down triangle, dotted line) respectively.

Finally, the IMF mass distributions were examined with respect to simulated

results in order to understand how the A_{IMF} may be affecting the angular distributions and the possible influence of E_{sym}. Figure 5.24 shows experimental A_{IMF} compared to the hot CoMD. The statistics for the hot CoMD are low but do show a slight difference between the different stiffness of the symmetry energy with the stiff or super-stiff usually more closely matching the experimental data. The ^{124}Xe+^{58}Ni system is the exception and none of the CoMD simulations are a close match to the experimental IMF mass distribution. Within error bars, the hot CoMD is a good fit to the experimental data.

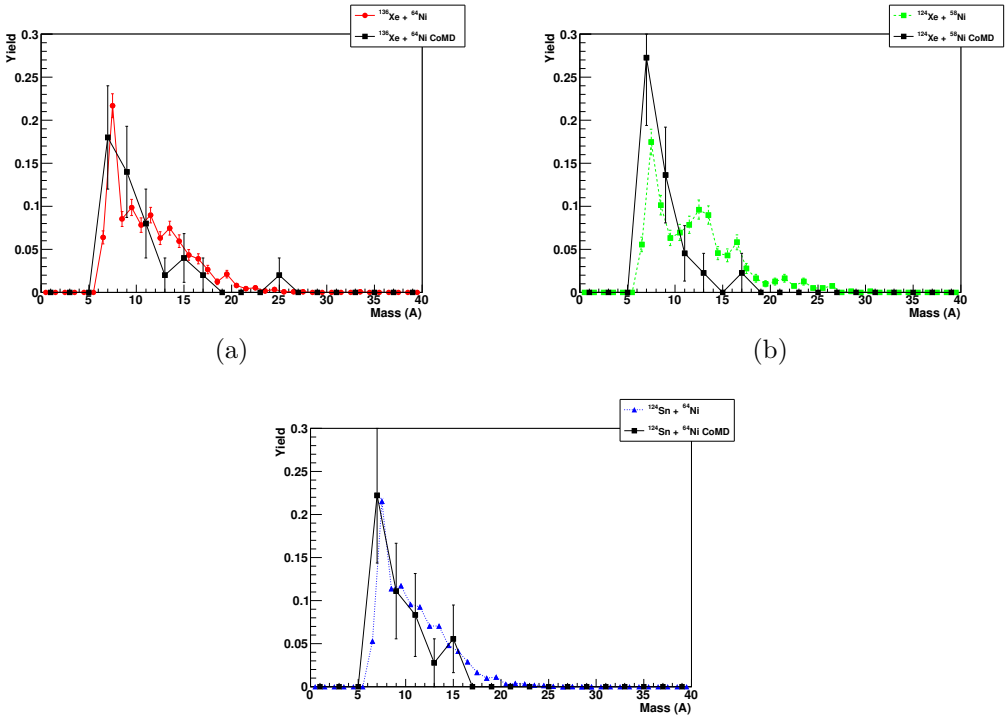

(a) (b)

(c)

Figure 5.25: Comparison of experimental and total CoMD A_{IMF} Distributions for ^{136}Xe+^{64}Ni (a), ^{124}Xe+^{58}Ni (b), and ^{124}Sn+^{64}Ni (c). The total CoMD is from summing the CoMD together the three symmetry energy parameterizations. CoMD data is shown in black (circles, solid line) with experimental results for the ^{136}Xe+^{64}Ni, ^{124}Xe+^{58}Ni, ^{124}Sn+^{64}Ni shown in red (circles, solid line), green (triangles, dashed line) and blue (upside-down triangle, dotted line) respectively.

Combining the output of the CoMD (summing the CoMD events together from all three symmetry energy parameterizations) to look at just the dynamical picture without respect to the influence of the symmetry energy is shown to have a positive effect in matching the simulated A_{IMF} distribution by increasing the statistics as shown in Figure 5.25. In Figure 5.25, all three systems are in better agreement with the combined CoMD. The error bars are still large even with increased statistics and increased bin width. The distributions of A_{IMF} after cooling the CoMD with GEMINI are a different story.

As expected, the A_{IMF} distribution after cooling with GEMINI is shifted down, and peaked at $A_{IMF} = 6$. For a minimum $Z = 3$, this would correspond to an overproduction of ^{6}Li as would be expected out of GEMINI. This is shown in Figure 5.26. The CoMD+GEMINI A_{IMF} distributions quickly tail-off for $A_{IMF} > 9$ where as the experimental distributions continue out to $A_{IMF} > 15$. So although the angular correlations seem to better agree, in some cases, with the CoMD+GEMINI simulations, it is clear there are some underlying dynamical processes masked by an abundance of statistical processes in the experimental data. In the following section, Section 5.5, the disentanglement of dynamic vs. statistical events is described in greater detail.

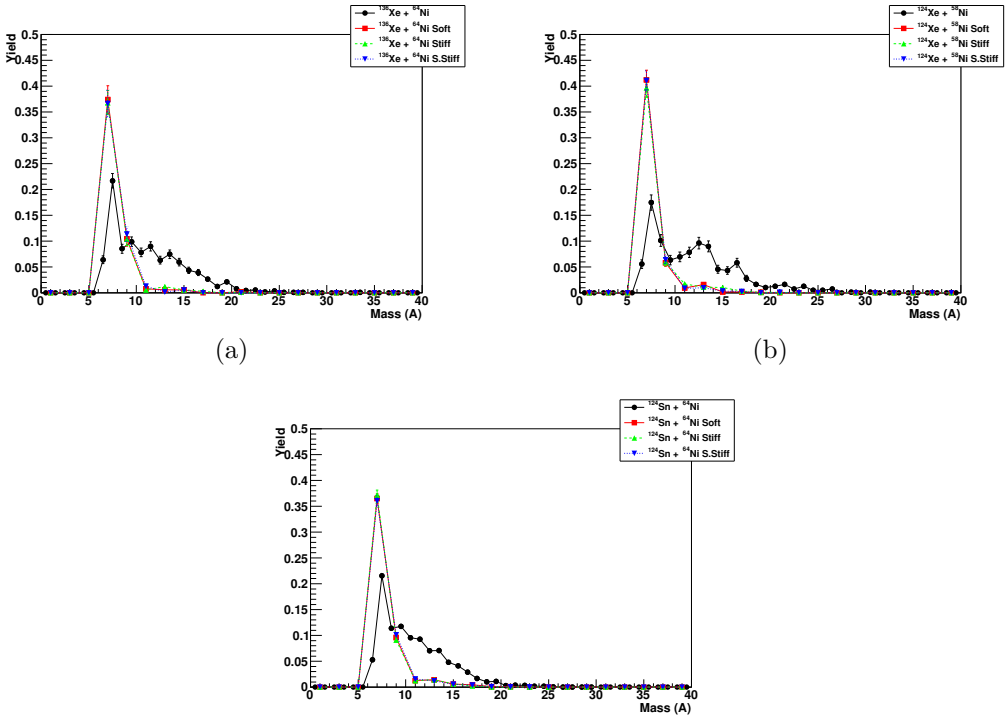

Figure 5.26: Comparison of experimental and CoMD+GEMINI[83, 84, 85] A_{IMF} Distributions for ^{136}Xe+^{64}Ni (a), ^{124}Xe+^{58}Ni (b), and ^{124}Sn+^{64}Ni (c). Experimental data is shown in black (circles, solid line) with filtered CoMD+GEMINI results for the soft, stiff, and super-stiff case shown in red (circles, solid line), green (triangles, dashed line) and blue (upside-down triangle, dotted line) respectively.

5.5 Statistical vs. Dynamical Experimental Events

Although the GEMINI-cooled CoMD appears to fit reasonably well to the experimental data there are still small discrepancies in the fit of the angular and A_{IMF} distributions. The lab frame velocity of the PLF ($\vec{v}^{lab}_{PLF}$) is compared to that of the GEMINI-cooled CoMD in Figure 5.27 and it clearly shows there is a significant bimodal feature to the experimental distribution as seen in black. The filtered CoMD+GEMINI PLF velocity distribution is shown in red. The bimodal PLF velocity distribution can then be bifurcated such that a cut is applied at $\vec{v}^{lab}_{PLF}/c = 0.135$

in the lab frame for the PLF. This results in the PLFs being divided into low (red shaded region) and high (green shaded region) velocity PLFs as shown in Figure 5.27. The resulting lower velocity modality of the experimental distribution is reasonably

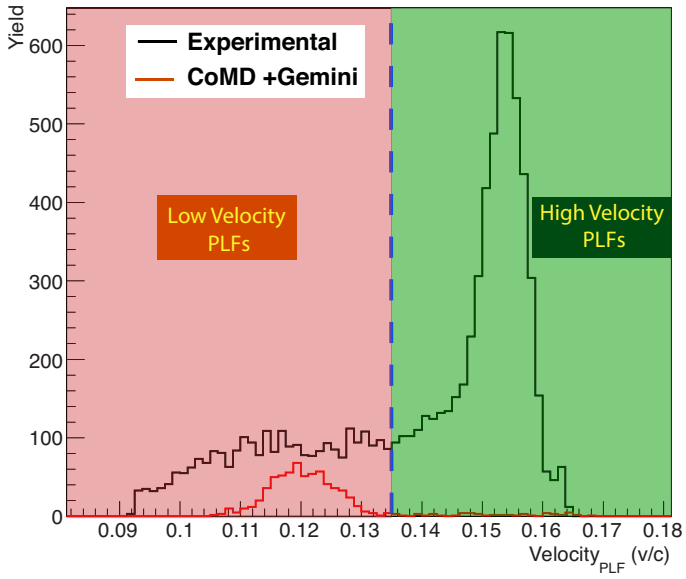

Figure 5.27: Lab frame velocity of the PLF comparison between filtered CoMD+ GEMINI and the experimental data. The experimental data from ^{136}Xe+^{64}Ni at 15 MeV/nucleon is shown and is representative of the other systems.

described by the CoMD+GEMINI after the FAUST filter. Further examination of the filtered CoMD+GEMINI events (red histogram in Figure 5.27) revealed that these events are largely composed of a QP where $A_{QP} \sim A_{system}$. These fusion-like events then decayed into two heavy reaction partners resembling a heavy PLF ($A_{PLF} < 190$) and coincident IMF (with no TLF or QT). The statistical decay of a fusion-like QP on long time scales makes up the statistical portion of the experimental ternary breaking observed earlier in this section.

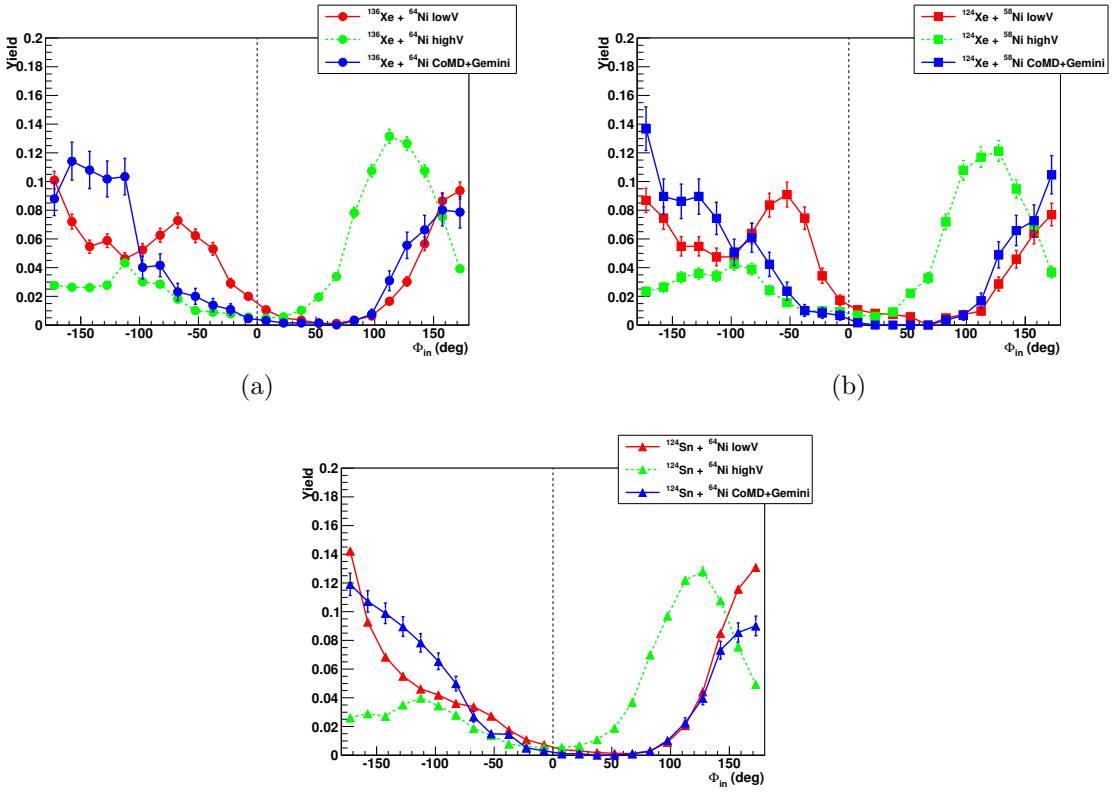

Figure 5.28: Comparison of dynamical and statistical breaking of experimental systems versus filtered CoMD+GEMINI Φ_{in} Angular Distributions after the PLF velocity cut. Data is shown for for ^{136}Xe+^{64}Ni (a), ^{124}Xe+^{58}Ni (b), ^{124}Sn+^{64}Ni (c) PLFs. The experimental high velocity cut (dynamical) events are shown in green and the low velocity (statistical) events in red. The filtered CoMD+GEMINI is shown in blue.

In Figure 5.27 the experimental data for the ^{136}Xe+^{64}Ni system is shown as the black, bimodal histogram with the GEMINI-cooled CoMD shown as the smaller red histogram centered near $\vec{v}^{lab}_{PLF}/c = 0.12$. This velocity cut, when re-examining the angular distributions, dramatically emphasizes the dynamical vs. statistical ternary breaking of the reaction system especially in the case of the in-plane (Φ_{in}) and $cos(\theta_{prox})$ angular distributions, shown in Figures 5.28 and 5.29 respectively. There is a clear difference between the higher-velocity PLFs and the lower-velocity PLFs

associated with the statistical breaking as seen through the GEMINI-cooled CoMD. Figure 5.28 shows there is very good match between the experimental, statistical Φ_{in} and that described by CoMD+GEMINI. Additionally, there is a clear difference in the experimental Φ_{in} distributions between the statistical and dynamical contributions. The statistical contribution is centered around $\Phi_{in} = \pm 180°$ where as the dynamical contrition is centered closer $\Phi_{in} = 110°$ for all three systems.

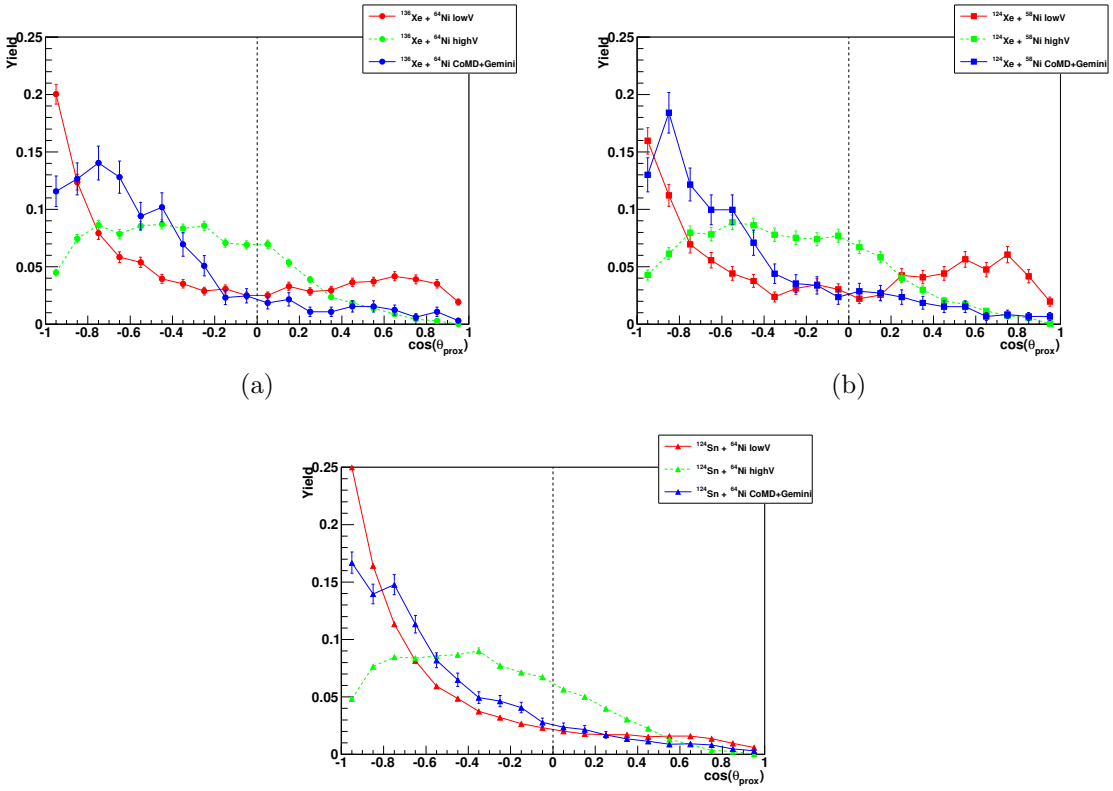

(a) (b)

(c)

Figure 5.29: Comparison of dynamical and statistical breaking of experimental systems versus filtered CoMD+GEMINI $cos(\theta_{prox})$ Angular Distributions after the PLF velocity cut. Data is shown for for ^{136}Xe+^{64}Ni (a), ^{124}Xe+^{58}Ni (b), ^{124}Sn+^{64}Ni (c) PLFs. The experimental high velocity cut (dynamical) events are shown in green and the low velocity (statistical) events in red. The filtered CoMD+GEMINI is shown in blue.

These higher velocity PLFs, representing the dynamical breaking, match well with the lower mass, higher energy PLFs. This lends stronger credence to these higher energy, lower mass QPs being suggestive of semi-peripheral to peripheral impact parameters and is in good agreement with previously published theoretical work. In contrast, the statistical breaking of the QP/reaction system, as determined by the lower velocity PLF cut ($\vec{v}^{lab}_{PLF}/c \leq 0.135$), represents QPs that are at more central to mid-peripheral impact parameters.

Figure 5.29 shows the statistical vs. dynamical experimental $cos(\theta_{prox})$ angular distributions. The CoMD+GEMINI is shown in blue, the lower velocity PLFs in red, and the higher velocity PLFs in green. Comparing the CoMD+GEMINI to the lower velocity PLFs shows that both are representative of the the IMF being emitted in the forward direction and are in good agreement with each other. Figure 5.29 also reinforces the conclusions of those drawn in the Φ_{in} distributions (shown in Figure 5.28) where there is good agreement between CoMD+GEMINI and the lower velocity PLFs. However, the $cos(\theta_{prox})$ distributions shown in Figure 5.29 add additional information as to the emission preference of the IMF relative to the PLF. Although the IMFs are still preferentially emitted forward in the dynamical $cos(\theta_{prox})$ distributions, there is a clear distinction between the statistical and dynamical $cos(\theta_{prox})$ contributions from the experiment. The statistical, experimental $cos(\theta_{prox})$ distributions match the sharp peak of the CoMD+GEMINI distribution near $cos(\theta_{prox}) = -1$.

Additionally, we can examine the isospin content of the IMFs of the dynamically vs. statistically emitted IMFs as a function of $cos(\theta_{prox})$ as shown in Figure 5.30. Figure 5.30 shows the statistical emission of IMFs in solid lines whereas the dynamical emission is described by the dashed lines. In the case of the statistically emitted IMFs, there is a clear isotropic emission of the IMF with respect to the IMF

isopin content. Additionally there is no clear dependence on the entrance channel isospin asymmetry between the three systems. There may be an isospin dependence within the Z=54 systems with the ^{136}Xe+^{64}Ni system emitting slightly more neutron rich IMFs when compared to ^{124}Xe+^{58}Ni, as we would expect. However, there is a clear deviation between the Z=54 and Z=50 systems. The ^{124}Sn+^{64}Ni system ($N/Z = 0.1702$) yields the more neutron rich, statistically emitted IMFs even though its entrance isospin asymmetry is slightly less than the ^{136}Xe+^{64}Ni system ($N/Z = 0.1800$). However, the system ordering does follow the trend as described by the fissility parameter[135, 136], Z^2/A, as tabulated in Table 5.2. In this way, the system with the lowest fissility parameter, ^{124}Sn+^{64}Ni with a $Z^2/A = 32.36$, emits more neutron rich IMFs where as the system with the highest fissility parameter, ^{124}Xe+^{58}Ni, emits more symmetric IMFs.

Table 5.2: Fissility parameter, system-by-system

System	Fissility Parameter (Z^2/A)
^{124}Sn+^{64}Ni	32.36
^{136}Xe+^{64}Ni	33.62
^{124}Xe+^{58}Ni	36.95

Contrastingly, the dynamically emitted IMFs are emitted anisotropically with a dependence on the entrance channel isospin asymmetry. The more neutron rich, dynamically emitted IMFs are emitted backward ($cos(\theta_{prox}) > 0$) with more neutron poor IMFs being emitted in the forward direction ($cos(\theta_{prox}) < 0$). The more neutron rich IMFs being emitted backward are suggestive of a subset of events that are the result of a QP that rotates briefly before breaking into a PLF and IMF. The IMFs

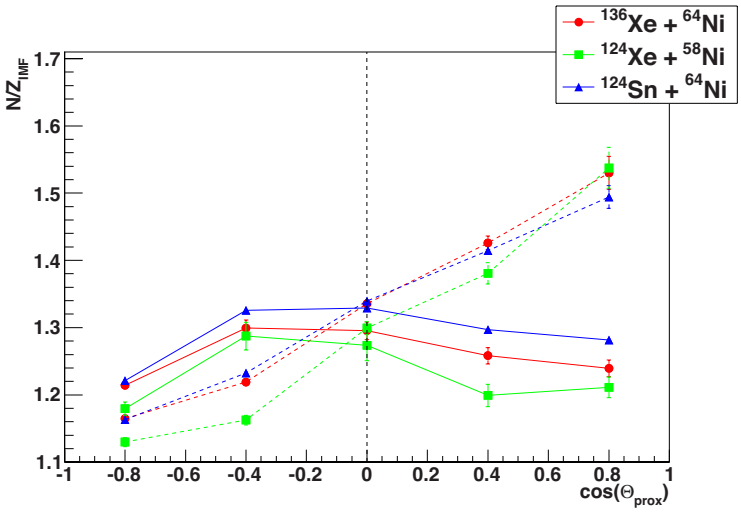

Figure 5.30: Comparison of N/Z isospin content vs $cos(\theta_{prox})$ distributions of dynamically and statistically emitted IMFs from the experimental systems. Data is shown for for ^{136}Xe+^{64}Ni (a), ^{124}Xe+^{58}Ni (b), ^{124}Sn+^{64}Ni (c) IMFs in red, green, and blue respectively. The experimental, dynamical events are shown in dashed lines; in contrast, the statically emitted IMFs are shown with a solid line.

emitted in the forward direction are likely emitted after the QP has a longer time to rotate after separation from the QT. This can be visualized in Figure 5.31 where we can see that after the QP separates from the QT, the QP can rotate significantly before breaking into the PLF and IMF.

Larger rotations have been correlated to a longer time between QP-QT separation and QP break-up[70, 130, 131]. On longer time scales, the QP has more time to equilibrate with any neutron enrichment that occurred near the neck region, thereby decreasing the neutron enrichment of the emitted IMF. However, on shorter time scales, where the IMF is emitted quickly backward (toward the neck region), it is shown in Figure 5.30 as it has been shown previously by Refs.[70, 130, 131], that there is an neutron enrichment of the IMF emitted close to the neck region between the QP and QT shortly after interaction. The short rotation time does not allow

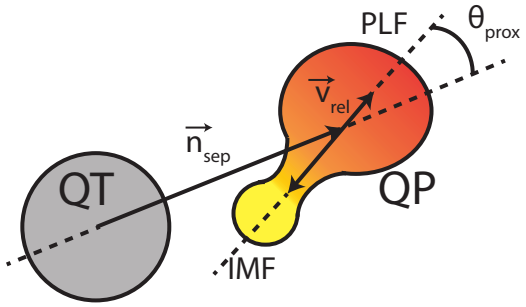

Figure 5.31: 2D Projection of the QP-QT separation and subsequent QP breakup. The QT is described by the gray sphere on the left. The QP is described as the colored, deformed shape on the right. The QP decays into a PLF and IMF. The time from QP-QT separation to QP breakup has been shown to be directly correlated to the degree of rotation[70, 130, 131] described by $cos(\theta_{prox})$

.

for the equilibration of neutron enrichment that occurred in the lower density neck region formed between the interacting projectile and target.

A small dependence on the entrance channel isospin asymmetry also exists with the ^{136}Xe+^{64}Ni and ^{124}Sn+^{64}Ni systems yielding more neutron rich IMFs than the ^{124}Xe+^{58}Ni system. The dynamically emitted IMFs from the two neutron rich systems are very close in isospin content with the ^{136}Xe+^{64}Ni, yielding slightly more neutron rich IMFs. Typically when there appears to be a deviation from this trend, the isopsin content of the dynamical IMFs (between the two neutron rich systems) are within error bars of each other.

However, it still remains that the hot CoMD statistics that make it through the FAUST software filter are quite low. A direct comparison between the experimental data and hot CoMD is not possible observable-by-observable. It is also worth mentioning that detector geometry and energy thresholds are also likely a significant consideration when examining the reaction dynamics.

In summary, it has been shown, through the examination of several angular cor-

relations, that cuts in mass and energy of the reconstructed QP (A_{QP} and E_{QP} respectively) provide a qualitative surrogate to impact parameter. The angular correlations also allowed for the examination of the gross trends with respect to QP rotation after QP-QT separation and the IMF angle of emission. Additionally the QP mass and energy cuts allowed for the examination of the qualitative impact parameter dependence of the IMF angle of emission showing a clear trend in anisotropy of the emission at semi-peripheral impact parameters. It has been shown that experimental angular and velocity correlations via Ψ_{out}, Φ_{in}, and $cos(\theta_{prox})$ are well described by GEMINI-cooled CoMD whereas the IMF mass distributions are better described by the hot CoMD.

When the $cos(\theta_{prox})$ distributions were examined by cutting on high or low lab frame PLF velocity, there was a clear difference in the dynamical vs. statistical contributions where the statistical contribution was well described by the GEMINI-cooled CoMD. Finally, a clear trend in the neutron enrichment of the dynamically emitted IMFs as a function of $cos(\theta_{prox})$ was shown. Specifically, it has been shown that the IMFs dynamically emitted backward (toward the neck) are more neutron rich than those emitted forward. This is in contrast to the isotropic neutron enrichment of the statistically emitted IMFs. The system-by-system N/Z vs. $cos(\theta_{prox})$ distributions of the dynamically emitted IMFs are ordered by system isospin content ($\delta = (N - Z)/A$) whereas the statistically emitted IMFs are ordered by system fissility parameter (Z^2/A).

6. QUASI-PROJECTILE SHAPE ANALYSIS

Nuclear reactions just below the Fermi energy present a unique opportunity for probing the dynamics of nuclear material below normal nuclear density using shape deformations in momentum space. Competition between fusion and quasi-fission, in semi-peripheral collisions, and deep-inelastic transfer (multiplicity$\geq$2) mechanisms, in more peripheral collisions, dominate the exit channels. However, composite systems resulting from semi-peripheral collisions are predicted to exhibit momentum space shape deformations with a large associated angular momentum. These hot systems are predicted to possibly break into a ternary system of two heavy fragments (projectile and target-like) with a coincident intermediate mass fragment emission. In some cases, as noted by Refs.[59, 58], the system may promptly break into three nearly symmetric bodies. However, in the systems being examined in this experiment, the more likely scenario is to have the system separate into a hot QP and QT with the the subsequent breakup of the QP into a PLF and IMF. This likelihood is due to both the degree of reaction system asymmetry, inverse kinematics, as well as bias from the construction of the detector[63]. In the remainder of this section, the measurement of the QP quadrupole deformation will be analyzed and then compared to simulations with the intent of extracting information about the dynamical nature of the process, as well as a possible influence of the symmetry energy on the QP break-up.

In this section, we explore the momentum deformations via quadrupole and octupole fluctuations as described in Eqs. 6.1 and 6.2, respectively.

$$Quad_{mom} = \sum_{i=1}^{A} \frac{2p_{z_i}^2 - p_{y_i}^2 - p_{x_i}^2}{A} \tag{6.1}$$

$$Oct_{mom} = \sum_{i=1}^{A} \frac{5p_{z_i}^3 - 3p_{z_i}(p_{x_i}^2 + p_{y_i}^2 + p_{z_i}^2)}{A} \tag{6.2}$$

The terms p_{x_i}, p_{y_i}, p_{z_i} represent the x, y, z components of the momentum vector of the i^{th} particle in the center of mass with A being the particle's mass. $Quad_{mom}$ and Oct_{mom} represent the quadrupole and octupole momentum fluctuation value as calculated.

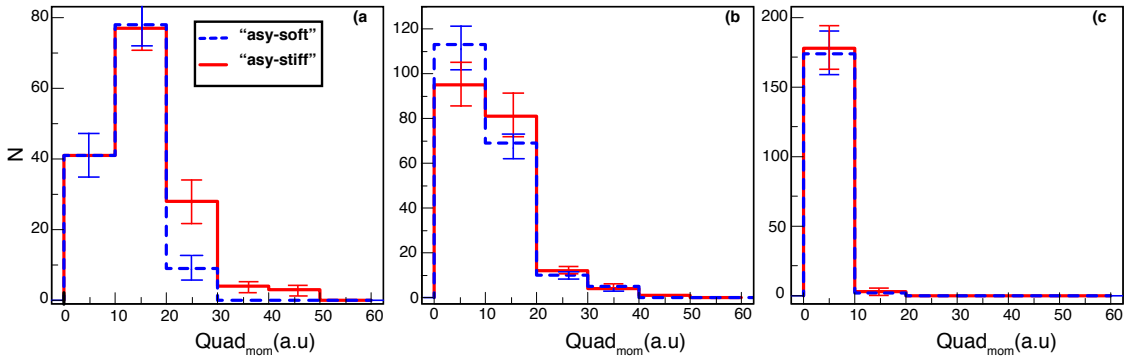

Figure 6.1: Quadrupole fluctuations of the QP, in position space, for ^{132}Sn+^{64}Ni at 10 MeV/nucleon. Impact parameters shown are 6 fm(a), 7 fm(b), and 8 fm(c) at time=500 fm/c. Dashed blue lines represent the asy-stiff case of the symmetry energy; solid red lines are the asy-soft. Data from Refs. [11, 41].

Baran, Di Toro and Colonna et al.[47, 25, 45, 11, 44, 48, 41] have described for many years how the hot QP, just after separation, may be highly deformed and subsequently decay into two smaller reaction partners via IMF emission. The authors have shown that momentum fluctuations of the hot source just before decay are predicted to be sensitive to the density dependence of the symmetry energy as shown in Figures 6.1 & 6.2. These deformed sources are predicted to lead to breakup of the QP on long time scales ($t > 3000$ fm/c). This deformation, prior to break up,

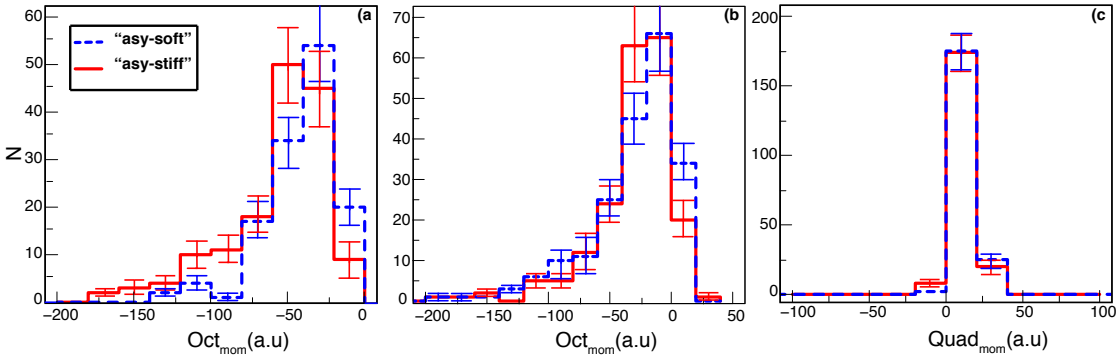

Figure 6.2: Octupole fluctuations of the QP, in position space, for ^{132}Sn+^{64}Ni at 10 MeV/nucleon. Impact parameters shown are 6 fm(a), 7 fm(b), and 8 fm(c) at time=500 fm/c. Dashed blue lines represent the asy-stiff case of the symmetry energy; solid red lines are the asy-soft. Data from Refs. [11, 41].

should be possible to measure via reconstruction of the two heavy reaction partners (PLF and IMF) into the QP via lab frame detectors. In this way, it should be possible to measure the deformation of the QP near the time of break-up.

The shape fluctuations on long time scales can also be seen in simulations using CoMD. On very long times scales, typically longer than 5000-7000 fm/c, the system retains a large amount of excitation. This can be seen in Figure 6.3 where system excitation energy (E^*) is plotted as a function of time. There is approximately 75-100 MeV of excitation energy out to times greater than 5000 fm/c. This can also be seen in momentum fluctuations within CoMD. The projectile interacts with the target on short time scales, forming a highly deformed compound system. At semi-peripheral to peripheral impact parameters, this compound system then re-separates into two reaction partners. These reaction partners, particularly the QP in the case of asymmetric systems in inverse kinematics, then have a long period of fluctuating quadrupole moment as a function of time as shown in Figure 6.4. Only in a few cases, approximately $\leq$ 1%, the QP could then decay dynamically, due

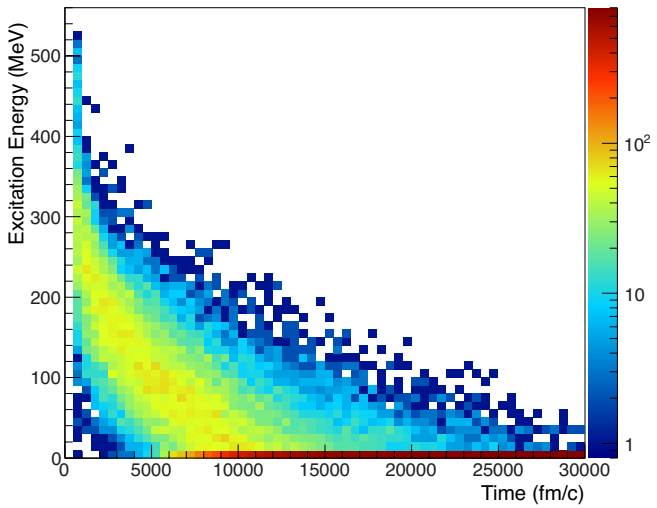

Figure 6.3: Excitation Energy vs Time for ^{136}Xe+^{64}Ni at 15MeV/nucleon using the stiff parameterization of the symmetry energy. There are 500 events simulated for each time step.

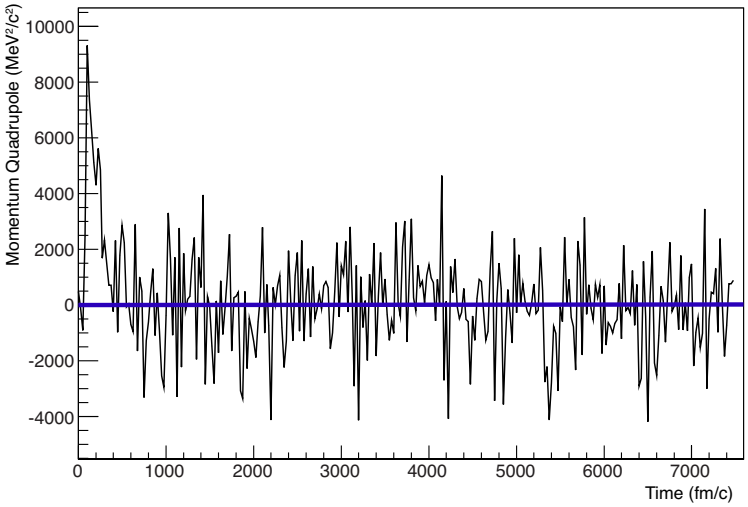

Figure 6.4: Momentum Quadrupole vs Time for ^{136}Xe+^{64}Ni at 15 MeV/nucleon using the stiff parameterization of the symmetry energy.

to large momentum fluctuations. It should be noted that only a small number of events (∼200) were simulated when studying the excitation energy and momenta deformations as a function of time.

It is not possible to measure the individual nucleon momenta in this energy regime due to the fact that the system does not fragment into many individual light charged particles. Additionally, on average, only two heavy fragments are detected per event. This poses a particularly difficult problem in determining the deformation of the QP prior to fragmentation. Using only two fragments in the QP frame, the momenta of the two particle system, by definition, sum to zero. In this two-body case, the momentum quadruple would always equal zero, suggestive of a spherical QP in momentum space. In order to address this issue and that of having simulations for CoMD that dynamically cool only to 3000 fm/c, a qualitative surrogate is proposed for examining the deformation of the QP prior to fragmentation. The surrogate involves calculating the quadrupole deformation in velocity space (Eq 6.3).

$$V_{quad} = \sum_{i=1}^{N} 2v_{z_i}^2 - v_{y_i}^2 - v_{x_i}^2 \tag{6.3}$$

The terms $v_{x_i},\ v_{y_i},\ v_{z_i}$ represent the x, y, z components of the velocity vector of the i^{th} fragment in the QP center of mass for N particles. Instead of using momentum, the velocity of the two heaviest reaction partners detected is used. The sum of the two velocity vectors is not required to be equal to zero in velocity space. In this way, a spherical nucleus at the time of separation would have a velocity quadrupole equal to zero. Deformation of the QP may be measured by finite deviations from zero in the velocity quadrupole. As has been shown in the previous chapter, events from CoMD cooled with GEMINI have lost much of the information from the dynamical stage of the interaction. Therefore, we only consider the events directly from CoMD,

filtered through the FAUST software filter, that exhibit a ternary breaking. Again, the CoMD for the remainder of this study was run out to $t = 3000\ fm/c$. With this in mind, it was not possible to detect enough of these events through the FAUST filter to make a clear determination as to the effect of the symmetry energy based on this observable alone.

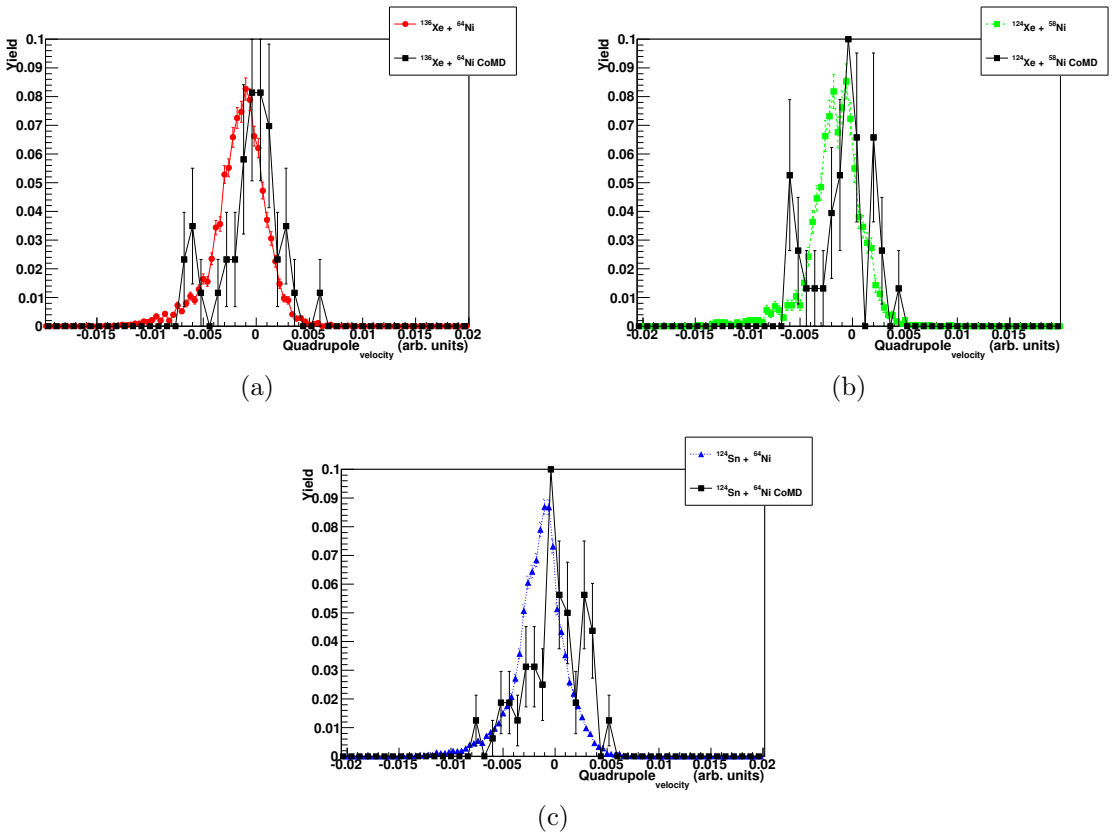

(a) (b)

(c)

Figure 6.5: Comparison of experimental and total CoMD Velocity Quadrupole Distributions for ^{136}Xe+^{64}Ni (a), ^{124}Xe+^{58}Ni (b), and ^{124}Sn+^{64}Ni (c) PLFs. The total CoMD is the result of summing the CoMD events together from all three symmetry energy parameterizations and is shown in black (squares solid line). Experimental data for ^{136}Xe+^{64}Ni, ^{124}Xe+^{58}Ni, ^{124}Sn+^{64}Ni are shown in red (circles), green (squares), and blue (triangles) respectively.

Figure 6.5 depicts the velocity quadrupole for each system with the experimental data shown in color and the filtered CoMD results shown in black. The CoMD results shown in black are the result of summing the CoMD events together from all three symmetry energy parameterizations in order to get enough statistics to have meaningful error bars. The results of both experimental and simulated data shown have been filtered by only selecting the events that passed the high velocity PLF cut ($\vec{v}^{lab}_{PLF}/c \geq 0.135$ in the lab frame). The experimental and simulated reconstructed, dynamical QPs both exhibit a velocity quadrupole centered around zero. This is suggestive of QPs that are nearly spherical in velocity space with few fluctuations. The experimental V_{quad} distributions are closely described by the hot CoMD.

This has not always been the case when comparing many other observables. The experimental, dynamical QPs have shown, in previously described angular and A_{IMF} distributions, that they are not a great match to the hot CoMD due to secondary decay effects. An attempt to utilize the available statistics via simulations (hot and cold) has been made to examine the influence of the symmetry energy via Sliced Inverse Regression will be described in detail in Section 8. This technique takes into consideration multiple observables simultaneously (see Section 7.1 for a detailed description of the Sliced Inverse Regression algorithm). The consideration of multiple observables simultaneously has recently been mentioned by the community at recent conferences[37, 38] as a possible avenue to explore. Although it would be nice to make a direct comparison to CoMD and SMF, mean field calculations scale with N^3 where the CoMD scales with N^2 making it unfeasible at this time to do a direct comparison of physics observables to SMF.

7. SYMMETRY ENERGY ANALYSIS OF SIMULATIONS*

There are a number of methods that can be used for this multivariate analysis. Usually, they can be grouped together into either iterative or non-iterative methods, each with their own set of benefits and drawbacks. In this analysis, the non-iterative technique Sliced Inverse Regression (Section 7.1) was employed from within the R statistical environment (Section 7.2) in an attempt to test whether or not machine learning has become robust enough, in the past few decades, to determine principal components that would be sensitive to the symmetry energy[81]. This is a novel approach using a combination of several observables utilizing a "bottom-up" approach where a number of observables were measured, event-by-event, with the intent to increase the sensitivity to theoretical differences, such as the underlying nucleon-nucleon (NN) interaction of heavy-ion collisions. The Sliced Inverse Regression Method (SIR) offers the ability to efficiently and, in an unbiased way, perform such an analysis. The results of the analysis are discussed in Section 7.3.

7.1 Sliced Inverse Regression

Multivariate analysis has been around for at least a century in one form or another[137, 138, 139, 140]. However, seminal work by R. A. Fisher[140] examining the power of linear discriminant analysis methods, paved the way for modern multivariate statistical analysis. This original work examined how multivariate statistics could discriminate classifiers in biological taxonomic data sets with, what were considered at the time, a large number of measurements for a set of observable parameters. Fisher found that, utilizing several manipulations of the matrices containing

*This chapter reproduced-in-part with permission from Elsevier from P. Cammarata et al., Sifting Through the Remnants of Heavy-ion Collisions for Observables Sensitive to the Nuclear Equation of State, Nucl. Instruments Methods Phys. A **761**, 1-6, Elsevier, Copyright 2014[81].

the measured data, it was possible to classify several different species of the same variety of plants. These different species can be described as the cohorts, or sub-sets of data. The version of the method used in the analysis described in Section 7.3, namely the Sliced Inverse Regression algorithm[141, 142], is a direct decendent of the linear discriminant analysis technique.

The SIR method includes a suite of statistical significance tests and the ability to analyze more groups of data simultaneously. This was previously absent from earlier versions. In general the SIR algorithm is a set of matrix operations such that it can analyze several subsets of data. In the particular case described herein, each of the subsets, or cohorts, are a different parameterization of E_{sym}. For the case of two forms of the density dependence of E_{sym} (two cohorts of data), the treatment of matrices containing the initial data for each population ($\mathbf{S}_{ij}$ for the asy-stiff and $\mathbf{V}_{ij}$ for the asy-soft) can be described in general terms below (as prescribed by [140]). Explicitly, the matrices $\mathbf{S}_{ij}$ and $\mathbf{V}_{ij}$ are defined as a matrix of data observables with i rows of events for j columns of observables. These matrices will simply be referred to as $\mathbf{S}$ and $\mathbf{V}$ for the remainder of this discussion.

First the mean deviation corrected matrix of the raw data ($\mathbf{S}_{dc}$ and $\mathbf{V}_{dc}$) is calculated by taking the difference of the raw data and its mean value (Eq. 7.1). In this way the mean and sum of each column in the matrix $\mathbf{S}_{dc}$ (and $\mathbf{V}_{dc}$) is zero. Thus

$$\mathbf{S}_{dc} = \mathbf{S} - \mathbf{U}\mathbf{S}(\frac{1}{N_s}), \tag{7.1}$$

where N_s is the number of observed events, $\mathbf{U}$ is a square unit matrix of $N_s \times N_s$ size. The subset of data represented by $\mathbf{V}$ is treated in the same way. The deviation score sums of the matrix for each group (termed $\mathbf{S}_{ds}$ and $\mathbf{V}_{ds}$ respectively) is determined

by taking the product of the transpose of $\mathbf{S}_{dc}$ represented by $\mathbf{S}_{dc}^{T}$.

$$\mathbf{S}_{ds} = \mathbf{S}_{dc}^{\mathbf{T}}\mathbf{S}. \tag{7.2}$$

The sum of squares and cross products of deviations($\mathbf{\Sigma}_{scp}$) is calculated by determining the sum of both $\mathbf{S}_{ds}$+$\mathbf{V}_{ds}$:

$$\mathbf{\Sigma}_{scp} = (\mathbf{S}_{ds} + \mathbf{V}_{ds}). \tag{7.3}$$

The matrices of the mean values of the observables, $\mathbf{UV}(\frac{1}{N_v})$ and $\mathbf{US}(\frac{1}{N_s})$, are matrices of $J \times K$ size where J is the number of samples and K is the number of observables used for the computation. The difference in the means of the observables between the groups, $\vec{\mathbf{D}}$, is thus determined by

$$\vec{\mathbf{D}} = \left[\mathbf{UV}\left(\tfrac{1}{N_v}\right)\right]_{1,K} - \left[\mathbf{US}\left(\tfrac{1}{N_s}\right)\right]_{1,K}. \tag{7.4}$$

Finally, the weighting coefficients for the linear combination are calculated by taking the product of the inverse of $\mathbf{\Sigma}_{scp}$ and $\mathbf{D}$

$$\mathbf{C}_{SIR} = {\mathbf{\Sigma}_{scp}}^{-1}\vec{\mathbf{D}}^{T}, \tag{7.5}$$

where the matrix $\mathbf{C}_{SIR}$ contains the weighting coefficients, yielding a linear relationship

$$SIR_{value} = \lambda_0 x_0 + \lambda_1 x_1 \ldots \lambda_n x_n + c\ , \tag{7.6}$$

with λ_n as the weighting coefficients for each observable for n number of observables and c is a normalization constant to center the data around zero. This is a general description for the two subset cases; the exact algorithm for H subsets of data is

described by Li *et al.*[141].

7.2 R Statistical Environment

"R"[143] is an integrated software suite that facilitates data manipulation, calculation and graphical display of data. It includes an effective data handling and storage facility, a suite of operators for calculations on arrays, a large collection of intermediate tools for data analysis, and graphical facilities for data analysis. R also incorporates a well-developed programming language specific to the R environment. R is designed around a true computer language, and it allows users to add additional functionality by defining new functions. Much of the system is itself written in R language. For computationally-intensive tasks, C, C++ and Fortran code can be linked and called at run time. Advanced users can write C code to manipulate R objects directly. All of the statistical packages (modules) intended for use within R are available, via open-source license, through the CRAN family of Internet sites covering a very wide range of modern statistics.

7.3 Analysis of Theoretical Simulations

The interaction of ^{124}Sn+^{64}Ni at 15 MeV/nucleon was simulated with a Boltzmann-Nordheim-Vlasov based Stochastic Mean Field approximation (SMF), employing the test particle method[47, 82], and the Constrained Molecular Dynamics (CoMD)[3] model. Three different parameterizations of E_{sym} were simulated for both SMF and CoMD. The density dependence of the asymmetry energy parameterizations is shown in Figure 7.1. The asymmetry energy, generally, can be described in two ways. In the case where E_{sym} increases monotonically with increasing density (ρ), the relationship between E_{sym} and ρ can be described as "stiff", or asy-stiff (Figure 7.1). Conversely the "soft" , or asy-soft, can be generally described as the case when

the relationship E_{sym} vs ρ increases to approximately saturation density (ρ_0 ~0.16 fm^{-3}) [17] and then begins to decrease above ρ_0. In the case of CoMD, the "softer" of the three parameterizations of E_{sym} does continue to increase monotonically with density. The stiff E_{sym} for both CoMD and SMF, in Figure 7.1, lay on top of

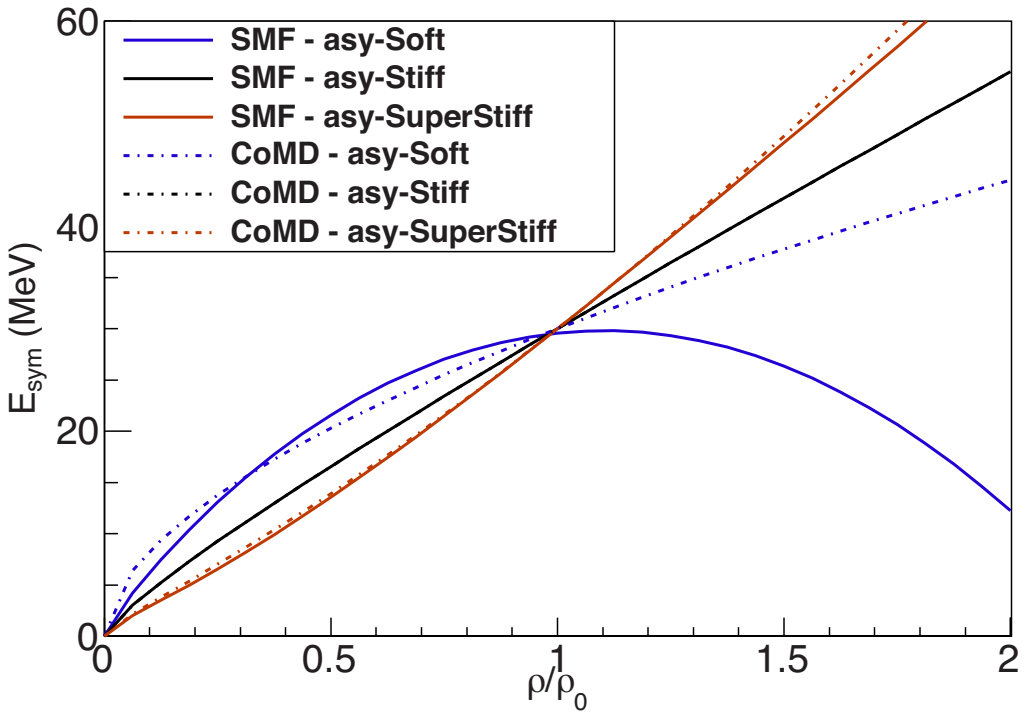

Figure 7.1: The density dependence of the asymmetry energy for SMF and CoMD. Solid lines represent SMF, dashed lines represent CoMD with the soft parameterization in blue, stiff in black and super-stiff in red.

each other. For the super-stiff E_{sym}, although the lines lay close to each other, the super-stiff parameterization for CoMD is slightly more stiff at $\rho/\rho_0 > 1$. However, in the case of the asy-soft, E_{sym} for SMF is clearly much softer than for the CoMD. At saturation density ($\rho/\rho_0 = 1$), the E_{sym} curves intersect as this represents the well constrained normal nuclear density described by the semi-empirical mass

formula for nuclei. At the energy of the simulated reactions for this analysis (15 MeV/nucleon), the 2-body separation (binary) that we are observing will be below saturation density due to the increase in excitation and subsequent increase in volume just after reseparation. In Figure 7.2, the density profile for a 2-body separation of the projectile-like and target-like fragments (PLF and TLF respectively) are depicted for ^{124}Sn+^{64}Ni at 15 MeV/nucleon at t=450 fm/c for an impact parameter of 7 fm in the reaction plane as simulated using the stiff E_{sym} from SMF. In Figure 7.2, the Z-coordinate is parallel to the beam direction with the projectile traveling from low to high value on the Z-coordinate. The Transverse-coordinate represents the plane transverse the the beam direction. The PLF is depicted by the larger, deformed fragment on the right-hand side of the reaction plane. The strong deformation of the PLF and TLF, illustrated in Figure 7.2, is predicted to be dependent on the stiffness of the E_{sym}[11, 25, 41, 44, 45, 47, 48].

Approximately 3,000 and 500,000 events were simulated with each model, SMF and CoMD respectively, to train the SIR algorithm in identifying the way observables behave relative to a change in E_{sym}. The output of SMF (using a flat impact parameter distribution from 6 to 8 fm) was then treated with a coalescence code[46] to identify the free nucleons and clusters that appear in the exit channel based on the locations of the test particles in phase space. The coalescence code output was then filtered in order to select only on the PLF at t=450 fm/c. In the case of CoMD, a triangular impact parameter distribution was used and the simulation was stopped at 400 fm/c. This time was chosen in an attempt to directly compare the results from SMF to CoMD. The data was then filtered with a geometric software filter for the Forward Array Using Silicon Technology (FAUST)[95]. This was done to examine the ability of the SIR method to find observables typically found in experimental

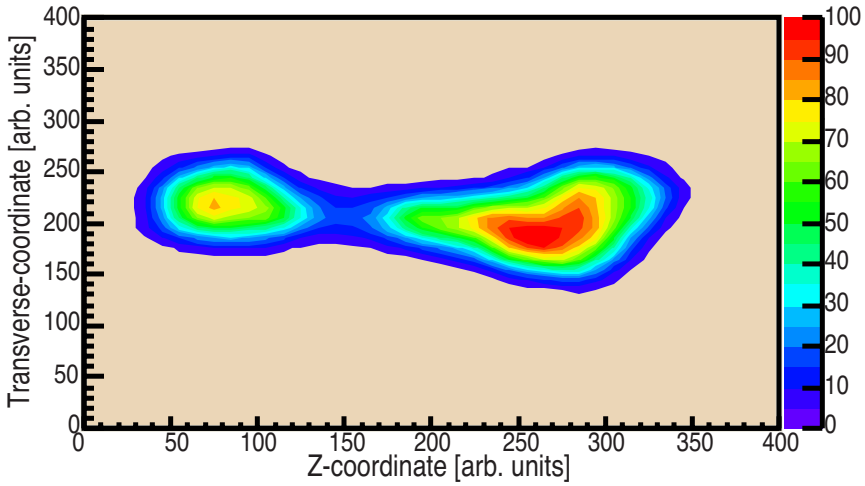

Figure 7.2: A representative, typical density contour of ^{124}Sn+^{64}Ni at 15 MeV/ nucleon in the reaction plane at t=450 fm/c at an impact parameter of 7 fm in coordinate space as simulated by the stiff E_{sym} in SMF with 40 test particles per nucleon. The projectile-like fragment (PLF) is depicted by the larger, deformed fragment on the right and the target-like fragment (TLF) on the left. Density contours range from low to high represented by purple (darker gray) a the the edges of the profile to deep red (transitioning from dark to lighter grays) at the center of the profiles. The Z-coordinate is parallel to the beam direction with the projectile traveling from low to high value on the Z-coordinate. The Transverse-coordinate represents the plane transverse the the beam direction.

data. The data, from CoMD, was gated on binary events (events having only two heavy fragments with Z$\geq$3) followed by a cut in Z and on the velocity parallel to the beam axis in the center of mass (V_{par}^{cm}) to ensure that only the heavy PLF was selected.

For both SMF and CoMD, the sorted outputs were then analyzed by the dimension reduction package[142] within the R statistical environment. Specifically, the Sliced Inverse Regression (SIR) algorithm from this package was used for this analysis. In the case of the SMF simulation, 13 observables were analyzed whereas

only 9 observables were used in the initial analysis of CoMD (no coordinate space observables were output). Specifically, mass (A), charge (Z), excitation energy (E^*), spin (J), center of mass momentum vector components (p_x, p_y, p_z), position in the center of mass frame (x, y, z), distance from the center of the fragment to the center of mass frame (r^2), and the quadrupole($Quad_{mom}$) and octupole (Oct_{mom}) moments, all of the PLF. The Quad_{mom} and Oct_{mom} take the general form

$$Quad_{mom} = \sum_{i=1}^{A} \frac{2p_{z_i}^2 - p_{y_i}^2 - p_{x_i}^2}{A} \tag{7.7}$$

and

$$Oct_{mom} = \sum_{i=1}^{A} \frac{5p_{z_i}^3 - 3p_{z_i}(p_{x_i}^2 + p_{y_i}^2 + p_{z_i}^2)}{A} \tag{7.8}$$

where p_x, p_y, and p_z are the momentum components in the center of mass frame. For SMF the sum is extended over all test particles (i) inside the PLF. The sum, for CoMD, is extended over all nucleons in the PLF. Although, the quadrupole and octupole deformation in momentum space are not directly observable, it has been shown that these measurements may lead to subsequent PLF breaking[11, 25, 41, 44, 45, 47, 48]. It should be noted that because this section is describing a theoretical test case of the discrimination power of the SIR method when applied to nuclear physics applications, the octupole and quadrupole information available in the simulations will be used. However, as has been mentioned in the previous chapter, an experimental surrogate to these observables is required, namely V_{Quad}. These along with other observables can be utilized to distinguish between stiff and soft E_{sym}.

7.4 Determination of Observables and Symmetry Energy Effects

Initially, we analyzed the output from SMF for the stiff and soft asymmetry energy at an impact parameter (b) of 6 fm at t=450 fm/c. We took into account the 13 observables from the output of SMF. By looking at the weighting coefficient of the factors from the linear combination of observables derived from the SIR output, it is possible to evaluate the significance of the contribution to the separation by the magnitude of the absolute value of the weighting coefficient.

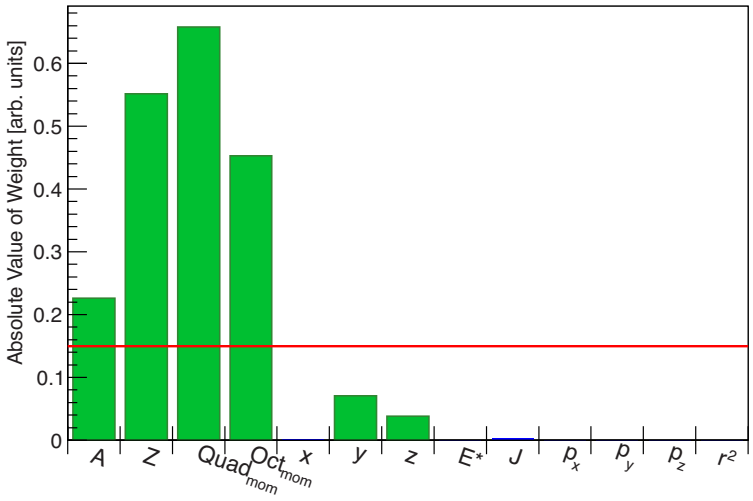

Figure 7.3: Absolute values of the observable weights as determined by SIR for the case of 2 E_{sym} at an impact parameter of 6 fm using SMF. The solid red line, equivalent to an observable weight of 0.15, indicates the cut-off used to determine the most important observables. This value is arbitrarily defined and may vary depending on the analysis.

Figure 7.3 shows the absolute value of the weighted coefficients for each of the 13 observables. The most important observables were chosen to be those that had a weight greater than 0.15, represented by the solid red line. This value is arbi-

trarily defined and may vary depending on the analysis. In this regard, the mass, charge and deformation in momentum space of the PLF (quadrupole and octupole moments) were the most significant terms. By looking at the distributions of the observables for the PLFs individually, it is difficult to make a clear determination as to how they are affected by the asymmetry energy. In Figure 7.4, both E_{sym} are overlaid for each observable that was determined to be significant. A close inspection shows there is no clear separation in the mean value of each observable for the PLFs using the stiff and soft asymmetry energy from SMF.

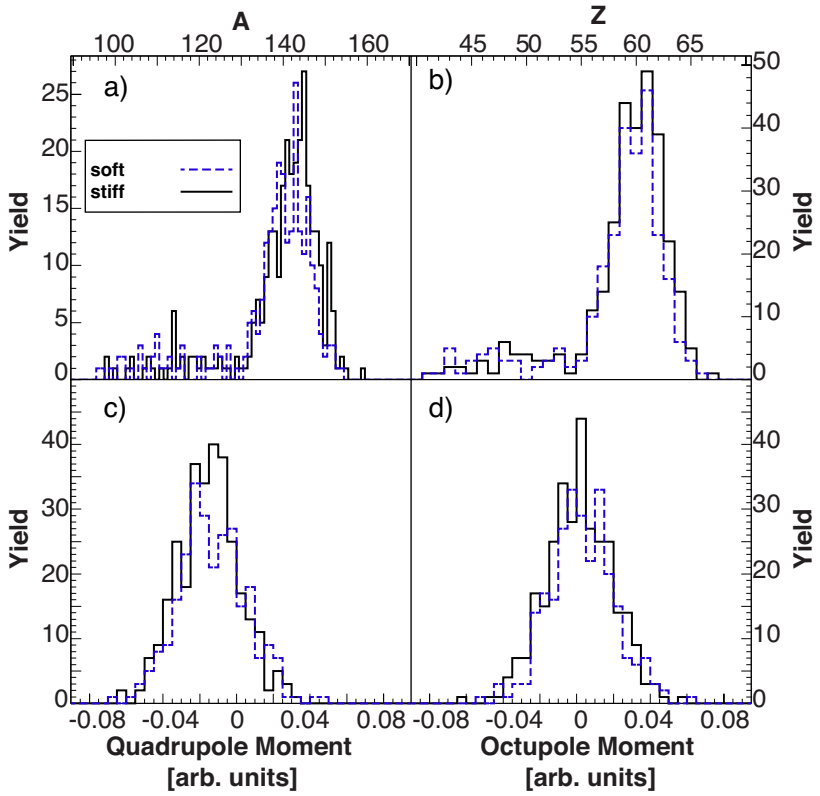

Figure 7.4: Mass (a), Charge (b), Quadrupole Moment (c) and Octupole Moment (d) for stiff (solid black) and soft (dashed blue) E_{sym} at an impact parameter of 6fm. All data shown is for PLFs resulting from a 2-body (binary) breakup of the system at t=450 fm/c using the SMF model.

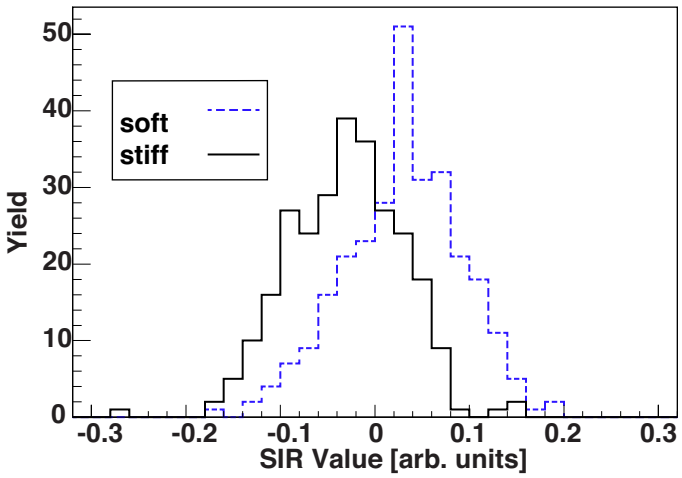

Figure 7.5: Separation of the asymmetry energy via SIR for the projectile-like fragment from SMF. The dashed blue line represents the soft and the solid black line represents the stiff E_{sym} at an impact parameter of 6 fm.

Re-analysis of the same data this time using only the principal observables as determined previously by SIR (shown above the red line in Figure 7.3 as A,Z, $Quad_{mom}$ and Oct_{mom}) provided a clear separation between the mean SIR_{value} for the stiff and soft forms of E_{sym} in SMF, as shown in Figure 7.5. This emphasizes that analyzing the observables together yields a better understanding of the effect of the asymmetry energy on the observables. The analysis, using only the principal observables, yields the function

$$\begin{aligned} SIR_{value} &= -0.7338A + 0.17392Z \\ &+0.97921Quad_{mom} - 0.07429Oct_{mom} + constant\ , \end{aligned} \tag{7.9}$$

where the SIR_{value} is a value based on the linear combination of the weighted observables in arbitrary units.

To verify this separation was not particular to one impact parameter or the forms of the asymmetry energy chosen, the data was re-analyzed this time to include b=6-8 fm and 3 forms of E_{sym}. The impact parameter range was selected for semi-peripheral impact parameters where the probability is highest for heavy (Z≥3) 3- or 4-body breaking of the reacting system at low-intermediate energy. As seen in

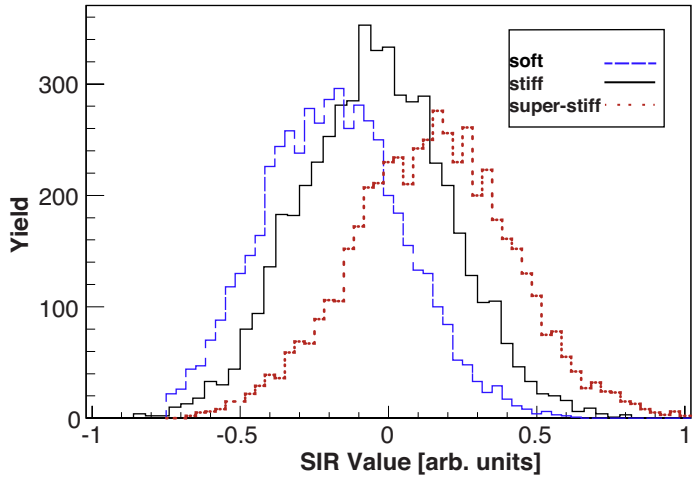

Figure 7.6: Separation of the asymmetry energy via SIR using all three forms of the asymmetry energy from SMF at impact parameters 6, 7, and 8 fm. In this instance, the dashed blue line is for the soft asymmetry energy, the solid black line for the stiff, and dotted red line for the super-stiff.

Figure 7.6, the separation in the mean SIR_{value} for the 3 forms of E_{sym} is still clear. This analysis yielded results that trended with the previous result yielding:

$$\begin{aligned} SIR_{value} &= 0.31727A - 0.75325Z \\ &-0.07374Quad_{mom} + 0.57142Oct_{mom} + constant. \end{aligned} \tag{7.10}$$

The change in the precise values of the weighting coefficients in the linear com-

bination (SIR_{value}) is of little consequence. Although the mean SIR_{value} for the soft and stiff E_{sym} in Figure 7.6 have changed sign, so have the weighted coefficients in Eq. 7.10. The same principal observables are identified as important, and as seen in Figures 7.5 and 7.6, the relative separation of the distributions is not strongly affected by the inclusion of a third asymmetry energy parameterization of the data over additional impact parameters.

Table 7.1: Statistics for SIR using SMF simulations

E_{sym}	Mean	σ	Error	C.I. t-test
Soft	-0.189	0.240	3.35×10^{-3}	
Stiff	-0.044	0.250	3.43×10^{-3}	>99.99%
Super-Stiff	0.133	0.271	3.77×10^{-3}	

An additional set of 3000 events at b=6-8 fm for each E_{sym} were simulated with SMF to test the SIR technique. The weighted linear combination from Eq. 7.10 was then applied directly to the filtered results of these additional 3000 events, confirming the method works for this test case. Table 7.1 shows the mean, half width, standard error, and the confidence interval derived from the t-test (C.I. t-test). The C.I. t-test statistically describes the separation of each parameterization of the density dependence of E_{sym} to be >99.99%.

While the SMF model provides the ability to look at a number of important observables on short time scales and has been valuable in attempts to constrain E_{sym}, CoMD was also analyzed for a more complete comparison between two commonly used, heavy-ion collision dynamics models: a mean field transport calculation and a molecular dynamics simulation. This could prove to be important if a direct com-

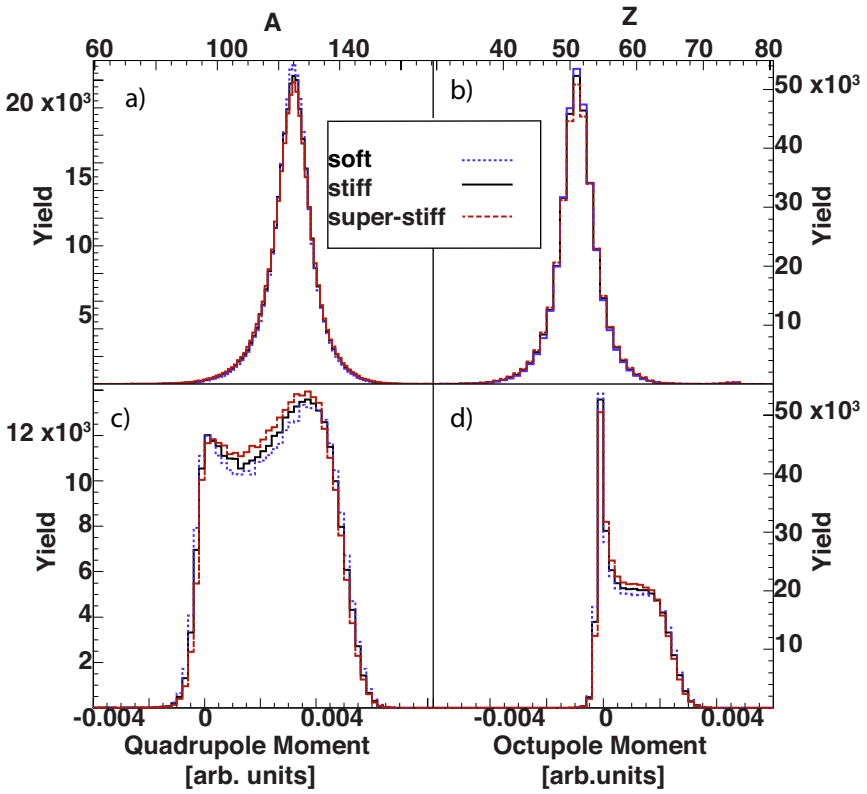

Figure 7.7: Mass (a), Charge (b), Quadrupole (c) and Octupole (d) moments for soft (dotted blue), stiff (solid black), super-stiff(dashed red) and E_{sym} for impact parameters from 6 to 8 fm in CoMD.

parison is to be made to theory using experimental data. As previously stated, the same observables as were used with the SMF model were also used for the analysis of the CoMD output with the exception of the coordinate space observables.

The output of the SIR algorithm using the filtered CoMD data at b=6-8 fm (inclusive) for the three parameterizations of E_{sym} available within CoMD (Figure 7.1) was analyzed. The strongest observables were determined via principal component analysis, as done previously for the SMF dataset. Using SIR with only the most heavily weighted observables as determined by principal component analysis, the

Table 7.2: Statistics for SIR using CoMD simulations

E_{sym}	Mean	σ	Error	C.I. t-test
Soft	1.021×10^{-4}	3.317×10^{-4}	8.12×10^{-7}	
Stiff	0.172×10^{-4}	3.266×10^{-4}	7.89×10^{-7}	>99.99%
Super-Stiff	-3.271×10^{-4}	3.271×10^{-4}	8.00×10^{-7}	

following linear combination was calculated as represented in Eq. 7.11. In this case the linear combination of the most important observables includes E^* and is given as:

$$\begin{aligned} SIR_{value} = &-5.838\times10^{-6}A + 5.227\times10^{-5}Z \\ &-6.991\times10^{-6}E^* - 2.12\times10^{-1}Quad_{mom} \\ &-9.773\times10^{-1}Oct_{mom} + constant. \end{aligned} \tag{7.11}$$

Figure 7.7 shows the mass, charge, octupole and quadrupole moment distributions of the PLFs from CoMD. It can be seen that while there was not a substantial difference in the observables used to extract the E_{sym}, the combination of the most important observables provides a modest, yet statistically significant separation between the means of the SIR_{value} for each E_{sym} (see Figure 7.8). Table 7.2 shows the mean, half width, standard error, and the confidence interval derived from the t-test (C.I. t-test). From this we can see that, although there is a small difference between mean values, there is a statistically significant separation with >99.99% confidence.

From each of the models we can see that some observables give more power to the discrimination between the stiffness of the asymmetry energy. Although in our

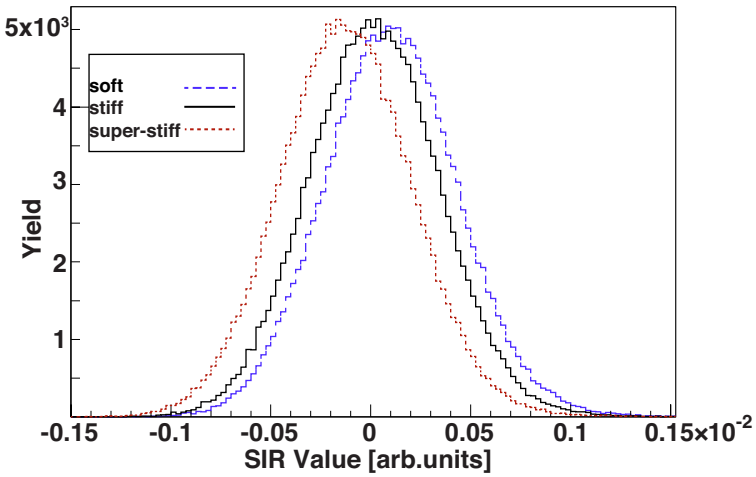

Figure 7.8: Separation of the asymmetry energy by SIR using mass, charge and shape deformation in momentum space (octupole and quadrupole moments) of the projectile-like fragment. SIR_{value} represents an arbitrary value to describe the influence of E_{sym} on collective stiffness or softness of the observables analyzed

analysis it appears that A, Z, octupole moment, quadrupole moment and, in the case of CoMD, the excitation energy of the PLF have the most sensitivity, it is important to recognize that this was not an exhaustive analysis of all the possible observables. The purpose of this report is not to create the "ultimate" composite observable, but to use a number of easily measured observables to demonstrate the strength of the SIR method. Certainly parameters such as dipole fluctuations, velocity correlations between fragments, $\frac{Z}{A}$, $\left(\frac{Z}{A}\right)^2$, or other event-by-event combination of measurements may improve the results of the SIR analysis. There is a physical argument to be made, however, for each of the simple observables that we see from the SIR analysis. For example, SIR suggests that there is a large importance in the mass and charge of the PLF. As such this may be interpreted that there is even the possibility that isoscaling of the heavy or light fragments may provide another observation that contributes to a more collectively sensitive set of observables[96] even though it is not

possible to probe with SIR as it requires event-by-event observables for the input. It should also be noted that it is possible to extract different E_{sym} for the same data set by focusing on a different observable individually. However, by combining multiple observables into a single value will result in a unique solution with a stronger dependence on E_{sym} than any single observable for each experimental data set and theoretical model.

8. SYMMETRY ENERGY ANALYSIS OF EXPERIMENTALLY FILTERED SIMULATION DATA

There has been significant progress in recent years toward placing tighter constraints on the symmetry energy[23, 34, 35, 36]. However, it has been recently suggested that the community should consider methods to analyze the many observables sensitive to the symmetry energy together. This was suggested as an attempt to understand the interplay between the many observables, understand which observables are most sensitive relative to each other, and to attempt to place better constraints in the symmetry energy[37, 38]. In an attempt to extend the analysis of Section 7 and Ref. [81], the results from both hot and cooled CoMD were analyzed through the full FAUST filter. Additionally, a brief study on the secondary decay effects using the the FAUST filter was conducted.

Similar to the theoretical analysis performed in Section 7 and Ref. [81], the Sliced Inverse Regression algorithm was used in an attempt to test the robustness of the method. However, in this section, the SIR algorithm will be used to examine the influence of the symmetry energy on reaction dynamics observables using CoMD simulations results filtered with the FAUST software filter. The angular, mass partitioning, and QP shape observables previously described in Section 5 and Section 6 were used in this analysis. Among the observables selected were the mass and charge of the PLF and IMF, the mass, quadrupole, and octupole moments of the reconstructed QP, as well as the angular alignment of the PLF via Ψ_{out}, Φ_{in}, and $cos(\theta)$. The observables were chosen as they represent the observables that have been predicted by a range of theories to be most sensitive to the symmetry energy in this energy range ($10-15$ MeV/nucleon). The observables for each of the three systems and each of the

three parameterizations of the symmetry energy were examined system-by-system. Each system was examined individually with respect to the symmetry energy and not as an aggregate.

The reaction observables were analyzed via Sliced Inverse Regression[141, 142] directly from within the "R" statistical environment[143]. The initial analysis presented in this chapter consists of the examination of the "hot" results of CoMD filtered through the FAUST software filter. In this way, we can examine what the expected influence of the symmetry energy would be with the current detector constraints. This in effect extends the analysis in Section 7 from a binary breaking of the reaction system at short time intervals ($t \sim 400$ fm/c) to events that have already broken into three heavy reaction partners (ternary breaking of the reaction system) at $t = 3000$ fm/c. In addition, analyzing the CoMD after filtering with the FAUST software filter takes the analysis an additional step forward by filtering the data by what we expect to be reasonably detectable particles.

The current analysis takes into consideration several observables discussed in preceding chapters, namely the mass and charge of the PLF, IMF, and QP, θ_{prox}, Φ_{in}, Ψ_{out}, and the velocity quadrupole (V_{quad}). Additionally we have considered the relative difference in velocity between the magnitudes of the two fragments (ΔV), the difference in the velocity vectors of the two fragments (V_{rel}[67]), the perpendicular velocity of the QP in the center of mass frame of the system, and the mass difference between the IMF and PLF (ΔA_{frag}). The results from the analysis, shown in Figure 8.1, show a very modest ability of SIR to distinguish between the three parameterizations of the symmetry energy. In each case, there is a small but statistically significant difference between each symmetry energy. In all three cases, SIR selected the principal components with the most significant impact, as shown in Table 8.1, by assigning the highest absolute weight. In this way, the mass of the

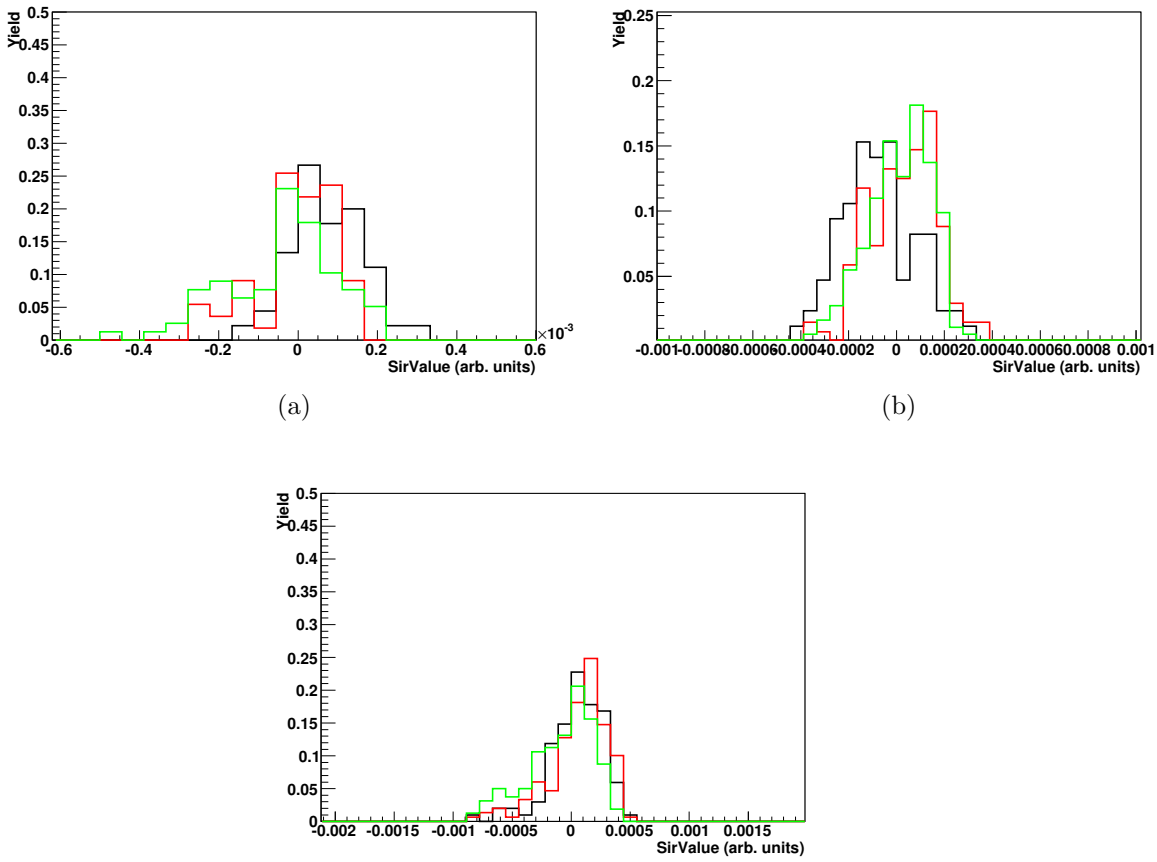

Figure 8.1: Comparison of the output from SIR when attempting to discriminate between symmetry energy parameterizations via CoMD. The results are shown system-by-system for ^{136}Xe+^{64}Ni (a), ^{124}Xe+^{58}Ni (b), ^{124}Sn+^{64}Ni (c). CoMD results for the soft, stiff, and super-stiff case shown in black, red and green respectively.

PLF, IMF and QP along with the quadrupole velocity of the reconstructed QP and the mass difference between the IMF and PLF (ΔA_{frag}) were selected as the most significant or principal components in the analysis. The observables multiplied by their determined weighting coefficients can then be summed together resulting in the value shown in abscissa of Figure 8.1, the $\mathrm{SIR}_{\mathrm{value}}$. The statistical separation confidence interval is detailed in Table 8.2

Table 8.1: SIR weighting coefficients for each observable, system-by-system, for CoMD

Reaction	^{124}Sn+^{64}Ni	^{124}Xe+^{58}Ni	^{136}Xe+^{64}Ni
A_{PLF}	-2.884×10^{-1}	7.378×10^{-1}	6.364×10^{-1}
Z_{PLF}	4.892×10^{-5}	-1.597×10^{-5}	-2.264×10^{-5}
A_{IMF}	7.557×10^{-1}	-3.403×10^{-1}	-5.002×10^{-1}
Z_{IMF}	-7.924×10^{-5}	1.895×10^{-4}	-9.256×10^{-5}
θ_{prox}	-5.778×10^{-6}	-8.843×10^{-7}	1.445×10^{-6}
Φ_{in}	5.731×10^{-7}	-1.662×10^{-7}	2.946×10^{-8}
Ψ_{out}	3.075×10^{-7}	-2.715×10^{-7}	9.902×10^{-7}
A_{QP}	-2.336×10^{-1}	-1.988×10^{-1}	-6.706×10^{-2}
ΔV_{frag}	9.415×10^{-4}	1.889×10^{-3}	5.750×10^{-3}
V_{quad}	-1.853×10^{-2}	-1.058×10^{-2}	-3.089×10^{-4}
V_{rel}	1.496×10^{-3}	-1.070×10^{-4}	-3.750×10^{-3}
V_{perp}^{QP}	-2.207×10^{-3}	-3.757×10^{-3}	-1.505×10^{-3}
ΔA_{frag}	5.220×10^{-1}	-5.390×10^{-1}	-5.693×10^{-1}

Table 8.2: Sliced Inverse Regression (SIR) separation confidence interval, system-by-system, for CoMD

E_{sym}	^{124}Sn+^{64}Ni	^{124}Xe+^{58}Ni	^{136}Xe+^{64}Ni
Soft vs. Stiff	$\geq 90\%$	$\geq 99.9\%$	$\geq 85\%$
Soft vs. Super-Stiff	$\geq 99.9\%$	$\geq 99.9\%$	$\geq 99.9\%$
Stiff vs. Super-Stiff	$\geq 99.9\%$	$\geq 80\%$	$\geq 90\%$

Nonetheless, the hot CoMD, even experimentally filtered, is still sensitive to the E_{sym}. When examining the ability of SIR to distinguish between CoMD+GEMINI (statistically decayed hot CoMD), SIR was unable to obtain a statistically significant separation. This is not a surprise as we have statistically cooled the dynamical simulations. The previously retained dynamical information about the influence of the symmetry energy on the breakup was lost when the dynamical events were decayed using a statistical decay model. The separation using SIR on the CoMD+GEMINI

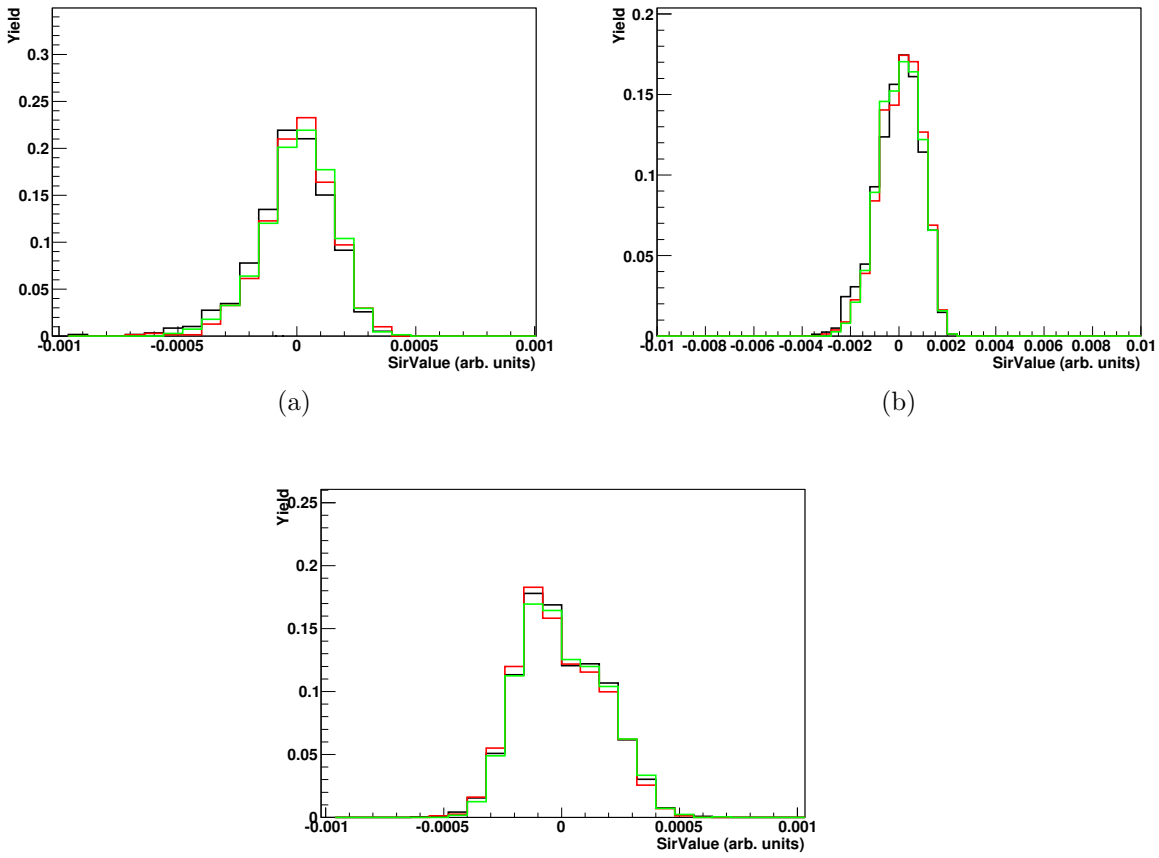

Figure 8.2: Comparison of the output from SIR when attempting to discriminate between symmetry energy parameterizations via cooled CoMD+Gemini. The results are shown system-by-system for ^{136}Xe+^{64}Ni (a), ^{124}Xe+^{58}Ni (b), ^{124}Sn+^{64}Ni (c). Cooled CoMD+Gemini results for the soft, stiff, and super-stiff case shown in black, red and green respectively.

simulations are shown in Figure 8.2. The separation confidence intervals are shown in Table 8.3. It is clear from the histograms, that the differences between the symmetry energies is much smaller after cooling with GEMINI as the distributions from the three parameterizations of the symmetry energy are now laid one on top of each other without a statistically significant separation between them. This in effect says that it is important to let the CoMD (dynamical simulations) cool dynamically in

order to help preserve the signatures that are more sensitive to the symmetry energy.

Table 8.3: Sliced Inverse Regression (SIR) separation confidence interval, system-by-system, for cooled CoMD+Gemini

E_{sym}	^{124}Sn+^{64}Ni	^{124}Xe+^{58}Ni	^{136}Xe+^{64}Ni
Soft vs. Stiff	$\leq 50\%$	$\leq 85\%$	$\leq 50\%$
Soft vs. Super-Stiff	$\leq 60\%$	$\leq 50\%$	$\leq 60\%$
Stiff vs. Super-Stiff	$\leq 70\%$	$\leq 60\%$	$\leq 50\%$

The results of the hot CoMD were then compared to those of the experimental data. However, the SIR technique did not provide a good match between the $\text{SIR}_{\text{value}}$ distributions of experimental data and the CoMD simulations. This is not unexpected as many of the probed CoMD observables were not a close fit to the experimental data. This is partially due to subtle secondary decay effects that we have shown to be evident in the experimental data. This further contributes to the inability of the SIR to fit the experimental data to the CoMD. There is still much work to be done in order to understand how we can apply multidimensional analysis to of theoretical data and extract meaningful results with experimental data. This is currently a hot topic in the machine learning and multi-dimensional statistical analysis communities.

9. CONCLUSIONS

A new beam line was simulated, designed, and constructed at the Texas A&M University Cyclotron Institute based on ∼10 million hours of theoretical simulations. This beam line was specifically aimed at executing a systematic analysis of reaction dynamics in reaction systems with $A \sim 200$ in the energy region of $10 - 15$ MeV/nucleon. Observables from the dynamic, ternary break-up of heavy, asymmetry systems have been teased out from a large background of other mechanisms utilizing the newly constructed beam line. This beam line also enables a suite of experiments where collection of residues near the beam axis is important for probing the underlying physics.

The dynamic processes associated with the ternary breaking of the reaction system have been shown to be dependent on the mass and energy of the emitting QP. The QP has been shown to preferentially emit the IMF forward of the PLF indicating a longer, sequential breakup. Secondary decay effects have been separated out from dynamical events via PLF velocity cuts. This is in agreement with simulated reactions via CoMD+GEMINI. This statistical vs. dynamical separation allowed for the analysis of the dynamical contribution to these ternary breakups. It has also been shown that in agreement with previous works, IMFs emitted toward the neck, on short time scales, are more neutron rich than those emitted forward of the PLF on longer time scales. This is also indicative of the IMFs emitted toward the neck being a fast emission, whereas the IMFs emitted forward of the PLF are due to a QP that has rotated significantly and decayed sequentially later in time.

Quadrupole and octupole moments of the hot QP have been predicted to be sensitive to the symmetry energy over long time scales ($t \leq 3000$ fm/c)[11, 44, 41,

47, 48, 49] with little experimental validation. This thesis has made a first step in measuring the deformation of the QP in velocity space and directly comparing the experimental values to those simulated via CoMD. This velocity space deformation was then correlated directly to the dynamical experimental events. This has shown that, on average, the dynamical events detected had low deformation in the velocity space.

Finally, recent work has taken a first step in examining multiple observables sensitive to the symmetry energy simultaneously. The initial work[81] provided the first step in examining theoretical models using multi-dimensional analysis. This thesis has extended this analysis technique to experimentally filtered simulated data and to simulations accounting for secondary decay effects. An important step was taken in the multi-dimensional analysis of simulated data within the constraints of the detector. This has shown that with better simulation statistics and further development of the method, better agreement between simulated and experimental data should be possible in the future. Thus it may be possible to make a determination as to the influence of the symmetry energy on experimental data using this technique.

This thesis has carefully examined and analyzed the reaction dynamics in the $E = 10 - 15$ MeV/nucleon regime. With continued development of experimental equipment, reexamination of experimental data, and creative/critical consideration of a number of experimental parameters, it should be possible to extend this work and the work of others in the field. This will aid further progress toward the end goal of understanding the reaction dynamics at lower intermediate energies. With improved detection of a wider range of events and upgrades to the detection system, characterization of the reaction dynamics in this energy regime and this experimental data set could be realistically built upon. For instance, it may be possible to design an experiment with greater sensitivity to PLFs detected off beam axis ($\theta > 2.3^{\circ}$)

while maintaining the sensitivity near the beam axis ($\theta < 2.3^{\circ}$) as presented herein.

REFERENCES

[1] Friedman, W., Phys. Rev. Lett. 60 (1988) 2125.

[2] Ono, A. and Horiuchi, H., Prog. Part. Nucl. Phys. 53 (2004) 501.

[3] Papa, M., Giuliani, G. and Bonasera, A., J. Comput. Phys. 208 (2005) 403.

[4] Fuchs, C. and Wolter, H.H., Eur. Phys. J. A 30 (2006) 5.

[5] Choppin, G.R., Liljenzin, J.O. and Rydberg, J., Radiochemistry and Nuclear Chemistry (Butterworth-Heinemann, 2002).

[6] Loveland, W.D., Morrissey, D.J. and Seaborg, G.T., Modern Nuclear Chemistry (John Wiley & Sons, 2005).

[7] Satchler, G., Phys. Rev. 109 (1958) 429.

[8] Chen, L.W., Ko, C.M. and Li, B.A., Phys. Rev. Lett. 94 (2005) 032701.

[9] Chen, L.W., Ko, C.M. and Li, B.A., Phys. Rev. C 76 (2007) 054316.

[10] Shetty, D., Yennello, S. and Souliotis, G.A., Phys. Rev. C 75 (2007) 034602.

[11] Colonna, M., J. Phys. Conf. Ser. 168 (2009) 012006.

[12] Lattimer, J.M. and Prakash, M., Science 304 (2004) 536.

[13] Baran, V., Colonna, M., Greco, V. and Ditoro, M., Phys. Rep. 410 (2005) 335.

[14] Li, B., Chen, L. and Ko, C., Phys. Rep. 464 (2008) 113.

[15] Steiner, A.W., Lattimer, J.M. and Brown, E.F., Astrophys. J. 722 (2010) 33.

[16] Klähn, T., Blaschke, D., Typel, S., van Dalen, E.N., Faessler, A. et al, Phys. Rev. C 74 (2006) 035802.

[17] Stone, J.R., Miller, J., Koncewicz, R., Stevenson, P. and Strayer, M., Phys. Rev. C 68 (2003) 034324.

[18] Danielewicz, P., Lacey, R. and Lynch, W.G., Science 298 (2002) 1592.

[19] Steiner, A., Prakash, M., Lattimer, J. and Ellis, P., Phys. Rep. 411 (2005) 325.

[20] Demorest, P.B., Pennucci, T., Ransom, S.M., Roberts, M.S.E. and Hessels, J.W.T., Nature 467 (2010) 1081.

[21] Tsang, M.B., Liu, T.X., Shi, L., Danielewicz, P., Gelbke, C.K. et al, Phys. Rev. Lett. 92 (2004) 062701.

[22] Tsang, M.B., Zhang, Y., Danielewicz, P., Famiano, M., Li, Z. et al, Phys. Rev. Lett. 102 (2009) 122701.

[23] Tsang, M.B., Stone, J.R., Camera, F., Danielewicz, P., Gandolfi, S. et al, Phys. Rev. C 86 (2012) 015803.

[24] Kohley, Z., Colonna, M., Bonasera, A., May, L.W., Wuenschel, S. et al, Phys. Rev. C 85 (2012) 064605.

[25] Baran, V., Colonna, M., Di Toro, M., Greco, V., Zielinska-Pfabe, M. et al, Nucl. Phys. A 703 (2002) 603.

[26] Geraci, E., Bruno, M., D'Agostino, M., De Filippo, E., Pagano, A. et al, Nucl. Phys. A 732 (2004) 173.

[27] Famiano, M.A., Liu, T., Lynch, W.G., Mocko, M., Rogers, A.M. et al, Phys. Rev. Lett. 97 (2006) 052701.

[28] Shetty, D., Yennello, S., Botvina, A., Souliotis, G.A., Jandel, M. et al, Phys. Rev. C 70 (2004) 011601.

[29] Yong, G.C., Li, B.A., Chen, L.W. and Zuo, W., Phys. Rev. C 73 (2006) 034603.

[30] Souder, P.A., Holmes, R., Jen, C.M., Zana, L., Ahmed, Z. et al, PAC38 (2010).

[31] Roca-Maza, X., Centelles, M., Viñas, X. and Warda, M., Phys. Rev. Lett. 106 (2011) 252501.

[32] Ban, S., Horowitz, C.J. and Michaels, R., J. Phys. G Nucl. Part. Phys. 39 (2012) 015104.

[33] Brown, B.A., Phys. Rev. Lett. 85 (2000) 5296.

[34] Möller, P., Myers, W.D., Sagawa, H. and Yoshida, S., Phys. Rev. Lett. 108 (2012) 052501.

[35] Tews, I., Krüger, T., Hebeler, K. and Schwenk, A., Phys. Rev. Lett. 110 (2013) 032504.

[36] Steiner, A.W., Lattimer, J.M. and Brown, E.F., Astrophys. J. Lett. 765 (2013) L5.

[37] 3rd International Symposium on Nuclear Symmetry Energy, NuSym2013 (http://www.nucl.phys.tohoku.ac.jp/nusym13/). Last Accessed: 12-3-2014.

[38] Int. Workshop on the Multi-facets of the Equation of State and Clustering 2014, IWM - EC 2014 (https://agenda.infn.it/conferenceDisplay.py?confId=6673). Last Accessed: 12-3-2014.

[39] Di Toro, M., Baran, V., Colonna, M., Gaitanos, T., Rizzo, J. et al, Prog. Part. Nucl. Phys. 53 (2004) 81.

[40] Di Toro, M., Olmi, A. and Roy, R., Eur. Phys. J. A 30 (2006) 65.

[41] Di Toro, M., Baran, V., Colonna, M., Ferini, G., Gaitanos, T. et al, Nucl. Phys. A 787 (2007) 585.

[42] Di Toro, M., Colonna, M., Rizzo, C. and Baran, V., Int. J. Mod. Phys. E 17 (2008) 110.

[43] Di Toro, M., Baran, V., Colonna, M. and Greco, V., J. Phys. G Nucl. Part. Phys. 37 (2010) 083101.

[44] Baran, V., Colonna, M. and Di Toro, M., Nucl. Phys. A 730 (2004) 329.

[45] Lionti, R., Baran, V., Colonna, M. and Di Toro, M., Phys. Lett. B 625 (2005) 33.

[46] Colonna, M., Ono, A. and Rizzo, J., Phys. Rev. C 82 (2010) 054613.

[47] Shvedov, L., Colonna, M. and Di Toro, M., Phys. Rev. C 81 (2010) 054605.

[48] Rizzo, C., Baran, V., Colonna, M., Corsi, A., Di Toro, M. et al, Phys. Rev. C 83 (2011) 014604.

[49] Rizzo, C., Colonna, M., Baran, V. and Di Toro, M., arXiv (2014), 1407.0831.

[50] De Filippo, E., Pagano, A., Wilczyński, J., Amorini, F., Anzalone, A. et al, Phys. Rev. C 71 (2005) 044602.

[51] Fleischer, R., Price, P., Walker, R. and Hubbard, E., Phys. Rev. 143 (1966) 943.

[52] Becker, H., Vater, P., Brandt, R., Boos, A. and Diehl, H., Phys. Lett. B 50 (1974) 445.

[53] Glässel, P., Harrach, D., Specht, H.J. and Grodzins, L., Zeitschrift für Phys. A Hadron. Nucl. 310 (1983) 189.

[54] Casini, G., Phys. Rev. Lett. 71 (1993) 2567.

[55] Stefanini, A.A., Casini, G., Maurenzig, P., Olmi, A., Charity, R.J. et al, Zeitschrift für Phys. A Hadron. Nucl. 351 (1995) 167.

[56] Charity, R.J., Freifelder, R., Gobbi, A., Herrmann, N., Hildenbrand, K.D. et al, Hadron. Nucl. 341 (1991) 53.

[57] Piantelli, S., Bidini, L., Poggi, G., Bini, M., Casini, G. et al, Phys. Rev. Lett. 88 (2002) 052701.

[58] Skwira-Chalot, I., Siwek-Wilczyńska, K., Wilczyński, J., Amorini, F., Anzalone, A. et al, Phys. Rev. Lett. 101 (2008) 262701.

[59] Wilczyński, J., Skwira-Chalot, I., Siwek-Wilczyńska, K., Pagano, A., Amorini, F. et al, Phys. Rev. C 81 (2010) 067604.

[60] Wilczyński, J., Skwira-Chalot, I., Siwek-Wilczyńska, K., Pagano, A., Amorini, F. et al, Phys. Rev. C 81 (2010) 024605.

[61] Cap, T., Siwek-Wilczyńska, K., Skwira-Chalot, I. and Wilczyński, J., Phys. Scr. T154 (2013) 014007.

[62] De Filippo, E., Amorini, F., Anzalone, A., Auditore, L., Baran, V. et al, Acta Phys. Pol. B 40 (2009) 1199.

[63] Russotto, P., De Filippo, E., Pagano, A., Piasecki, E., Amorini, F. et al, Phys. Rev. C 81 (2010) 064605.

[64] Piantelli, S., Casini, G., Maurenzig, P., Olmi, A., Barlini, S. et al, Phys. Rev. C 88 (2013) 064607.

[65] Hudan, S., Alfaro, R., Beaulieu, L., Davin, B., Larochelle, Y. et al, Phys. Rev. C 70 (2004) 031601.

[66] McIntosh, A.B., Hudan, S., Black, J., Mercier, D., Metelko, C.J. et al, Phys. Rev. C 81 (2010) 034603.

[67] Davin, B., Alfaro, R., Xu, H., Beaulieu, L., Larochelle, Y. et al, Phys. Rev. C 65 (2002) 064614.

[68] Hudan, S., Souza, R. and Ono, A., Phys. Rev. C 73 (2006) 054602.

[69] Hudan, S., McIntosh, A.B., Black, J., Mercier, D., Metelko, C.J. et al, Phys. Rev. C 80 (2009) 064611.

[70] Brown, K., Hudan, S., DeSouza, R.T., Gauthier, J., Roy, R. et al, Phys. Rev. C 87 (2013) 061601.

[71] Aiello, S., Anzalone, A., Baldo, M., Cardella, G., Cavallaro, S. et al, Nucl. Phys. A 583 (1995) 461.

[72] Lukasik, J. and Majka, Z., Acta Phys. Pol. B 24 (1993) 22.

[73] Plagnol, E., Łukasik, J., Auger, G., Bacri, C.O., Bellaize, N. et al, Phys. Rev. C 61 (1999) 014604.

[74] Papa, M., Amorini, F., Anzalone, A., Auditore, L., Baran, V. et al, Phys. Rev. C 75 (2007) 054616.

[75] Colonna, M., Fabbri, G., Di Toro, M., Matera, F. and Wolter, H., Nucl. Phys. A 742 (2004) 337.

[76] Chbihi, A., Manduci, L. and Moisan, J., J. Phys. Conf. Ser. 420 (2013) 012099.

[77] Henry, E., Toke, J., Nyibule, S., Quinlan, M., Schöder, W.U. et al, arXiv (2014), 1404.3758v1.

[78] Colonna, M., Di Toro, M., Guarnera, A., Maccarone, S., Zielinska-Pfabé, M. et al, Nucl. Phys. A 642 (1998) 449.

[79] Colonna, M., Burgio, G., Chomaz, P., Di Toro, M. and Randrup, J.r., Phys. Rev. C 47 (1993) 1395.

[80] Colonna, M., Di Toro, M. and Guarnera, A., Nucl. Phys. A 580 (1994) 313.

[81] Cammarata, P., Colonna, M., Bonasera, A., McIntosh, A.B., Kohley, Z. et al, Nucl. Instruments Methods Phys. A 761 (2014) 1.

[82] Greco, V., Guarnera, A., Colonna, M. and Toro, M.D., Phys. Rev. C 59 (1999) 810.

[83] Charity, R.J., ICTP-IAEA Adv. Work. Model Codes (2008).

[84] Charity, R.J., Phys. Rev. C 82 (2010) 014610.

[85] Mancusi, D., Charity, R.J. and Cugnon, J., Phys. Rev. C 82 (2010) 044610.

[86] Aichelin, J., Phys. Rep. 2002 (1991) 233.

[87] Kohley, Z.W., Mid-rapidity Fragmetns in Fermi Energy Heavy Ion Collisions, PhD thesis, Texas A&M University, 2010.

[88] Guarnera, A., Colonna, M. and Chomaz, P., Phys. Lett. B 373 (1996) 267.

[89] Rizzo, J., Chomaz, P. and Colonna, M., Nucl. Phys. A 806 (2008) 40.

[90] Ayik, S. and Gregoire, C., Phys. Lett. B 212 (1988) 269.

[91] Chomaz, P., Colonna, M. and Randrup, J., Phys. Rep. 389 (2004) 263.

[92] Bonasera, A., Gulminelli, F. and Molitoris, J., Phys. Rep. 243 (1994) 1.

[93] Hauser, W. and Feshbach, H., Phys. Rev. 87 (1952) 366.

[94] Bohr, N. and Wheeler, J., Phys. Rev. 56 (1939) 284.

[95] Gimeno-Nogues, F., Rowland, D., Ramakrishnan, E., Ferro, S., Vasal, S. et al, Nucl. Instruments Methods Phys. A 399 (1997) 94.

[96] Souliotis, G.A., Shetty, D., Keksis, A., Bell, E., Jandel, M. et al, Phys. Rev. C 73 (2006) 024606.

[97] Souliotis, G.A., Botvina, A.S., Shetty, D.V., Keksis, A.L., Jandel, M. et al, Phys. Rev. C 75 (2007) 011601.

[98] Souliotis, G.A., Keksis, A., Stein, B., Veselsky, M., Jandel, M. et al, Nucl. Instruments Methods Phys. B 261 (2007) 1094.

[99] Barbui, M., Pesente, S., Nebbia, G., Fabris, D., Lunardon, M. et al, Nucl. Instruments Methods Phys. B 265 (2007) 605.

[100] Souliotis, G.A., Stein, B., Veselsky, M., Galanopoulos, S., Keksis, A. et al, Nucl. Instruments Methods Phys. B 266 (2008) 4692.

[101] Kheswa, N., iThemba Labs (http://www.tlabs.ac.za). Last Acessed: 12-3-2014.

[102] Trace Sciences International, Trace Sciences (http://www.tracesciences.com). Last Acessed: 12-3-2014.

[103] Davin, B., de Souza, R.T., Yanez, R., Larochelle, Y., Alfaro, R. et al, Nucl. Instruments Methods Phys. A 473 (2001) 302.

[104] Todd, R., RIS-Corp, 5905 Weisbrook Lane, Suite 102 Knoxville, TN 37909, 2013.

[105] Brown, K. and Carey, D., SLAC-91, Rev. 3 (1983).

[106] Kowalski, S. and Enge, H., Nucl. Instruments Methods Phys. A 258 (1987) 407.

[107] Makino, K. and Berz, M., Nucl. Instruments Methods Phys. A 558 (2006) 346.

[108] Tassan-Got, L. and Stephan, C., Nucl. Phys. A 524 (1991) 121.

[109] Knoll, G.F., Radiation Detection and Measurement (John Wiley & Sons, Ann Arbor, 2002).

[110] Leo, W.R., Techniques for Nuclear and Particle Physics Experiments (Springer, New York, 1994).

[111] Elson, J., PicoSystems (www.pico-systems.com). Last Accessed: 12-3-2014.

[112] May, L.W., Kohley, Z., Wuenschel, S., McIntosh, A.B., Souliotis, G.A. et al, AIP Conf. Proc. 616 (2013) 616.

[113] Wuenschel, S.K., Temperature and Scaling Studies from Projectile Fragmentation of 86,78Kr+ 64,58Ni at 35 MeV/A, PhD thesis, Texas A&M University, 2009.

[114] Souliotis, G.A., Veselsky, M., Shetty, D., Trache, L. and Yennello, S., Nucl. Phys. A 746 (2004) 526.

[115] Tarasov, O. and Bazin, D., Nucl. Phys. A 746 (2004) 411.

[116] Tarasov, O. and Bazin, D., LISE++ (http://lise.nscl.msu.edu/lise.html). Last Accessed: 12-3-2014.

[117] Ziegler, J.F., SRIM (http://www.srim.org/). Last Accessed: 12-3-2014.

[118] Ziegler, J.F., Ziegler, M. and Biersack, J., Nucl. Instruments Methods Phys. B 268 (2010) 1818.

[119] Tassan-Got, L., Nucl. Instruments Methods Phys. B 194 (2002) 503.

[120] Tabacaru, G., Borderie, B. and Ouatizerga, A., Nucl. Instruments Methods Phys. A 428 (1999) 379.

[121] Effron, B., Ann. of Stat. 7 (1979) 1.

[122] Tribble, R., Burch, R. and Gagliardi, C., Nucl. Instruments Methods Phys. A 285 (1989) 441.

[123] Keksis, A.L., May, L.W., Souliotis, G.A., Veselsky, M., Galanopoulos, S. et al, Phys. Rev. C 81 (2010) 054602.

[124] Soisson, S.N., Isospin Dependence of Fragmentation, PhD thesis, Texas A&M University, 2010.

[125] Soisson, S.N., Botvina, A., Souliotis, G.A., Stein, B.C., Heilborn, L. et al, J. Phys. G Nucl. Part. Phys. 39 (2012) 115104.

[126] Agostinelli, S., Allison, J., Amako, K., Apostolakis, J., Araujo, H. et al, Nucl. Instruments Methods Phys. A 506 (2003) 250.

[127] Courant, E.D., Rev. Sci. Instrum. 22 (1951) 1003.

[128] Burge, E.J. and Smith, D.A., Rev. Sci. Instrum. 33 (1962) 1371.

[129] Gruyer, D., Frankland, J.D., Bonnet, E., Boisjoli, M., Chbihi, A. et al, EPJ Web Conf. 62 (2013) 07006, 1308.5302.

[130] Hudan, S. and DeSouza, R.T., Eur. Phys. J. A 50 (2014) 36.

[131] Stiefel, K., Kohley, Z., de Souza, R.T., Hudan, S. and Hammerton, K., Phys. Rev. Lett. (submitted) 1.

[132] Montoya, C., Lynch, W. and Bowman, D., Phys. Rev. Lett. 73 (1994) 3070.

[133] Toke, J., Lott, B. and Baldwin, S., Phys. Rev. Lett. 7 (1995) 2920.

[134] Russotto, P., Dynamical Emission of Heavy Fragments in the 112,124 Sn+ 58, 64Ni Reactions at 35 AMeV as Seen with CHIMERA, PhD thesis, Università degli Studi di Catania, 2006.

[135] Vandenbosch, R. and Huizenga, J., Nuclear Fission (Academic, 1973).

[136] Vertés, A., Nagy, S., Klencsár, Z., Lovas, R. and Rösch, editors, Handbook of Nuclear Chemistry, 2nd ed. (Springer, 2011).

[137] Pearson, K., London, Edinburgh, Dublin Philos. Mag. J. Sci. 6 (1901) 559.

[138] Gosset, W.S., Biometrika 6 (1908) 1.

[139] Fisher, R.A. and Mackenzie, W.A., Stud. Crop Var. II Manor. response Differ. potato Var. J. Agric. Sci. Cambridge 13 (1923) 311.

[140] Fisher, R., Ann. Eugen. 7 (1936) 179.

[141] Li, K., J. Am. Stat. Assoc. 86 (1991) 316.

[142] Weisberg, S., J. Stat. Softw. 7 (2002) 1.

[143] R: A Language and Environment for Statistical Computing (R Foundation for Statistical Computing, Vienna, Austria, 2013).